THE UNIVERSITY *of* EDINBURGH

Lattice Models of Pattern Formation in Bacterial Dynamics

Alasdair Thompson

A thesis submitted in fulfilment of the requirements
for the degree of Doctor of Philosophy
to the
University of Edinburgh
October 2011

Abstract

In this thesis I study a model of self propelled particles exhibiting run-and-tumble dynamics on lattice. This non-Brownian diffusion is characterised by a random walk with a finite persistence length between changes of direction, and is inspired by the motion of bacteria such as *Escherichia coli*. By defining a class of models with multiple species of particle and transmutation between species we can recreate such dynamics. These models admit exact analytical results whilst also forming a counterpart to previous continuum models of run-and-tumble dynamics. I solve the externally driven non-interacting and zero-range versions of the model exactly and utilise a field theoretic approach to derive the continuum fluctuating hydrodynamics for more general interactions. I make contact with prior approaches to run-and-tumble dynamics off lattice and determine the steady state and linear stability for a class of crowding interactions, where the jump rate decreases as density increases.

In addition to its interest from the perspective of nonequilibrium statistical mechanics, this lattice model constitutes an efficient tool to simulate a class of interacting run-and-tumble models relevant to bacterial motion. Pattern formation in bacterial colonies is confirmed to be able to stem solely from the interplay between a diffusivity that depends on the local bacterial density and regulated division of the cells, in particular without the need for any explicit chemotaxis. This simple and generic mechanism thus provides a null hypothesis for pattern formation in bacterial colonies which has to be falsified before appealing to more elaborate alternatives. Most of the literature on bacterial motility relies on models with instantaneous tumbles. As I show, however, the finite tumble duration can play a major role in the patterning process. Finally a connection is made to some real experimental results and the population ecology of multiple species of bacteria competing for the same resources is considered.

Declaration

Except where otherwise stated, the research undertaken in this thesis was the unaided work of the author. Where the work was done in collaboration with others, a significant contribution was made by the author.

A. Thompson
June 2011

Acknowledgements

I would like to record my thanks to all those who have helped me in the course of this work. In particular, the following:

Mike Cates, Richard Blythe and Julien Tailleur for all their support in supervising me over the last three years. I couldn't possibly have managed to complete this project in the time I have without their help, guidance and collaboration. Julien, in particular, I would like to thank for constantly pushing me not to simply drift along following the instructions they gave me, but to consider my own ideas and to think about where I wanted to go.

Martin Evans and Wilson Poon for their feedback in interviewing me after my first and second years and reviewing my reports. Their advice helped me to realise where I had to be clearer in my exposition and to focus on what I wanted to achieve from my PhD.

Davide Marenduzzo for numerous useful discussions and collaboration on the work on pattern formation in growing bacterial colonies.

Jane Patterson for helping me out with all the admin that goes with working or studying in a university and which I could never work out by myself.

All the people I've shared an office with and who have been able to offer advice when my code wouldn't compile or I was struggling to analyse or visualise my data.

Finally all my friends and family for their support in keeping me sane and solvent until now.

Contents

List of Figures

Chapter 1

Introduction

In recent years the study of biological, and in particular bacterial, systems has become of interest in mathematics and physics. Biological systems provide real world examples of non-equilibrium dynamics—where there is never a static equilibrium but even at steady-state currents and flows exist—but remain simple enough and easy enough to manipulate that progress can be made both analytically and experimentally. Their study provides us with the possibility to experimentally test the predictions of some more abstract mathematical models and offers us inspiration to develop new ones.

In this thesis I construct a number of lattice models of the movement and reproduction of bacteria. The non-interacting continuum limit of these recovers the off lattice equations previously derived for non-interacting particles obeying dynamics characteristic of bacteria such as *Escherichia coli* [2,3]. (These equations are discussed in chapter 2.) I will also address interactions in the form of density dependent motility parameters, and thereby connect also with the off lattice approach of Cates and Tailleur [4]. Finally I will couple my models to logistic population dynamics, which will allow me to investigate the population ecology of multiple competing species.

Although real bacterial systems do not exist fixed to a discrete lattice, there are a number of advantages to treating them as such for the purpose of analytic or computational study. Both the microscopic run-and-tumble equations, and the diffusive continuum equations found by coarse graining these, are difficult to simulate efficiently off-lattice, particularly once interactions are included. On-lattice the local density of particles is easy to determine and so density-dependent

interactions are easy to include at relatively low cost computationally. Lattice simulations are also easier to extend to higher dimensions as we will consider towards the end of this thesis. For all these reasons, creation of a robust and accurate lattice representation of bacterial motility is a worthwhile goal, even from a purely phenomenological standpoint, whereby the purpose of a model is to provide a fairly direct explanation for results seen in experiment.

A second motivation is more fundamental. Models of non-equilibrium statistical mechanics can be broadly split into two categories: one phenomenological as just described, the other comprising simple models which allow the study of basic concepts and facilitate a more detailed understanding of the nature of non-equilibrium physics. In the latter category we can think of lattice transport models such as the exclusion [5] or zero-range [6] processes, for which some exact analytical results can be found, as well as methods to characterise fluctuations and large deviations in non-equilibrium states [7]. My models fall squarely into this category of simple theoretical models, and indeed extend some of these examples; I investigate both a zero-range process and a partially excluding system. For these microscopic lattice models we can, under certain conditions, calculate exact steady states and understand precisely how changes in the underlying dynamics affect the probability distributions. More generally we can always write an exact master equation for the probability of a configuration and utilise a variety of field theoretic representations to derive the large scale fluctuating hydrodynamics, to attempt to map the system to a free energy and to determine the steady state behaviour and dynamic stability.

Though many of the results and techniques utilised in this thesis will apply more broadly, and will be approached from the standpoint of theoretical physics, my motivation throughout shall be the spatial and population dynamics of bacteria. Before attempting to describe the models I have investigated I will, in chapter 2, therefore briefly review the relevant features of bacterial motility and reproduction. I describe several previous attempts at modelling these behaviours and recount a few key concepts in non-equilibrium statistical physics.

Having thus established the background to this work, in chapter 3 I present the basic mathematical frameworks required to build and analyse my models. I describe the use of lattice models in statistical physics, discuss how to move from the master equation for the evolution of the probability density for interacting

particles on a lattice to the continuum Langevin equation for the density and the fluctuating hydrodynamics for interacting particles. I will detail the field theoretic techniques used to systemically derive the continuum behaviour of my lattice models, the correct procedure to perform the diffusive rescaling and the connection to large deviation functions. Finally I explain the various algorithms used in my simulations and compare their efficiency.

Eventually we want to be able to describe systems in which bacteria interact with each other through some density dependence in their motility. Before considering that more complex case, however, in chapter 4 I look at what understood be done about non-interacting bacteria undergoing the characteristic run-and-tumble dynamics seen, for example, in *Escherichia coli*. In one dimension, with both closed and periodic boundary conditions, we can in fact calculate the full steady state probability distribution even for completely inhomogeneous and anisotropic dynamics. I present that analytic solution and several examples in chapter 4.

In chapter 5 I investigate the first interacting model of this thesis, a zero-range process (where particles hop on a lattice with rates that depend on the density at the departure site only) which can under certain conditions, which I detail, be solved analytically. The model I use shows separation into high density single site clusters against a low density background. I derive conditions for these clusters to be finitely sized—in comparison to the more standard condensation seen in zero-range processes where the clusters scale with the system size L. I examine and characterise the dynamics of this clustering and show how the number of clusters relaxes through a series of condensation and evaporation events toward an analytically determinable steady state. As already explained, in addition to being an interesting toy model that we can use to understand driven non-equilibrium physics, our model also forms a direct lattice counterpart to some well established phenomenological continuum models of bacterial dynamics. It is unusual for a model to allow exact computations while credibly describing the real behaviour of a physical system, and this is one of the reasons why this model is of interest.

In chapter 6 I begin to develop a model which more closely resembles real physical systems. I derive the steady state of the zero-range model from chapter 5 using the field theory technique from chapter 3 then extend the model to finite-

range interactions. In so doing the isolated high density sites we saw previously are replaced with extended contiguous domains. Further extending the model to higher dimensions I measure the coarsening of these domains over time. Finally I look at how the finite-range interactions lead to an effective surface tension and derive an expression for this term from the microscopic dynamics.

In chapter 7 I introduce the final basic element of my bacterial modelling: population dynamics. I present a model of bacteria interacting via a density dependent motility which separate into high and low density domains due to a dynamic instability. As seen previously off-lattice, the birth-death dynamics then arrest this separation leading to a characteristic length scale on which a variety of patterns from droplets to stripes form. Through the mappings derived in chapter 6 I can quantitatively compare my simulation results to previous analytical work off-lattice [1]. Finally I consider the robustness of my results to a variety of implementations of the regulated cell division and find that so long as the net growth rate declines as density increases the precise details can be substantially altered without qualitatively altering the outcome.

Lastly, in chapter 8 I consider cooperation and competition between multiple types of bacteria interacting on a common substrate and competing for common resources. I examine the stability and steady state of a number of models, extending a previous model of the growth of *Proteus mirabilis* colonies to two dimensions and to include the effects of noise. I end with some preliminary results on competition between two identical species of bacteria and show how the multiple instabilities resulting from their interaction can result not only in separation of the total density into domains of high and low density, but also in the "dissociation" of the two species (whereby each domain is dominated by just one of the two species present).

Chapter 2

Background

Before we delve into the details of the models of bacterial dynamics and colony growth described herein, we should first review a little of the background literature. I begin by defining a few key concepts in the modelling of non-equilibrium processes which will be useful for both the analytical and computational treatments described in chapter 3. I then explain the importance to the study of non-equilibrium systems played by biological processes and describe the basic biological features we wish to understand. I review a number of prior approaches to modelling their dynamics and touch on how this work will go beyond those results. Finally in this chapter there is a brief discussion of patterning in bacterial colonies, a topic which will be taken up in more detail in chapter 7.

2.1 Non-Equilibrium Dynamics

The necessary background material on non-equilibrium dynamics can be found in a large number of books on statistical mechanics (for example Gardiner [8]). A brief overview of the most important concepts is included here as a reminder for the ease of the reader.

2.1.1 What is a stochastic process? and a Markov process?

A *stochastic process* is a sequence of random variables, say X_t, labelled by some parameter which we shall call t, for say time, which can be discrete or continuous. In our case the positions and internal states of the particles we model will take the role of random variables, which will change over time in some not totally deterministic manner.

Let us define then a particular configuration of the system we are interested in as $\mathcal{C}$, chosen from some state space $\mathcal{N}$ of all possible configurations, and a trajectory to be a particular realisation of a sequence of configurations, say $\mathcal{T} = \{\mathcal{C}_1, \mathcal{C}_2, \ldots, \mathcal{C}_T\}$, for a trajectory of $T-1$ discrete configuration changes.

A *Markov process* is defined as a stochastic process where the probability of a future configuration is dependent only on the current configuration, independent of any prior states; mathematically

$$P\left[\mathcal{C}_{t+1}|\mathcal{C}_t, \mathcal{C}_{t-1}, \ldots, \mathcal{C}_0\right] = P\left[\mathcal{C}_{t+1}|\mathcal{C}_t\right]. \tag{2.1}$$

For calculating results, both analytically and computationally, this property makes our work considerably simpler and we will model all the systems considered in this thesis as Markov processes.

Computationally, we need only store the current configuration, not the whole history of the system, vastly reducing the required memory, while analytically we can describe the evolution of the probability of a given configuration, $P[\mathcal{C}_t]$, in continuous time, by an ordinary differential equation, called the master equation,

$$\frac{\mathrm{d}P[\mathcal{C}_t]}{\mathrm{d}t} = \sum_{\mathcal{C}' \neq \mathcal{C}} W_t\left(\mathcal{C}' \to \mathcal{C}\right) P[\mathcal{C}'_t] - \sum_{\mathcal{C}' \neq \mathcal{C}} W_t\left(\mathcal{C} \to \mathcal{C}'\right) P[\mathcal{C}_t], \tag{2.2}$$

where $W_t\left(\mathcal{C} \to \mathcal{C}'\right)$ is the rate for a transition to occur between configuration $\mathcal{C}$ and $\mathcal{C}'$ at time t.

In general, for a non-Markovian process we would need to write the master equation as an integro-differential equation over all time from initialisation till the current state.

In some cases we will be able to calculate the various statistical properties of our system exactly, while in others we will have to make certain approximations

in order to proceed analytically. We can, however, even in these cases, determine the properties of the system computationally. By starting the system in some known configuration $\mathcal{C}_0$ and evolving it forward via some *Markov Chain Monte Carlo* (MCMC) algorithm, using the transition rates $W(\mathcal{C}' \to \mathcal{C})$, the system will, if a unique steady state distribution exists, gradually approach this distribution, $P[\mathcal{C}_\infty]$, and any particular realisation of the computer simulation can be seen as having been sampled from this distribution. Through multiple simulation runs we can, therefore, build up a picture of $P[\mathcal{C}_\infty]$, and other statistical properties, which we can compare to our approximate analytical results. The details of the algorithms used in this thesis are described in section 3.3.

2.1.2 Equilibrium and Non-Equilibrium Steady-States

For an equilibrium system in contact with a heat bath of inverse temperature β we can write the probability of a configuration $\mathcal{C}$ as

$$P[\mathcal{C}] \propto e^{-\beta E[\mathcal{C}]}, \tag{2.3}$$

where $E[\mathcal{C}]$ is the internal energy of the state. This is the Gibbs-Boltzmann distribution.

The dynamics of the system in the equilibrium state are reversible, so there are no net currents and the probability of starting in some configuration $\mathcal{C}_1$ and observing a given trajectory $\{\mathcal{C}_1, \mathcal{C}_2, \ldots, \mathcal{C}_T\}$ is equal to the probability of starting in $\mathcal{C}_T$ and observing the reverse trajectory $\{\mathcal{C}_T, \ldots, \mathcal{C}_2, \mathcal{C}_1\}$. That is

$$P(\mathcal{C}_1)W(\mathcal{C}_1 \to \mathcal{C}_2)..W(\mathcal{C}_{T-1} \to \mathcal{C}_T) = P(\mathcal{C}_T)W(\mathcal{C}_T \to \mathcal{C}_{T-1})..W(\mathcal{C}_2 \to \mathcal{C}_1). \tag{2.4}$$

The transition rates between configurations and the probabilities of observing each configuration must then obey a *detailed balance* relation

$$P[\mathcal{C}]W(\mathcal{C} \to \mathcal{C}') = P[\mathcal{C}']W(\mathcal{C}' \to \mathcal{C}), \tag{2.5}$$

for every pair of configurations $\mathcal{C}$ and $\mathcal{C}'$.

In contrast, for a non-equilibrium steady state, we require only that the right

hand side of the master equation vanishes, and hence that

$$\sum_{\mathcal{C}' \neq \mathcal{C}} P[\mathcal{C}] W\left(\mathcal{C} \to \mathcal{C}'\right) = \sum_{\mathcal{C}' \neq \mathcal{C}} P[\mathcal{C}'] W\left(\mathcal{C}' \to \mathcal{C}\right). \tag{2.6}$$

In this case there can be closed current loops even in the steady state and the probability distribution will not be given by the Gibbs-Boltzmann distribution. It is these non-equilibrium states which we shall, primarily, investigate in this thesis. It should be noted that there is no general method to calculate the steady state distribution for non-equilibrium processes and so the systems which can be solved by specific means are thus of particular interest, as they highlight the kind of steady-state for which we should look.

2.2 Biology: Bacterial Dynamics

The last decade has seen a growing number of studies of biological systems conducted by physicists. Much of this work relies on tools not traditionally found in biology. For instance, recent methods of nonlinear optics have made possible observation of biological systems on much smaller scales than was previously possible [9]. In other cases biological systems have helped shed light on questions of fundamental importance in theoretical physics. Studies of bird flocks showed that it may be possible to observe long range order in two dimensional systems with a continuous symmetry if detailed balance is broken [10] (in equilibrium this is forbidden by the Mermin-Wagner theorem [11]).

Bacteria provide one example of a biological system which is of great interest to the study of non-equilibrium physics.

Movement on bacterial length scales is very different to that at scales we are accustomed to in everyday life. Viscosity becomes far more important in determining dynamics, while inertia becomes almost completely unimportant. We can quantify the relative importance of the two through the dimensionless number $\Re$, known as the Reynolds number, equal to the ratio of the inertial to viscous forces. Mathematically $\Re$ is given by

$$\Re = \frac{a\, v\, \rho}{\eta}, \tag{2.7}$$

where a is a characteristic length - the size of the bacteria in our case - v is the velocity of the object, ρ is the density of the fluid through which it moves and η is the dynamic viscosity of said fluid. For a person swimming in water at standard temperature and pressure the Reynolds number is typically of order $\mathcal{O}(10^6)$, while for bacteria swimming in a typical medium it is of order $\mathcal{O}(10^{-5})$. At low Reynolds number the Navier-Stokes equation, governing the hydrodynamics of the system, simplifies considerably

$$-\nabla p + \eta \nabla^2 \mathbf{v} = \cancelto{0}{\rho \frac{\partial \mathbf{v}}{\partial t} + \rho (\mathbf{v} \cdot \nabla) \mathbf{v}}, \tag{2.8}$$

here p denotes the pressure in the fluid. We see that the inertial terms — and hence any time dependence — drop out of the equation and, so find that any reciprocal motion cannot lead to a net displacement over time; we always end back where we started from such an action. This observation was referred to as the *Scallop Theorem* by Purcell [12]; scallops, which have just one degree of freedom - to open or close their shell - would not be capable of self-propelled motion at low Reynolds number, and can move only by virtue of turbulent effects, i.e. because at high Reynolds the time dependent terms in the Navier-Stokes equation do not drop out and the process is not reversible. For bacteria, however, which do exist in a low Reynolds environment, this type of propulsion is not possible, and multiple degrees of freedom which allow them to perform a circuitous path in the phase space of their physical configurations are required. This is exactly what some species of bacteria, such as *Escherichia coli*, do, rotating helical flagella to propel themselves forward by means of a series of relatively straight runs interspersed with short periods of chaotic motion, known as tumbles, during which their orientation changes at random and they experience little net displacement [13]. This can be seen as a type of non-Brownian diffusion where the steady state probability distribution for particle position will not be Boltzmann.

Following experiments to determine their behaviour by Berg and others [14–20] from the 1970s onwards, much is known about the dynamics and behaviour of individual bacteria. Less, however, is known about their collective behaviour and it is here that statistical mechanics can play a useful role. We have attempted to create a microscopic model of their movement, from which information on their collective dynamics and behaviour can be determined. Before we discuss

our models of bacterial dynamics, however, it is useful to review a little of the biology of the organisms we hope to understand.

E. coli is a single celled, rod-shaped organism. It is approximately $2\mu m$ in length and $1\mu m$ in diameter and is covered in, on average, 4-6 helical flagella [21] approximately $20nm$ in diameter and several μm in length. By tethering a bacterium and adding attractant and repellent chemicals, Larsen et al. [18] was able to induce both runs and tumbles and observe that the tumbles are associated with clockwise (CW) rotation of the flagella whereas runs are associated with counter-clockwise (CCW) rotation, as observed by looking down the flagella towards the cell body. During runs the flagella form a bundle at the rear of the cell [15], forced together by geometrical and hydrodynamic constraints [19]. The polymorphic form of the flagella changes on rotating CCW, switching the chirality of the helix and forcing the bundle apart [20]. For a more complete account of the properties of bacterial flagella, their structure, assembly, genetics and operation see Berg [16].

In the absence of chemotaxis, a directed movement along a chemical gradient, the tumbles last approximately 0.1s and the runs 1s [14, 20], with an exponential distribution of durations. The runs and tumbles of different lengths occur at random and with Poissonian statistics [14], justifying our later use of constant rates for the bacteria in our model to move or change direction.

E. coli can also undergo chemotaxis, moving preferentially towards or away from certain chemicals. Berg found that on exposing a culture of bacteria to a gradient of serine, an amino acid, caused the run length to increase and the tumble rate to decrease [14]. Non-chemotactic mutants showed no response to the chemical. The change in behaviour for those bacteria which were chemotactic, however, was quite pronounced: their speed increased by around 40%, the change in direction from run to run decreased and the rate of tumbling decreased by a similar amount. The behaviour also appeared different when moving up and down the serine gradient. On swimming up the gradient the tumble rate decreased; on moving down the rate was the same as in an isotropic medium of the same local concentration [14].

In the last two decades, much of the work on bacterial motility has focused on chemotaxis [22–26]. Schnitzer et al. analysed various strategies bacteria may employ, e.g. changing their speed or tumble rate, and studied the differences

these techniques make to the steady state distribution. They found the density of bacteria to be inversely proportional to the speed at a given location, $\rho(x) = \rho(0)\frac{v(0)}{v(x)}$ [22]. That is, if, for some reason, bacteria move more slowly in one region of space they will, by virtue of that fact, accumulate in that area.

Due to their size bacteria cannot perform spatial comparisons of chemical concentrations; the chemicals they measure can diffuse across the length of the cell much faster than the cell itself moves, but they can perform temporal integrations to measure the change in concentration as they move [27]. It is often supposed that, due to a gradient of the concentration of some chemical, there is a change in tumbling rate, $\alpha(t)$, given by some response function:

$$\begin{aligned} \alpha(t) &= \alpha_0 + \int^t R(t-t')c(t')\mathrm{d}t' \quad \text{if} \int^t R(t-t')c(t')\mathrm{d}t' > 0 \\ &= \alpha_0 \qquad\qquad\qquad\qquad\qquad\quad \text{if} \int^t R(t-t')c(t')\mathrm{d}t' < 0. \end{aligned} \tag{2.9}$$

The dynamics of the bacteria can then be described by a drift velocity proportional to the gradient of the concentration of the chemical, $v_D = \kappa\nabla c$ [23–25]. For wild type *E. coli* responding to changes in aspartate concentration Segall et al. found the integral $\int^t R(t-t')\mathrm{d}t' = 0$, with a positive peak over $\sim 1s$ followed by a negative peak over $\sim 3s$, so the bacterium senses only changes in concentration and is blind to overall levels [28]—the approximate form is shown in figure 2.1. For the moment my work will not focus on chemotaxis, though chemotactic effects could be included within the framework described here. Instead, I aim to better understand the transition from a probability density for the position of a single bacterium to a density of many bacteria and to quantify the effects of noise, interactions between bacteria and their connection to longer time-scale population dynamics.

In investigating the population dynamics on long time scales we must consider not just the movement of our bacteria but also their birth and death processes. The life-cycle of bacteria turns out to be quite complex, and it is not always clear exactly what we mean by "death" in this context. There can be different stages at which the bacteria sequentially stop dividing, then stop moving; then at which they can be revived by being placed in more advantageous environments - for example with more nutrients; then a stage at which they cannot be revived but still maintain their physical integrity; then finally they undergo lysis. In most of

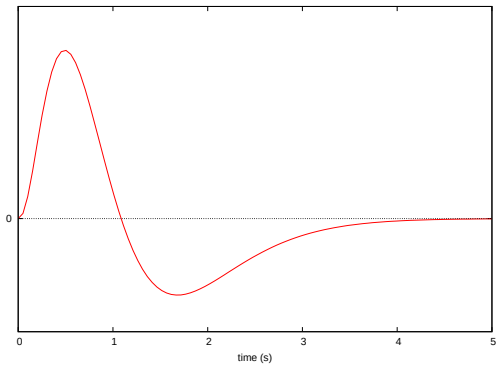

Figure 2.1: A sketch of the response function, $R(t)$, for wild type *E. coli*.

our modelling we will not distinguish between these processes but simply assume this complex behaviour, dependent on the local environmental conditions, can be approximated by logistic growth, where the birth and death rates depend on the local density of bacteria such as to lead to a fixed average carrying capacity. In chapter 7 we examine this approximation in more detail and find that the logistic approximation does not significantly compromise our results.

2.2.1 Prior Approaches to Bacterial Modelling

There have, in the past, been a number of attempts to predict the collective behaviour of bacteria from a study of their individual dynamics [2, 4, 22, 23]. Schnitzer [2] defined a continuous space and time model with, in one spatial dimension, the density of particles moving to the left at position x and time t, $L(x,t)$, and to the right, $R(x,t)$, evolving via the equations

$$\begin{aligned} \frac{\partial R(x,t)}{\partial t} &= -\frac{\partial vR}{\partial x} - \frac{\alpha R}{2} + \frac{\alpha L}{2} \\ \frac{\partial L(x,t)}{\partial t} &= \frac{\partial vL}{\partial x} + \frac{\alpha R}{2} - \frac{\alpha L}{2}, \end{aligned} \tag{2.10}$$

where v is the speed of the particles and α the tumbling rate for particles to change from right moving to left moving and vice versa. Defining a total particle density and current as the sum and difference of these respectively, he arrived at the continuity equation

$$\frac{\partial^2 \rho}{\partial t^2} = \frac{\partial}{\partial x}\left(v\frac{\partial v\,\rho}{\partial x}\right) + \alpha\frac{\partial J}{\partial x}, \tag{2.11}$$

where $\rho = R + L$ and $J = v(R - L)$. From this one can recover the results of his earlier work [22] for the equilibrium distribution of non-interacting, self-propelled particles with position dependent, but symmetric, rates. The paper goes on to generalise the approach to non-symmetric rates, higher dimensions and to include factors such as rotational Brownian motion and non-uniform rates amongst particles. The paper incorrectly assumes, however, that the single particle probability density, p, can simply be replaced with the particle density for many bacteria by replacing $\rho = N\,p$. Even before we add interactions to the model, however, this leads to equations for the bacterial density which do not take account of noise; ρ is an inherently fluctuating quantity, where p is not.

Cates and Tailleur [4] follow a different path from equations (2.10). They treat $L(x,t)$ and $R(x,t)$ as probability densities to find a single particle (bacterium) moving left, or right, at a given location and time. To move from this single particle description to a many-body problem they first take a diffusive approximation of their continuity equation for the probability density, $\frac{\mathrm{d}p(x,t)}{\mathrm{d}t} = -\nabla J(x,t)$, and recast it as an Ito-Langevin equation for the trajectory of the ith particle:

$$\dot{x}_i(t) = A(x_i) + C(x_i)\eta_i(t) \tag{2.12}$$

where A and C are given functions of the velocities and tumble rates related to the diffusivity, D, and drift, V, by $C^2 = 2D$ and $A = V + \partial D/\partial x_i$ and η is a Gaussian white noise. They then assume that in order to account for interactions between bacteria, A and C can then be replaced by counterparts which depend on the local density of bacteria, $A([\rho])$ and $C([\rho])$. Following Dean [29], they can then apply Ito's Theorem[1] and, after some algebra, arrive at the Fokker-Planck equation for the many-body probability:

$$\dot{\mathcal{P}}([\rho]) = \int \mathrm{d}x \frac{\delta}{\delta\,\rho}\partial_x \left[\rho\, V - D\partial_x\rho - D\rho\left(\partial_x \frac{\delta}{\delta\,\rho}\right)\right]\mathcal{P} \tag{2.13}$$

[1]Ito's theorem states that for any function $f(x_i)$, if x_i evolves via equation(2.12), then

$$\dot{f}(x_i) = (A + CL_i)\frac{\partial f}{\partial x_i} + (C^2/2)\frac{\partial^2 f}{\partial x_i^2}.$$

Identifying f with the density ρ then allows one to determine a continuity equation for the collective density. From this standard methods, as detailed in, for example, Gardiner [8], allow one to derive the Fokker-Planck equation.

where V and D are functionals of ρ, and hence to the microscopic parameters of the system. They attempt to map onto a thermal system by looking for solutions of the form $\mathcal{P} \propto e^{-\mathcal{F}([\rho])}$ and arrive at the condition

$$\frac{V[\rho(x)]}{D[\rho(x)]} = -\nabla \left(\frac{\delta \mathcal{F}_{ex}}{\delta\, \rho(x)} \right) \tag{2.14}$$

for such a mapping to exist. In the case of one dimensional, non-interacting particles with symmetric rates, this recovers Schnitzer's result, $\rho(x) \propto 1/v(x)$. Perhaps more interestingly, they also find solutions in some cases for interacting particles. For example, for a translationally invariant system with even parity ($v_{R/L}(\rho(x)) = v_{L/R}(\rho(-x))$), they find that under certain conditions the system is unstable to spinodal decomposition. If the rates are also symmetric the condition for spinodal decomposition is

$$\frac{\mathrm{d}v}{\mathrm{d}\rho} < -\frac{v}{\rho}. \tag{2.15}$$

If, for example, $v(x) = v_0\, e^{-\lambda\, \rho(x)}$, the system is unstable for all $\rho > 1/\lambda$, while if $v(x) = v_0\, e^{-\lambda\, \phi \arctan\left(\frac{\rho(x)}{\phi}\right)}$, $v(x)$ saturates at large ρ and the density can become stable again. For $\phi > 2/\lambda$ there is a window in which the system can phase separate into high and low density regions. Simulations of the Ito-Langevin equations agreed with this prediction, though they were not able to simulate the microscopic model directly; continuum simulations of this type would require a long time to complete (see section 3.1 for more details).

They also consider the case of non-interacting sedimentation, where $v_{R/L} = v \pm \mu_T\, m\, g$. At steady state they found that $\rho(x) = \rho(0) e^{-\kappa\, x}$ where $\kappa = \frac{-v_T\, \alpha}{v^2 - v_T^2}$. This shows an exponential profile, as in the case of a thermal system, but the system collapses to zero height at finite g, when $v_T \to v$. This is due to the fact that after this point both v_R and v_L point in the same direction. This is not the case in a thermal system. Further to this work they have generalised the results for sedimentation to higher dimensions and considered the case of trapping in a harmonic potential and rectification by a wall of funnels [3].

In chapter 3 I will lay out the mathematical framework to re-derive the steady state distribution and stability conditions beginning from a lattice based model. Utilising a lattice approach allows us to compute simulations far more efficiently and, importantly, to be able to extend our simulation results to more than one spatial dimension without a prohibitive increase in the computational cost.

Further, we can simulate the microscopic model directly, and not rely merely on the Ito-Langevin equation.

In chapter 6 I shall then use this framework to investigate the effects of interactions in the system and to examine the importance of non-locality and coarse-graining in the density field.

As the density dependence in the jump (and later tumble) rates can be implemented as a proxy for chemical signalling between bacteria, we expect that the response will depend on number of bacteria across some spatially extended region, which we shall have to account for through some form of coarse-graining of that field. (In fact as multiple bacteria cannot exist in the same position, any density dependent interaction necessarily requires some form of coarse-graining to move from a description of each bacterium's position to either a discrete or continuous field.) On lattice this calculation is easy to perform, though, as we shall see, the precise manner in which it is performed can have significant effects on the resulting steady state and dynamics.

2.2.2 Patterning in Bacterial Colonies

The formation of patterns by groups of organisms is ubiquitous in nature [30], from the clustering of ants [31] to the flocking of birds [32], and, as such, has attracted a significant interest from the communities of ecologists, mathematical biologists and, more recently, physicists. Given the wide range of situations and scales at which patterns are observed, it is natural to wonder whether for each situation evolution has led to specific pattern formation mechanisms that have to be studied separately or if there are generic mechanisms that cover a large range of situations. Though some example of such mechanisms, such as that discovered by Turing [33], have already been uncovered, most of the modelling literature has aimed at providing precise descriptions of given experiments, whose detailed complexity can hinder the observation of any underlying generic features.

A striking example is pattern formation in bacterial colonies, where relatively simple microscopic dynamics, such as the run-and-tumble swimming of *E. coli* [34–38], the swarming of *B. subtilis* [39] or *P. mirabilis* [40], or the gliding of myxobacteria *D. discoideum* [41], result at a macroscopic level in complex forms of organisation. These patterning processes rely on interactions between the bacteria that have various origins such as the secretion of chemotractants, steric

interactions, competition for food or quorum sensing. However, the question remains whether these interactions, despite their variety, play a similar role in different situations or, on the contrary, fulfil different purposes.

It was indeed recently argued [1], based on the study of a semi-phenomenological partial differential equation, that any microscopic mechanism resulting macroscopically in density dependent diffusivity of the bacterial population could trigger an instability. When damped by regulated division of cells, this instability results in patterns of fixed size. Whether microscopic interactions between bacteria generically result in such density dependent diffusivity, or on the contrary have to be fine-tuned to do so, remained unanswered. Furthermore, it was not clear how crucial the details of the modelling of the birth-death terms are to the patterning process. This is of great importance since, were the mechanism to be robust to generic microscopic changes of the bacterial dynamics, this would strongly support its importance while the opposite would shed doubt on its practical applications.

In chapter 7 we will show that the model is in fact robust to generic microscopic changes, that we can derive the phenomenological equation from which Cates et al. began from the microscopics and that the details of the birth-death process are not crucial to their mechanism. Indeed, we show that whilst in their previous work the target density of the growth term fell within the miscibility gap of the interactions, for expanding colonies a finite target density does not even need to exist to observe patterns on the time scale of the colony growth. It seems, therefore, that generic underlying features may be present in bacterial, and indeed other biological, patterning and that before more complicated explanations are invoked this much simpler mechanism should first be considered.

Chapter 3

Mathematical Frameworks

Having laid out the biological background to the systems we want to describe in chapter 2, in this chapter I hope to relay to the reader the basic mathematical and computational frameworks necessary to understand the results derived across the remainder of this work. I begin by briefly reviewing the scope and applicability of lattice models in statistical physics and explaining why we use them in this work despite the inherently continuous nature of the processes they are used to model. I then detail the field theoretic techniques utilised to move from that discrete, microscopic description to a more coarse-grained continuum level, before, finally, elaborating the algorithms used for my simulations and comparing their efficiency.

3.1 Lattice Models

Lattice models have, by now, a considerable history in statistical physics as prototypical examples of equilibrium and non-equilibrium dynamics and have been used to describe an extensive range of physical systems from traffic flow [42], to accumulation of wealth in macroeconomic models [43], to biophysical transport [44–46], while also revealing a wide variety of interesting physical phenomena from phase transitions, to symmetry breaking, to condensation. In addition, they can admit exact analytical calculation of statistical properties in some cases, as we will see in chapters 4 and 5 and are easily amenable to computational treatments. Lattice models are often far faster to simulate, as, for example, it is extremely easy to define a local density - one has only to record an array of the occupation numbers at each site. In contrast, in a continuum simulation much more complex

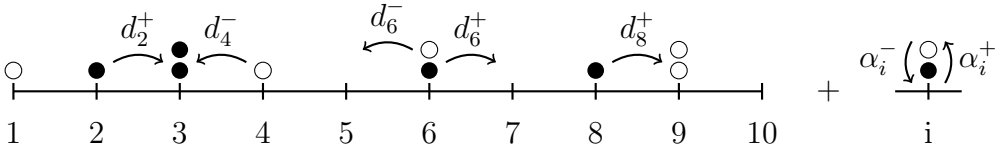

Figure 3.1: Presentation of the model. Filled circles represent right moving particles while unfilled circles denote left moving particles. Some of the possible transitions are illustrated on the figure.

calculations are required to determine a locally coarse-grained density. This is especially pertinent when working in more than one spatial dimension.

However, as the physical system we wish to model is inherently continuous, we need to take a continuum limit at some point in order to compare our calculations with experimental results; we will see in the coarse of this work that that is not always entirely straightforward and must be handled with some care to ensure the models are really equivalent.

3.1.1 Presentation of the Model: Run-and-tumble Dynamics on a Lattice

To model the finite persistence length in run-and-tumble dynamics on a lattice particles jump repeatedly in the same direction, $\mathbf{u}$, with rate $d(\mathbf{u})$ and change direction - tumble - with rate $\alpha(\mathbf{u})$; although in principle the tumble rate could also depend on the direction $\mathbf{u}'$ the particles face after the tumble ends, we do not consider this possibility here. In 1d, this means particles can be either right-going or left-going. Right-going particles jump with rate d_i^+ from site i to site $i+1$ and tumble with rate α_i^+. After a tumble, they become left-going particles with probability 1/2. The corresponding rates for left-going particles are called d_i^- and α_i^-, see figure 3.1. For now let us assume tumbles to be instantaneous. In reality the duration of tumbles is typically of the order of one tenth of the duration of runs [13]. There may be situations, however, where time spent tumbling may increase, and where the finite duration of a tumble may have an effect on the dynamics and steady state of the system. We shall consider the effect of finite tumble duration in section 6.4.

3.2 Deriving the Continuum Fluctuating Hydrodynamics

Let us start with the single particle process, and call $P(k,+)$ and $P(k,-)$ the probability to find a bacterium at site k going to the right and to the left respectively. The master equation reads

$$\begin{aligned}\partial_t P(k,+) &= d^+_{k-1}P(k-1,+) - d^+_k P(k,+) + \frac{\alpha^-_k}{2}P(k,-) - \frac{\alpha^+_k}{2}P(k,+)\\ \partial_t P(k,-) &= d^-_{k+1}P(k+1,-) - d^-_k P(k,-) - \frac{\alpha^-_k}{2}P(k,-) + \frac{\alpha^+_k}{2}P(k,+),\end{aligned} \tag{3.1}$$

where the first term on the right hand side of each equation describes the probability a particle jumped into site i, the second term the probability a particle vacated site i and the last two terms the probabilities that a particle changed direction.

Since we ultimately want to compare the run-and-tumble on lattice with its off lattice counterpart, let us first take the continuum limit of the master equation. Explicitly introducing the lattice spacing a and defining $x_k = ka$, the master equation (3.1) reads

$$\begin{aligned}\partial_t P(x_k,+) &= d^+(x_k-a)P(x_k-a,+) - d^+(x_k)P(x_k,+)\\ &\quad + \frac{\alpha^-(x_k)}{2}P(x_k,-) - \frac{\alpha^+(x_k)}{2}P(x_k,+)\\ \partial_t P(x_k,-) &= d^-(x_k+a)P(x_k+a,-) - d^-(x_k)P(x_k,-)\\ &\quad - \frac{\alpha^-(x_k)}{2}P(x_k,-) + \frac{\alpha^+(x_k)}{2}P(x_k,+).\end{aligned} \tag{3.2}$$

We are interested in cases where the typical run length is much longer that the lattice spacing so that $d^\pm \gg \alpha^\pm$. Furthermore, when $a \to 0$ while $v^\pm(x) = d^\pm(x)a$ remains finite, one gets, at leading order,

$$\begin{aligned}\partial_t P(x,+) &= -\nabla[v^+(x)P(x,+)] + \frac{\alpha^-(x)}{2}P(x,-) - \frac{\alpha^+(x)}{2}P(x,+) + \mathcal{O}(a)\\ \partial_t P(x,-) &= \nabla[v^-(x)P(x,-)] - \frac{\alpha^-(x)}{2}P(x,-) + \frac{\alpha^+(x)}{2}P(x,+) + \mathcal{O}(a),\end{aligned} \tag{3.3}$$

which is exactly the master equation for run-and-tumble bacteria considered previously off lattice [2, 4] which we began from in equation (2.10). Following the same path as there would lead (as described in section 2.2.1) to a Langevin equation for the density of a large but finite number of bacteria

$$\dot{\rho}(x,t) = -\nabla[\rho V - D\nabla\rho + \sqrt{2D\rho}\,\eta], \tag{3.4}$$

where

$$\begin{aligned} D &= \frac{\mathcal{D}}{1+\xi_1}; \qquad V = \frac{\mathcal{V}}{1+\xi_1}; \qquad \mathcal{V} = \frac{\alpha^- v^+ - \alpha^+ v^-}{2\alpha} - \frac{v}{\alpha}\nabla\frac{v^+v^-}{v} \\ \mathcal{D} &= \frac{v^+v^-}{\alpha}; \qquad \xi_1 = \frac{v^+}{2\alpha}\nabla\frac{v^+}{v} - \frac{v^-}{2\alpha}\nabla\frac{v^-}{v}, \end{aligned} \tag{3.5}$$

with $\alpha = (\alpha^+ + \alpha^-)/2$, $v = (v^+ + v^-)/2$. It was shown that (3.4) captures the steady state of the off lattice model exactly [4] and in section 3.2.1 we will show that it also describes the large scale behaviour of run-and-tumble bacteria on lattice. For (3.4) to derive from an effective free energy there must exist an excess free energy functional $\mathcal{F}_{ex}[\rho]$ that satisfies the condition[1] given in equation (2.14),

$$\frac{V}{D} = -\nabla\frac{\delta\mathcal{F}_{ex}}{\delta\rho(x)}, \tag{3.6}$$

which can be solved to give

$$\mathcal{F}_{ex}[\rho] = \int_0^L \mathrm{d}x \left\{ \rho(x) \left[\log\left(\frac{v^+v^-}{v}\right) + \frac{1}{2}\int_0^x \mathrm{d}x' \left(\frac{\alpha^+}{v^+} - \frac{\alpha^-}{v^-}\right)\right]\right\}, \tag{3.7}$$

as long as, for periodic boundary conditions, $\int_0^L \mathrm{d}x(\alpha^- v^+ - \alpha^+ v^-) = 0$. The total free energy is then given by

$$\mathcal{F}[\rho] = \int \mathrm{d}x \rho(\log\rho - 1) + \mathcal{F}_{ex}[\rho]. \tag{3.8}$$

Note that it is not always possible to write a free energy of this form for non-interacting particles in higher dimensions, nor, in general, for interacting systems. As we can see, there is no gradient term in this expression. This is due to the

[1] To arrive at this condition we need first to re-write equation (3.4) in the equivalent Fokker-Planck form. Then, to see if an effective free energy exists one can look for solutions of the form $\mathcal{P}([\rho]) \propto \exp(\mathcal{F})$. After accounting for the entropic term in the free energy, given by $\int \mathrm{d}x\rho(\log\rho - 1)$, the remaining (excess) free energy $\mathcal{F}_{ex}[\rho]$ must satisfy equation (3.6).

fact that when deriving the continuum limit, terms of order a and higher are neglected. If equation (3.4) leads to large gradients in the density, these higher order terms should be included and may alter the result; these terms control the surface tension, for example. These higher order terms could also violate condition (3.6). We shall now proceed using a field theoretic approach to derive the fluctuating hydrodynamics of the bacterial bath in a more general context. This will provide an alternative derivation of the non-interacting case to that presented previously in the literature [4], and will be able to account for the effect of interactions at the microscopic level.

3.2.1 Fluctuating Hydrodynamics for Interacting Bacteria

Bacteria do not exist as totally independent entities, free from the influence of other around them. To create any realistic model of their behaviour, therefore, we must be able to take into account interactions between bacteria. These interactions may come in a variety of forms and, for example, be purely steric in origin or mediated through the secretion and detection of some chemical components. To model the latter situation exactly one should explicitly consider additional fields for these components, and, indeed, that is what much of the previous literature in bacterial modelling has sought to do.

Here we will take a different course, however, and attempt to model the interactions through a general dependence of the jump and tumble rates on the local density - the occupation number at each site in a lattice context. That is we take the rates to be given by

$$d_i^{\pm} = d_i^{\pm}(\bar{n}_i^{\pm}); \qquad \alpha_i^{\pm} = \alpha_i^{\pm}(\bar{n}_i^{\pm}), \tag{3.9}$$

where $\bar{n}_i^{\pm}$ is a coarse-grained occupancy that depends linearly but non-locally on the occupancies of the whole lattice,

$$\bar{n}_i^{\pm} = \sum_j K_{i-j}^{\pm} n_j. \tag{3.10}$$

In general the coarse graining kernel $K_{i-j}^{\pm}$ could also be a function of lattice position though here we do not consider that situation, where the manner in which

the density is felt by the particles varies with position. In principle we should also consider the time delays involved in both the bacteria's response to the changing concentration of chemicals around them, which can be considerable when quorum sensing and gene expression are involved, and to the time required for chemical signals to themselves diffuse between bacteria. For computational and analytical simplicity, however, we assume the interactions to be instantaneous.

We aim at describing large scale behaviour, i.e. on a colony size, and so to derive a fluctuating hydrodynamics. In addition, this will allow us to compare again the phenomenology on and off lattice and to look for cases in which there is a "free-energy" like description, and for which we can thus characterise the steady state. We follow a field theoretic approach to derive a continuum Langevin equation for the system, from which we can deduce the appropriate Fokker-Planck equation and the steady-state distribution.

3.2.2 Field Theory for Non-Interacting Particles

To illustrate the technique we shall use to construct the fluctuating hydrodynamics for the full interacting case, let us first handle the non-interacting case and re-derive equation (3.4).

Field theoretic representations of lattice gases using bosonic coherent states were established in the 1970s following Doi and Peliti [47, 48]. The case where each site is limited to a single particle can be handled in some cases in this formalism [49], while more general finite occupancies could be handled using spin coherent states [50]. Alternatively, probabilistic approaches from mathematical physics have also been used [51–53]. Here we use an alternative derivation, based on an approach à la Jansen and De Dominicis [54, 55] transposed in the context of the master equation. This is very similar to the generating function approach used by Biroli and Lefevre [56]. Beginning with a process discrete in both time and space—with L lattice sites and N time steps—one writes the probability of

a trajectory, with fixed initial conditions, as

$$\begin{aligned} P[\{n_i^+(t_j), n_i^-(t_j)\}] \propto & \int \prod_{i=1}^{L}\prod_{j=1}^{N} \mathrm{d}J_i^+(t_j)\mathrm{d}J_i^-(t_j)\delta\big(n_i^+(t_{j+1}) - n_i^+(t_j) - J_i^+(t_j)\big) \\ & \times \delta\big(n_i^-(t_{j+1}) - n_i^-(t_j) - J_i^-(t_j)\big)P[\{J_i^+(t_j), J_i^-(t_j)\}] \\ & \propto \Big\langle \prod_{i=1}^{L}\prod_{j=1}^{N} \delta\big(n_i^+(t_{j+1}) - n_i^+(t_j) - J_i^+(t_j)\big) \\ & \times \delta\big(n_i^-(t_{j+1}) - n_i^-(t_j) - J_i^-(t_j)\big)\Big\rangle_{\mathbf{J}}, \end{aligned} \tag{3.11}$$

where $n_i^{\pm}(t_j)$ is the number of right $(+)$ of left $(-)$ moving particles at site i at time t_j, the $J_i(t_j)^{\pm}$ are the changes in the number of each type of particle at each site at each time step and the bold faced $\mathbf{J}$ denotes the average is over all J's. Re-writing the Dirac delta functions using imaginary Fourier representations this can be written as

$$\begin{aligned} P[\{n_i^+(t_j), n_i^-(t_j)\}] \propto & \int \prod_{i=1}^{L}\prod_{j=1}^{N} \mathrm{d}\hat{n}_i^+(t_j)\mathrm{d}\hat{n}_i^-(t_j) \\ & \times \Big\langle \exp\Big(\hat{n}_i^+(t_j)\big(n_i^+(t_{j+1}) - n_i^+(t_j) - J_i^+(t_j)\big) \\ & + \hat{n}_i^-(t_j)\big(n_i^-(t_{j+1}) - n_i^-(t_j) - J_i^-(t_j)\big)\Big)\Big\rangle_{\mathbf{J}} \\ & \propto \int \prod_{i=1}^{L}\prod_{j=1}^{N} \mathrm{d}\hat{n}_i^+(t_j)\mathrm{d}\hat{n}_i^-(t_j) \exp\Big(\hat{n}_i^+(t_j)\big(n_i^+(t_{j+1}) - n_i^+(t_j)\big) \\ & + \hat{n}_i^-(t_j)\big(n_i^-(t_{j+1}) - n_i^-(t_j)\big)\Big) \\ & \times \Big\langle \exp\Big(- \hat{n}_i^+(t_j)J_i^+(t_j) - \hat{n}_i^-(t_j)J_i^-(t_j)\Big)\Big\rangle_{\mathbf{J}}, \end{aligned} \tag{3.12}$$

where it should be noted that the conjugate fields $\hat{n}_i^{\pm}$ are imaginary. The average over the J's can then be calculated explicitly from the dynamics. Specifically, a right moving particle can jump from site i to site $i+1$ at time step j with probability $n_i^+(t_j)d_i^+\mathrm{d}t$, where $\mathrm{d}t$ is the duration of a time step. The corresponding values of the J's are $J_i(t_j) = -1$, $J_{i+1}(t_j) = 1$ and $J_{k\neq\{i,i+1\}} = 0$. Calculating all other moves and the probability that nothing happens, which corresponds to all

$J_i^{\pm} = 0$, we can write

$$\begin{aligned}\prod_{i=1}^{N}\left\langle e^{-\hat{n}_i^+(t_j)J_i^+(t_j)-\hat{n}_i^-(t_j)J_i^-(t_j)}\right\rangle_{\mathbf{J}} &= \prod_{i=1}^{N}\Big[1+n_i(t_j)^+d_i^+\left(e^{\hat{n}_i^+(t_j)-\hat{n}_{i+1}^+(t_j)}-1\right)\mathrm{d}t \\ &+ n_{i+1}^-(t_j)d_{i+1}^-\left(e^{\hat{n}_{i+1}^-(t_j)-\hat{n}_i^-(t_j)}-1\right)\mathrm{d}t \\ &+ \frac{\alpha_i^+}{2}n_i^+(t_j)\left(e^{\hat{n}_i^+(t_j)-\hat{n}_i^-(t_j)}-1\right)\mathrm{d}t \\ &+ \frac{\alpha_i^-}{2}n_i^-(t_j)\left(e^{\hat{n}_i^-(t_j)-\hat{n}_i^+(t_j)}-1\right)\mathrm{d}t\Big]. \qquad (3.13)\end{aligned}$$

As this is of the form $1 + k\mathrm{d}t$ we can approximate it as $\exp(k\mathrm{d}t)$ and write the probability for the trajectory as

$$\begin{aligned}P[\{n_i^+(t_j), n_i^-(t_j)\}] \propto \int\left(\prod_{i=1}^{L}\prod_{j=1}^{N}\mathrm{d}\hat{n}_i^+(t_j)\mathrm{d}\hat{n}_i^-(t_j)\right)\exp\Bigg[\sum_{i=1}^{L}\sum_{j=1}^{N} \\ \Big(\hat{n}_i^+(t_j)\left(n_i^+(t_{j+1})-n_i^+(t_j)\right)+\hat{n}_i^-(t_j)\left(n_i^-(t_{j+1})-n_i^-(t_j)\right) \\ +n_i(t_j)^+d_i^+\left(e^{\hat{n}_i^+(t_j)-\hat{n}_{i+1}^+(t_j)}-1\right)\mathrm{d}t \\ +n_{i+1}^-(t_j)d_{i+1}^-\left(e^{\hat{n}_{i+1}^-(t_j)-\hat{n}_i^-(t_j)}-1\right)\mathrm{d}t \\ +\frac{\alpha_i^+}{2}n_i^+(t_j)\left(e^{\hat{n}_i^+(t_j)-\hat{n}_i^-(t_j)}-1\right)\mathrm{d}t \\ +\frac{\alpha_i^-}{2}n_i^-(t_j)\left(e^{\hat{n}_i^-(t_j)-\hat{n}_i^+(t_j)}-1\right)\mathrm{d}t\Big)\Bigg]. \qquad (3.14)\end{aligned}$$

We can then take a continuous time limit and make the substitutions

$$n_i^{\pm}(t_{j+1})-n_i^{\pm}(t_j)\to\dot{n}_i^{\pm}\mathrm{d}t; \qquad \sum_{j=1}^{N}\mathrm{d}t\to\int_0^{T=N\mathrm{d}t}\mathrm{d}t; \qquad \prod_{j=1}^{N}\mathrm{d}\hat{n}_i^{\pm}(t_j)\to\mathcal{D}\hat{n}_i^{\pm}. \qquad (3.15)$$

The probability of a trajectory can then be written

$$P[\{n_i^+(t), n_i^+(t)\}]\propto\int\prod_i\mathcal{D}[\hat{n}_i^+,\hat{n}_i^-]e^{-S[\mathbf{n}^+,\mathbf{n}^-,\hat{\mathbf{n}}^+,\hat{\mathbf{n}}^-]}, \qquad (3.16)$$

where the action S is given by

$$\begin{aligned} S &= -\int_0^T \mathrm{d}t \sum_i \Big[\hat{n}_i^+ \dot{n}_i^+ + \hat{n}_i^- \dot{n}_i^- + n_i^+ d_i^+ \left(e^{\hat{n}_i^+ - \hat{n}_{i+1}^+} - 1 \right) + n_{i+1}^- d_{i+1}^- \left(e^{\hat{n}_{i+1}^- - \hat{n}_i^-} - 1 \right) \\ &+ \frac{\alpha_i^+}{2} n_i^+ \left(e^{\hat{n}_i^+ - \hat{n}_i^-} - 1 \right) + \frac{\alpha_i^-}{2} n_i^- \left(e^{\hat{n}_i^- - \hat{n}_i^+} - 1 \right) \Big]. \end{aligned} \tag{3.17}$$

Note that generic changes of variables in (3.16) will result in Jacobians. If these do not depend on the fields, $n_i^\pm$ and $\hat{n}_i^\pm$, they can be subsumed into the normalisation of the path integral but they must be handled with care otherwise.

We further simplify by considering symmetric, constant, rates $d_i^+ = d_i^- = d$ and $\alpha_i^+ = \alpha_i^- = \alpha$; the more general case causes little conceptual difficulty but is considerably more cumbersome as an illustration. Let us then introduce the new variables

$$\rho_i = n_i^+ + n_i^-; \quad J_i = d(n_i^+ - n_i^-); \quad \hat{\rho}_i = \frac{1}{2}(\hat{n}_i^+ + \hat{n}_i^-); \quad \hat{J}_i = \frac{1}{2}(\hat{n}_i^+ - \hat{n}_i^-) \tag{3.18}$$

The action can then be written as

$$\begin{aligned} S &= -\int_0^T \mathrm{d}t \sum_i \Big[\hat{\rho}_i \dot{\rho}_i + \frac{1}{d} \hat{J}_i \dot{J}_i + \frac{d}{2} \rho_i \left(e^{-(\hat{\rho}_{i+1} - \hat{\rho}_i + \hat{J}_{i+1} - \hat{J}_i)} + e^{\hat{\rho}_{i+1} - \hat{\rho}_i - (\hat{J}_{i+1} - \hat{J}_i)} - 2 \right) \\ &+ \frac{J_i}{2} \left(e^{-(\hat{\rho}_{i+1} - \hat{\rho}_i + \hat{J}_{i+1} - \hat{J}_i)} - e^{\hat{\rho}_{i+1} - \hat{\rho}_i - (\hat{J}_{i+1} - \hat{J}_i)} \right) \\ &+ \frac{d}{2} (\rho_{i+1} - \rho_i - \frac{J_{i+1} - J_i}{d}) \left(e^{\rho_{i+1} - \hat{\rho}_i - (\hat{J}_{i+1} - \hat{J}_i)} - 1 \right) \\ &+ \frac{\alpha \rho_i}{4} \left(e^{2\hat{J}_i} + e^{-2\hat{J}_i} - 2 \right) + \frac{\alpha J_i}{4d} \left(e^{2\hat{J}_i} - e^{-2\hat{J}_i} \right) \Big]. \end{aligned} \tag{3.19}$$

The continuum limit can be taken by explicitly introducing the lattice spacing a and making the substitutions

$$\begin{aligned} \rho_i \to a\rho(x); \quad \hat{\rho}_i \to \hat{\rho}(x); \quad d \to v a^{-1}; \quad \textstyle\sum_i \to \int_0^{\ell = La} \mathrm{d}x a^{-1}; \\ J_i \to J(x); \quad \hat{J}_i \to \hat{J}(x); \quad \nabla_i \to a\nabla + \tfrac{1}{2} a^2 \Delta, \end{aligned} \tag{3.20}$$

where ∇_i is the discrete gradient, e.g. $\nabla_i \rho_i = \rho_{i+1} - \rho_i$, and ℓ is the system length. After Taylor expanding the action in powers of the lattice spacing, taking a diffusive rescaling of time and space and properly rescaling the fields,

see Appendix A, we find that the fluctuating hydrodynamic action is given by

$$S_0 = -\int_0^\tau \mathrm{d}t \int_0^1 \mathrm{d}x \left(\hat{\rho}\dot{\rho} - v\rho\nabla\hat{J} - J\nabla\hat{\rho} + \alpha\rho\hat{J}^2 + \frac{\alpha J\hat{J}}{v} \right), \tag{3.21}$$

which is invariant under a further diffusive rescaling of space and time.

Going back to the definition of the probability (3.16), we can then work backwards to recover a continuity equation for ρ from our action [50]. Starting from

$$P[\{\rho(x,t), J(x,t)\}] = \frac{1}{\tilde{Z}} \int \mathcal{D}[\hat{\rho}, \hat{J}] e^{-S_0[\rho, J, \hat{\rho}, \hat{J}]}, \tag{3.22}$$

one can remove the quadratic term $\hat{J}^2$ by introducing a new field $\eta(x,t)$ via a Hubbard-Stratonovich transformation so that

$$P[\{\rho(x,t), J(x,t)\}] = \frac{1}{\tilde{Z}} \int \mathcal{D}[\hat{\rho}, \hat{J}, \eta] e^{-S_0[\rho, J, \hat{\rho}, \hat{J}, \eta]}, \tag{3.23}$$

where the new action now reads (after some integration by parts)

$$S_0 = -\int_0^\tau \mathrm{d}t \int_0^1 \mathrm{d}x \left(\hat{\rho}\dot{\rho} + v\nabla\rho\hat{J} + \hat{\rho}\nabla J + \sqrt{2\alpha\rho}\,\eta\hat{J} + \frac{\alpha J\hat{J}}{v} - \frac{1}{2}\eta^2 \right). \tag{3.24}$$

The integral over $\hat{\rho}$ and $\hat{J}$ then leads to

$$P[\{\rho(x,t), J(x,t)\}] \propto \int \mathcal{D}[\eta]\delta(\dot{\rho} + \nabla J)\, \delta\Big(\frac{\alpha}{v} J + \sqrt{2\alpha\rho}\,\eta + \nabla v\rho \Big)\, e^{-\frac{1}{2}\int \mathrm{d}x\mathrm{d}t\, \eta^2}, \tag{3.25}$$

where the delta functions impose the two dynamic field equations

$$\dot{\rho} = -\nabla J; \qquad J = -D\nabla\rho + \sqrt{2D\rho}\,\eta; \qquad D = \frac{v^2}{\alpha}. \tag{3.26}$$

Given its weight in (3.25), $\eta(x,t)$ is a Gaussian white noise:

$$\langle \eta(x,t)\eta(x',t') \rangle = \delta(x-x')\delta(t-t'). \tag{3.27}$$

This is consistent with the calculation off-lattice for non-interacting, homogeneous and isotropic systems and validates the results obtained previously, see equation (3.4).

Fluctuating Hydrodynamics and Large Deviation Functions

Before going any further, let us make a brief detour to consider the connection with the standard fluctuating hydrodynamics approach considered in the mathematics literature [57]. Let us first note that from the definition of the continuum limit, one has

$$N = \sum_i \rho_i = \int_0^1 \mathrm{d}x \rho(x) \tag{3.28}$$

The integral of the density field is thus an extensive variable. On the other hand, the density field considered by mathematicians is often defined by

$$\rho(x) = \frac{1}{\ell} \sum_i \rho_i \delta(x - ai) \tag{3.29}$$

and satisfies the normalisation condition

$$\int \mathrm{d}x \rho(x) = \frac{N}{\ell} \tag{3.30}$$

To make the connection between the two approaches, it is thus natural to rescale our density term to make the extensivity apparent: $\rho \to \ell\rho$. To ensure that the conservation equation still has the form $\dot{\rho} = -\nabla J$, one must also rescale the current field $J \to \ell J$. Before introducing the $\eta(x,t)$ field, the action thus reads

$$S_0 = -\ell \int_0^\tau \mathrm{d}t \int_0^1 \mathrm{d}x \left(\hat{\rho}\dot{\rho} - v\rho\nabla\hat{J} - J\nabla\hat{\rho} + \alpha\rho\hat{J}^2 + \frac{\alpha J\hat{J}}{v} \right). \tag{3.31}$$

One can again introduce the noise field and integrate over the conjugate fields $\hat{\rho}$ and $\hat{J}$ to get

$$P[\{\rho(x,t), J(x,t)\}] \propto \int \mathcal{D}[\eta] \delta(\dot{\rho} + \nabla J)\ \delta\Big(\frac{\alpha}{v} J + \sqrt{2\alpha\rho}\,\eta + \nabla v\rho\Big)\ e^{-\frac{\ell}{2}\int \mathrm{d}x\mathrm{d}t\ \eta^2}. \tag{3.32}$$

Interestingly, the fields are now all intensive, and the smallness of the noise does not come from a $\sqrt{\rho}$ versus ρ noise prefactor, but from its explicit variance, read in the Gaussian weight:

$$\langle \eta(x,t)\eta(x',t') \rangle = \frac{1}{\ell} \delta(x - x')\delta(t - t'). \tag{3.33}$$

This is the usual fluctuating hydrodynamics, as considered, for instance, by Bertini et al. [57]. In the large size limit, the first order correction to the deterministic equation in a $1/\ell$ expansion is given by the addition of the noise term $\sqrt{2D\rho}$. This noise is typically of order $1/\sqrt{\ell}$, i.e. trajectories of probability of order 1 have $\ell\eta^2$ of order 1. Large deviations correspond to trajectories where the noise can be of order one. They yield probabilities of order $\mathcal{O}(\exp(-\ell))$, and remain described by the fluctuating hydrodynamics. Even less likely trajectories of order $\mathcal{O}(\exp(-\ell)^2)$ are outside of the scope of this description.

3.2.3 Field Theory for Interacting Particles

Consider now the case of interacting particles where the jump and tumble rates depend on the occupation numbers of each lattice site. Our velocity is then modified to

$$v^{\pm}(x) \to v^{\pm}(\bar{\rho}^{\pm}(x), x), \tag{3.34}$$

and the tumble rate to

$$\alpha^{\pm}(x) \to \alpha^{\pm}(\bar{\rho}^{\pm}(x), x), \tag{3.35}$$

with $\bar{\rho}^{\pm}(x)$ given by an integral over the density

$$\bar{\rho}^{\pm}(x) = \int K^{\pm}(x-y)\rho(y)\mathrm{d}y, \tag{3.36}$$

where $K^{\pm}(x-y)$ are some kernels which account for how the coarse-grained densities $\bar{\rho}^{\pm}(x)$ depend on $\rho(x)$.

Following the same path as that followed in section 3.2.2 for the non-interacting case, one gets for the action

$$\begin{aligned} S &= -\int \mathrm{d}t\mathrm{d}x \left[\hat{\rho}\dot{\rho} - \frac{v^+(\bar{\rho}^+)v^-(\bar{\rho}^-)}{v(\bar{\rho}^+,\bar{\rho}^-)}\rho\nabla\hat{J} - J\nabla\hat{\rho} + \frac{\alpha^+(\bar{\rho}^+)v^-(\bar{\rho}^-)+\alpha^-(\bar{\rho}^-)v^+(\bar{\rho}^+)}{v(\bar{\rho}^+,\bar{\rho}^-)}\rho\hat{J}^2\right. \\ &+ \left.\frac{\alpha(\bar{\rho}^+,\bar{\rho}^-)}{v(\bar{\rho}^+,\bar{\rho}^-)}J\hat{J} + \ell\frac{\alpha^+(\bar{\rho}^+)v^-(\bar{\rho}^-)-\alpha^-(\bar{\rho}^-)v^+(\bar{\rho}^+)}{v(\bar{\rho}^+,\bar{\rho}^-)}\rho\hat{J}\right], \end{aligned} \tag{3.37}$$

where $v = (v^+ + v^-)/2$ and $\alpha = (\alpha^+ + \alpha^-)/2$. The factor of ℓ in the final term implies that, for the diffusive scaling to hold, at a scale ℓ, the asymmetry $\alpha^+(\bar{\rho}^+)v^-(\bar{\rho}^-) - \alpha^-(\bar{\rho}^-)v^+(\bar{\rho}^+)$ must be of order $1/\ell$. This is reminiscent of the ASEP, where if the bias is much smaller than $1/\sqrt{\ell}$ the diffusive scaling holds

(Edwards-Wilkinson universality class), as in the symmetric exclusion process, but for larger asymmetries the dynamic exponent z is the same as Kardar-Parisi-Zhang scaling [58]. Integrating over $\hat{\rho}$ and $\hat{J}$ now yields the set of field equations

$$\dot{\rho} = -\nabla J; \qquad J = -D\nabla\rho - V\rho + \sqrt{\frac{v(\alpha^+ v^- + \alpha^- v^+)}{\alpha^2}}\rho\eta, \tag{3.38}$$

with

$$D = \frac{v^+ v^-}{\alpha}; \qquad V = \ell\frac{\alpha^- v^+ - \alpha^+ v^-}{2\alpha} - \frac{v}{\alpha}\nabla\frac{v^+ v^-}{v} \tag{3.39}$$

This formalism will later be used to analyse the effect of interactions on the large scale behaviour of a system of run-and-tumble particles. In order to verify that these calculations are correct, they will be compared to results obtained from direct numerical simulation of the underlying microscopic dynamics. The details of these simulations are briefly described in the next section.

3.3 Simulation Methods

Many of the analytical results contained in this work are compared with direct simulation of the underlying microscopic dynamics to verify the approximations we apply at various times. The analytical work is often guided by the results of these simulations and much of the justification for the use of a lattice approach is based upon the increased efficiency of the simulations, it is therefore important to be clear as to the workings of those simulations and we detail the methodology of their algorithms below.

3.3.1 Discrete Time Monte Carlo Simulations

The simplest way to reproduce the microscopic dynamics, and maintain the correct stochastic treatment, is to perform a type of discrete time Markov Chain Monte Carlo. We evolve forwards through time a particular realisation of the master equation dynamics in each simulation run. To do so we follow the basic procedure described below.

Begin by selecting one particular site (or particle) at random from a uniform distribution, so that for N sites each should be updated, on average, once per N iterations. Next determine the probability for some update to occur at the given site within the time-step dt, that is for each possible transition out of the current

configuration calculate the relevant probability. If the rate of each transition from a configuration $\mathcal{C}$ to $\mathcal{C}'$ is given by $W(\mathcal{C} \to \mathcal{C}')$ the probability of each transition is given by $P(\mathcal{C} \to \mathcal{C}') = W(\mathcal{C} \to \mathcal{C}')\mathrm{d}t$ where the time-step $\mathrm{d}t$ is fixed for the entire simulation and chosen such that the total probability to leave any configuration is never greater than 1, i.e.

$$\mathrm{d}t = \frac{1}{\max\left(\sum_{\mathcal{C}'} W\left(\mathcal{C} \to \mathcal{C}'\right), \mathcal{C}\right)}. \tag{3.40}$$

Place the possible actions taken to alter the configuration of the system in some, arbitrary, order, and determine which action if any is performed by picking a random number between 0 and 1. If the number is between 0 and $W(\text{action 1})\mathrm{d}t$ perform action 1, if it is between $W(\text{action 1})\mathrm{d}t$ and $W(\text{action 1})\mathrm{d}t + W(\text{action 2})\mathrm{d}t$ perform action 2, and so on, if it is greater than $\sum_i W(\text{action i})\mathrm{d}t$ leave the system unchanged. Finally update the system clock $t \to t + \mathrm{d}t$ and repeat until t is greater than the desired run-time.

3.3.2 Continuous Time Monte Carlo Simulations

In many circumstances, discussed at the end of this section, the discrete time procedure, though simple to implement, may not be efficient to run. In such circumstances it may be more appropriate for one to use a continuous time procedure instead.

In this case we must begin by calculating, for each and every site a rate for some update to take place,

$$R(\mathbf{x}) = \sum_{\mathcal{C}'} W_{\mathbf{x}}\left(\mathcal{C} \to \mathcal{C}'\right), \tag{3.41}$$

where $W_{\mathbf{x}}(\mathcal{C} \to \mathcal{C}')$ is the rate for an event to occur at a position $\mathbf{x}$ which takes the system from state $\mathcal{C}$ to $\mathcal{C}'$. We then draw a time till the next event for each site from a Poisson distribution of parameter $R(\mathbf{x})$,

$$t(\mathbf{x}) = -\frac{1}{R(\mathbf{x})}\log(U), \tag{3.42}$$

where U is a random number sampled uniformly between 0 and 1. These times are ordered in a structure known as a heap. This is a complete binary tree where

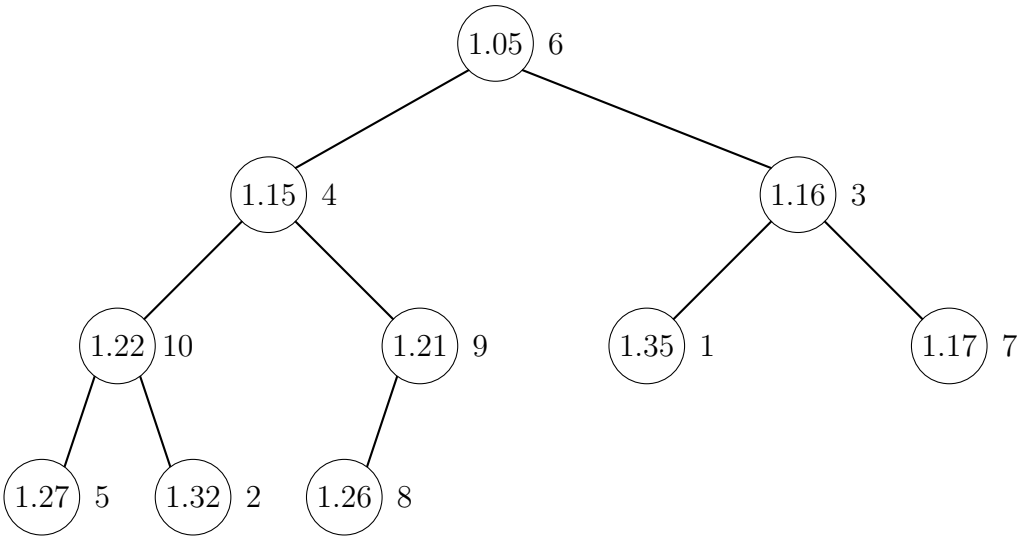

Figure 3.2: An example heap for a lattice of 10 sites. The time of the next event at each site is shown inside the nodes, the position on the lattice is listed to the right of each node. Note that the time at the parent of each node is smaller than that of the children, but the children are not ordered.

each node is less than or equal to that of both its children. Thus the site with the smallest time till the next event is always at the top of the heap and for N objects in the heap the time to sort them scales as order $\log N$ - for comparison a simple linear ordering of sites would require of order N moves to re-sort after each update. See figure 3.2 for an example.

We pick the site with the smallest time and set the system clock equal to this time. Having chosen a site to update we then choose which action to perform at that site by the same method as for the discrete time procedure but replacing dt with $R(\mathbf{x})$ so that each configuration change occurs with probability

$$P(\mathcal{C} \to \mathcal{C}') = \frac{W(\mathcal{C} \to \mathcal{C}')}{\sum_{\mathcal{C}'} W(\mathcal{C} \to \mathcal{C}')} \tag{3.43}$$

so that $\sum_{\mathcal{C}'} P(\mathcal{C} \to \mathcal{C}') = 1$, and there are no rejected updates, the configuration is always altered. We then draw a new time for every site whose configuration has been altered,

$$t'(\mathbf{x}) = t(\mathbf{x}) - \frac{1}{R(\mathbf{x})} \log(\mathrm{U}), \tag{3.44}$$

and reorder the heap. We iterate the procedure by picking the site with the new smallest time and repeat until the system time - and, necessarily, the time at

every site - is greater than the desired run-time.

3.3.3 Comparison of the Two Simulation Procedures

Though a continuous time description more closely describes the real dynamics of the particles we wish to simulate, we see no significant difference between the two procedures. Therefore, in the simulations presented in this work both continuous and discrete time algorithms are used for different problems, dependent on which is expected to be the most efficient procedure for the specific conditions under investigation.

Additionally, we may wish to record the position of each particle at each time-step, if we wish to track specific particles, say, or simply the occupation numbers at each site, if we do not. For the discrete time code this makes no difference to the efficiency of the code, and requires only minor alterations to the source code. For the continuous time code, however, instead of storing a heap of L sites, each with a time until any one of the n_i particles at that site moves or changes state, we must store a heap of $N = \langle n \rangle L$ particles, with a time until each one, individually, changes. Recording the position of each particle drastically increases the time it takes to run the simulations. If there are, for example, an average of 100 particles per site, $\langle n \rangle_i = 100$ and the jump rate depends on the occupation number of the site, then whenever any particle is moved, of order 100 new times must be drawn. If we care only about the rate for an event to happen at a given site, however, of order 1 new time must be drawn per particle moved. This is clearly a significant difference in efficiency.

Similarly, when the jump rate at a given site depends not just on the occupation number at that site but at many sites, the continuous time code may require many new times to be drawn and become, correspondingly, inefficient. In those situations the discrete time code will be used.

On the other hand, where the lattice is densely packed, or when there is for some other reason a large difference between the maximum escape rate from a configuration and the average escape rate, the discrete time code will generate many rejected events, where an update is attempted but no action happens. In this case the continuous time code may be more efficient.

In all cases the two sets of code have been compared numerically and found to produce identical results, the only difference appearing in the computational

time required to generate such results.

Chapter 4

Non-Interacting Active Particles

The jump and tumble rates defined in section 3.1.1 may, in general, depend on the occupation numbers of any lattices sites. Through this we may introduce interactions to our system and consider the general case of N interacting bacteria. Before we begin to deal with such complex cases in chapter 5, however, let us look at the limiting case of non-interacting particles, where all interesting and non-trivial effects come from heterogeneities or anisotropies in the jump and tumble rates, and we can calculate the steady state probability distributions exactly.

For non-interacting particles, one can always handle the single particle case first and compute the average occupancy $\rho_i^{\pm}$ of left $(-)$ or right $(+)$ moving particles on site i. As shown below, the steady-state distribution of n particles is then given by a product on each site of a multinomial distribution of parameters $\rho_i^{\pm}$.

4.1 Exact Results for Steady State

To calculate the steady state distribution we start from the continuity equation

$$\frac{\mathrm{d}}{\mathrm{d}t}\big[P(i,+) + P(i,-)\big] = J_{i-1,i} - J_{i,i+1}, \tag{4.1}$$

where $J_{i,i+1}$ is the net probability flux between sites i and $i+1$, that is

$$J_{i,i+1} = d_i^+ \, P(i,+) - d_{i+1}^- \, P(i+1,-). \tag{4.2}$$

As we are only after the steady state distribution we take the time derivative on the left hand side of equation (4.1) to be zero, so all currents $J_{i,i+1}$ are constant and equal to some J fixed by the boundary conditions.

The master equation for the density of left-moving particles at site i reads

$$0 = d_{i+1}^{-}\, P(i+1,-) - d_i^{-}\, P(i,-) + \frac{\alpha_i^{+}}{2} P(i,+) - \frac{\alpha_i^{-}}{2} P(i,-). \tag{4.3}$$

Using (4.2) to eliminate the first term on the right hand side of equation (4.3), which is the only term to depend on site $i+1$, we can establish a relationship between the number of left and right moving particles on site i at steady state:

$$P(i,+)\left(d_i^{+} + \frac{\alpha_i^{+}}{2}\right) - P(i,-)\left(d_i^{-} + \frac{\alpha_i^{-}}{2}\right) = J. \tag{4.4}$$

Equation (4.4), along with equation (4.2), leads to the recursion relation for right moving particles

$$P(i+1,+) = \frac{d_i^{+}}{d_{i+1}^{-}} \frac{2\, d_{i+1}^{-} + \alpha_{i+1}^{-}}{2\, d_{i+1}^{+} + \alpha_{i+1}^{+}} P(i,+) - J \frac{\alpha_{i+1}^{-}}{d_{i+1}^{-}(\alpha_{i+1}^{+} + 2\, d_{i+1}^{+})}, \tag{4.5}$$

which can be solved to yield

$$\begin{aligned} P(i,+) &= \prod_{j=1}^{i-1} \left(\frac{d_j^{+}}{d_{j+1}^{-}} \frac{2\, d_{j+1}^{-} + \alpha_{j+1}^{-}}{2\, d_{j+1}^{+} + \alpha_{j+1}^{+}} \right) \Bigg(P(1,+) \\ &\quad - J \sum_{k=1}^{i-1} \frac{\alpha_{k+1}^{-}}{d_{k+1}^{-}\,(2\, d_{k+1}^{+} + \alpha_{k+1}^{+}) \prod_{m=1}^{k} \left(\frac{d_j^{+}}{d_{j+1}^{-}} \frac{2\, d_{j+1}^{-} + \alpha_{j+1}^{-}}{2\, d_{j+1}^{+} + \alpha_{j+1}^{+}} \right)} \Bigg) \end{aligned} \tag{4.6}$$

$$P(i,-) = \frac{\left(2\, d_i^{+} + \alpha_i^{+}\right) P(i,+) - J}{2\, d_i^{-} + \alpha_i^{-}}. \tag{4.7}$$

The probability to find a particle at any position and in either state can then be calculated by noting that the total distribution must be normalised, i.e. $\sum_i [P(i,+) + P(i,-)] = 1$ and that J is imposed by the boundary conditions. For example, closed boundaries require that $J = 0$, while for periodic boundaries we have the additional constraint that $P(L+1,\pm) = P(1,\pm)$. Note that the probability densities for left and right moving particles do not have to be the same, and, in general, will not be.

The probability of a given configuration $P(\{n_i^+, n_i^-\})$, is given by

$$P\left(\{n_i^+, n_i^-\}\right) = N! \prod_i \frac{P(i,+)^{n_i^+} P(i,-)^{n_i^-}}{n_i^+!\, n_i^-!} \delta\left(\sum_i (n_i^+ + n_i^-) - N\right), \tag{4.8}$$

where N is the total number of particles in the system. If we call the average number of right or left going particles on a site $\rho_i^\pm = N\, P(i,\pm)$, then in the limit where $N \to \infty$ and $L \to \infty$, so that $P(i,\pm) \to 0$, but $\rho_i^\pm$ remains finite, the probability of a configuration is given by

$$P\left(\{n_i^+, n_i^-\}\right) = \prod_i \frac{(\rho_i^+)^{n_i^+} \exp(-\rho_i^+)}{n_i^+!} \frac{(\rho_i^-)^{n_i^-} \exp(-\rho_i^-)}{n_i^-!}. \tag{4.9}$$

4.2 Examples

Where not stated otherwise the simulations we present here use reflecting boundary conditions; if a particle tries to jump off one end of the lattice it is, instead, kept where it is but turned around. All simulations are performed with continuous-time Monte Carlo algorithms.

4.2.1 Position Dependent Rates with Closed Boundaries

First, we consider the case of a position dependent, but isotropic, jump rate and a constant tumbling rate. As a simple example we use a top-hat function for jump rate such that $d_i^\pm = 1 + 10\,\theta(i-150)\,\theta(350-i)$, where $\theta(x)$ is the Heaviside step function. Both the continuum and lattice theory predict that the average occupancy should be inversely proportional to the velocity,

$$\rho(x) \propto \frac{1}{v(x)}; \qquad \rho_i = \rho_i^+ + \rho_i^- \propto \frac{1}{d_i}. \tag{4.10}$$

The results of the simulations and both predictions are shown in figure 4.1 (main).

In contrast to the jump rate, simply making the tumble rate depend on position but maintaining isotropy has no effect on the predicted distribution. Note that the free energy in equations (3.7) and (3.8) has no dependency on α for isotropic rates. Using the same form as for the position dependent jump rate in our simulations this can be verified numerically, see figure 4.1 (inset).

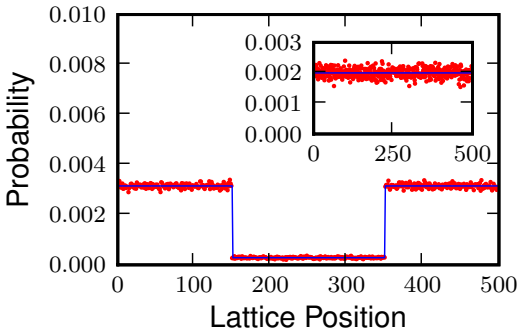

Figure 4.1: **Main:** Steady state probability distribution for constant tumble rates, $\alpha_i^{\pm} = 1$ and isotropic jump rates $d_i^{\pm} = 1 + 10\,\theta(i - 150)\,\theta(350 - i)$. Data averaged from the positions of $400,000$ particles. **Inset:** Steady state probability distribution for constant jump rates, $d_i^{\pm} = 10$, and tumble rates $\alpha_i^{\pm} = \theta(i - 150)\,\theta(350 - i)$. Data from $100,000$ particles. In both figures simulation data are shown in red and the theory prediction (equation (4.10)) in blue. Both simulations performed on a lattice of 500 sites and recorded at $t = 5000$.

4.2.2 Direction Dependent Rates with Closed Boundaries: Sedimentation and Chemotaxis

In many physical situations, however, bacteria do not move unbiasedly but are affected by their external conditions. This may be due, for example, to sedimentation due to gravity, where there is an asymmetry in jump rates between left and right (or up and down) moving particles. Another case of interest may be anisotropic tumble rates. Bacteria undergoing chemotaxis often vary their tumble rate dependent on whether they are travelling up or down a chemical gradient. Though a simple asymmetry in tumble rate does not fully capture this behaviour, we do see particles preferentially move in the direction of a lower tumble rate, as would be expected[1].

These two cases show qualitatively the same behaviour, with an exponential decay in the probability to find a particle at a given position in the unfavoured direction. From equations (4.6) and (4.7), the probabilities for left or right going

[1]Whether the asymmetry appears in the tumble or jump rate makes no qualitative difference to the results, and thus only the results for asymmetric jump rates are presented here (in figure 4.2); taking $\alpha_i^{+} \neq \alpha_i^{-}$ would produce the same effect.

particles on lattice are

$$P(i,\pm) \propto \exp\left[i \log\left(\frac{d^+\,(2\,d^- + \alpha^-)}{d^-\,(2\,d^+ + \alpha^+)}\right)\right] \equiv \exp\left[i\,\lambda_{\text{latt}}\right], \tag{4.11}$$

while in the continuum case the probability density is given (from equation (3.7)) by

$$\rho(x) \propto \exp\left[x\frac{\alpha^-\,v^+ - \alpha^+\,v^-}{2\,v^+\,v^-}\right] \equiv \exp\left[x\,\lambda_{\text{cont}}\right]. \tag{4.12}$$

For expositional simplicity we consider homogeneous rates here. To examine the difference between the lattice and continuum results, consider, for example, the case of sedimentation, where $d^\pm = d_0(1 \pm \epsilon)$ and $\alpha^\pm = \alpha_0$. The decay constant in the continuum limit is then

$$\lambda_{\text{cont}} = \frac{\alpha_0\,\epsilon}{v_0(1-\epsilon^2)}, \tag{4.13}$$

and the lattice decay constant is given by

$$\lambda_{\text{latt}} = \frac{\alpha_0\,\epsilon}{d_0(1-\epsilon^2)} - \frac{\epsilon\,\alpha_0^2}{2\,d_0^2(1-\epsilon^2)^2} + \mathcal{O}\left(\frac{\alpha_0}{d_0}\right)^3. \tag{4.14}$$

We can see then that the two decay lengths will be equal if the jump rate is much larger than the tumble rate, i.e. for average run lengths much larger than the lattice spacing. Both decay constants tend to zero as the asymmetry disappears, $\epsilon \to 0$, but the ratio $\lambda_{\text{latt}}/\lambda_{\text{cont}}$ remains finite.

In our simulations we use $d_i^\pm = 10 \mp 1$ and $\alpha_0 = 1$, so the drift velocity, the external bias, is much less than the self-propelled speed, i.e. $\left|d_i^+ - d_i^-\right| \ll d^\pm$. The continuum theory predicts the distribution to be $\rho(x) \propto \exp(-x/99)$, while the lattice theory predicts $P(i) \propto (207/209)^i$. Both predictions are shown, along with the simulation data in figure 4.2. The ratio of decay constants is

$$\frac{a\,\lambda_{\text{latt}}}{\lambda_{\text{cont}}} = 1 - \frac{\alpha_0}{d_0(1-\epsilon^2)} + \mathcal{O}\left(\frac{\alpha_0}{d_0}\right)^2 \approx 0.95. \tag{4.15}$$

Note that in equations (4.12) and (4.11) one constant multiplies lattice position, i, and the other the continuum position, x, hence the factor of a. We see that the difference between the lattice and continuum results vanishes in the infinite run length limit, $d_0/\alpha_0 \to \infty$, unless $\epsilon = 1$, in which case both decay constants

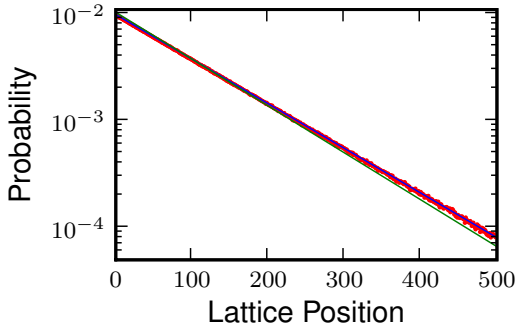

Figure 4.2: Steady state probability distribution for constant tumble rates, $\alpha_i^{\pm} = 1$ and jump rates $d_i^{\pm} = 10 \mp 1$. Simulation data are shown in red, the lattice prediction in blue and the continuum prediction in green. Data collected from 10^7 particles at $t = 2000$ on a lattice of 500 sites.

diverge.

4.2.3 Periodic Boundary Conditions

We can also calculate the expected probability distribution for periodic boundary conditions. In this case our calculation on lattice is slightly more complicated as we do not know the current a priori, but must determine it through the conditions $P(L+1,\pm) = P(1,\pm)$ and $\sum_i \big[P(i,+) + P(i,-)\big] = 1$.

We can write $P(i,+) = C_1(i)\big[P(1,+) - J\,C_2(i)\big]$, where $C_1(i)$ and $C_2(i)$ can be read from equation (4.6). Then from the periodicity of the system we can write the current as

$$J = \frac{C_1(L+1) - 1}{C_1(L+1)\,C_2(L+1)} P(1,+) \equiv C_3 P(1,+). \tag{4.16}$$

We can then use the normalisation of the distribution to determine $P(1,+)$ as

$$P(1,+) = \frac{1}{\sum_{i=1}^{L} \left[\frac{d_i^+ + d_i^- + \alpha_i^+ + \alpha_i^-}{d_i^+ + d_i^-} C_1(i)\,(1 - C_3\,C_2(i)) + \frac{C_3}{d_i^- + \alpha_i^-} \right]}. \tag{4.17}$$

As an example see figure 4.3 where we consider the case where the jump and

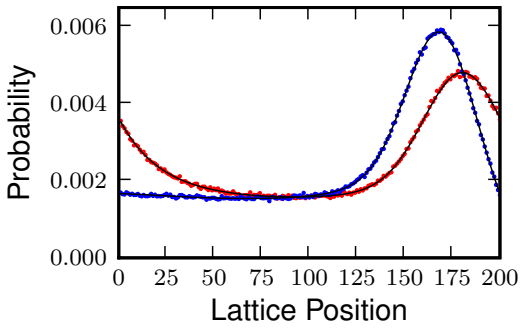

Figure 4.3: The probability distributions at steady state for rates given by equations (4.18). The distribution for left moving particles is shown in blue and for right moving particles in red. The points show data from stochastic simulations and the solid lines the theoretical prediction. Data from $2,000,000$ particles at $t = 200$ on a lattice of 200 sites.

tumble rates are

$$\begin{array}{rclcrcl} d_i^+ & = & 10 & & d_i^- & = & \frac{2}{\exp(-(x-100)^2/5000)} \\ \alpha_i^+ & = & 1 & & \alpha_i^- & = & 1. \end{array} \tag{4.18}$$

The exact forms for the probability distributions are omitted here as these do not reduce to a compact form and, though precisely calculable and consistent with simulations - as seen in figure 4.3 - are not enlightening in themselves.

To successfully capture the behaviour of the bacteria we hope to model, however, and to observe the patterning we wish to understand, non-interacting models will not suffice. We turn, in the next chapter, therefore, to the effects on interactions between our model bacteria and examine what effect they produce in the statistical properties of our system.

Chapter 5

Interacting Particles I: Saturated Condensation

Before we examine the full interacting run-and-tumble model of bacterial dynamics let us first turn to a simpler interacting system where we have just one species of particle which can hop between sites on our lattice with rates depending on the number of particles at the departure site, but not at any other site on the lattice. We shall choose the functional form of this interaction such that the hopping rate decreases with increasing particle density and observe that this leads to particles accumulating on some sites and a separation into sites of high density and others of much lower density.

It may appear on first glance that the microscopic model described in this chapter and its resulting behaviour have little to connect them to the broader narrative of this thesis in attempting to model and understand pattern formation in bacterial colonies. However, the basic manner by which the separation into high and low density sites is achieved - through a density dependent motility which amplifies stochastic fluctuations to cause particles to agglomerate - is instructive. Indeed, in chapter 6 we will investigate more general crowding type interactions, where the velocity of bacteria decreases with increasing density, and the exact results from this chapter will provide a useful guide in situations where we cannot exactly calculate the steady state. For the reader who wishes to avoid the more technical details and concentrate on the wider narrative, this chapter may be avoided without significant detriment.

5.0.4 Zero-Range Processes

The stochastic dynamical model we investigate in this chapter is known as a zero-range process (or ZRP) and has been extensively studied mathematically (see [6,59] for reviews). The model was introduced and solved for its steady-state behaviour by Spitzer [60], and it was realised a little over ten years ago that real-space condensation [61] is possible at sufficiently large particle densities under certain conditions on the hop rates [42], even within a spatially homogeneous system (see also [6,59]).

Real-space condensation, whereby a finite fraction of a system's mass accumulates within a microscopic region, is a spectacular phenomenon that is observed in a wide range of dynamical systems. For example, it is manifested experimentally in shaken granular gases in which particles can diffuse between compartments [62, 63]: as the driving strength is reduced, the sand grains cluster into a single compartment. One can also find examples in models of macroeconomics, whereby a large fraction of the available wealth is accumulated by a single individual [43], and of traffic flow, in which buses serving a single route cluster together [42].

One of the requirements for a thermodynamic condensation transition to occur as the total density of particles is increased is the absence of any restriction on the total number of particles that may occupy a single site. In this chapter, we are interested in the case where such unbounded growth of particle number is inhibited. This can happen quite naturally within specific applications: for example, the compartments in the granular gas experiments of [62, 63] are of finite size, and once they contain more than a certain number of particles, any extra particles may diffuse freely out of them. As we will show below, a vestige of the condensation phenomenon may still be observed in the form of a separation of the system into high- and low-density sites: we call this *saturated condensation*. The key questions then are: (i) Under what conditions is saturated condensation observed? (ii) How is the state of saturated condensation approached dynamically from some given initial condition?

The dynamics of condensation onto a single site has also been previously examined in the literature. There, the focus has been on the late-time coarsening of the excess mass into a decreasing number of increasingly massive clusters, which in a finite system ends with a process of mass exchange between the last

remaining clusters [64,65]. In the steady state, for a finite system, the condensate occasionally melts and reforms on a new site: the timescale of this process has been the subject of some discussion [65–67].

Variants of the ZRP where mass accumulates on multiple sites—and in particular an extensive number of sites—are comparatively little studied. Schwarzkopf et al [68] examined the statics and dynamics of a ZRP with transition rates chosen in such a way that a single condensate is destabilized in favour of either a finite number of extensive condensates, or a subextensive number of subextensive 'mesocondensates'. In both cases, one still has a finite fraction of the mass occupying a vanishingly small fraction of the sites in the thermodynamic limit, and thus a true condensation transition is observed in this model.

By contrast, I consider here the case where the hop rates in the ZRP are chosen such that the mass of condensates reaches a finite size that does not increase with system size. This prevents a true condensation transition, but nevertheless admits the possibility of saturated condensation discussed above. Since the true condensation limit can be approached by taking the upper limit on the size of a condensate to infinity, it seems clear that saturated condensation can have interesting consequences at a phenomenological level even if no formal singularity remains. This is similar to the equilibrium phenomenon of "micellization" in which attractive particles can form clusters whose size is limited by their packing geometry [69]. An analysis of this problem as an instance of saturating condensation in equilibrium was offered by Goldstein [70].

After recalling the definition of the ZRP in section 5.1 and briefly reviewing the conditions for a condensation transition in the homogeneous system (section 5.1.1), we present in section 5.1.2 the conditions on the ZRP hop rates for saturated condensation to occur. We then turn to the dynamics of the process. One can first ask about the dynamics within the steady state. This involves evaporation and formation of condensates, and in section 5.1.3 we calculate the rates at which both processes take place. The remainder of this chapter, presented in section 5.2, concerns an investigation of the relaxation to the steady state from a prescribed initial condition. My main finding is that this is a nontrivial, two-stage process. First, mass rapidly accumulates on sites that are selected by the local dynamics and in a way that depends on the initial condition. The number of such sites typically differs from its global equilibrium value. This gives rise to

a much slower second stage in which condensates are nucleated and evaporate as activated processes. We obtain a detailed portrait of both stages of the relaxational dynamics through a combination of mean-field theory, calculation of first-passage properties and an approach reminiscent of a fluctuation-dissipation analysis. In certain cases, these approximations agree remarkably well with stochastic simulations. These analytical results thus constitute a more complete account of a nonequilibrium condensation dynamics than has been achieved so far.

5.1 Presentation of the model: Steady state and condensation

The model we consider is defined on a one-dimensional lattice of L sites with periodic boundary conditions. Each site i can be occupied by an arbitrary number of particles n_i. Since the system is not connected to any reservoirs, the total number of particles in the system $N = \sum_i n_i$ is constant. A particle can move from site i to a neighbouring site $i \pm 1$ with rates $u_i^{\pm}(n_i)$, respectively (see figure 5.1). We call $d_i^{\pm}(n)$ the hopping rate *per particle* so that $u_i^{\pm}(n_i) = n_i d_i^{\pm}(n_i)$. (Note the distinction between per particle, $d(n)$, and per site, $u(n)$, rates; the per site rate can be an increasing function of n even while the per particle rate decreases, for example.) Qualitatively, our main results hold for both symmetric and asymmetric hoping rates but to avoid redundancies we shall only present the symmetric case. The definition of the zero-range process (ZRP) is that the hopping rates depend only on the number of particles at the *departure* site and not, for instance, on the occupancy of the target site. In general the rates could also vary from site to site but in this work we consider only spatially homogeneous systems.

5.1.1 Factorisation and condensation

Although the ZRP has been extensively reviewed in the literature [6, 59] we shall briefly summarise some known results that will be important in our understanding of saturated condensation, deferring to these articles for further details. First, because the interactions between particles are limited to a single site, the steady-

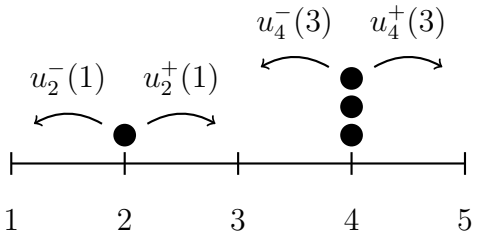

Figure 5.1: Presentation of the model. The arrows indicate the allowed transitions and the rates at which they occur.

state distribution of occupancies factorises. That is, in the canonical ensemble one has [6]

$$P(\{n_i\}) = \frac{1}{Z_{N,L}} \prod_{i=1}^{L} g(n_i)\, \delta\Big(\sum_{j=1}^{L} n_j - N\Big) \tag{5.1}$$

where the partition function $Z_{N,L}$ is given by

$$Z_{N,L} = \sum_{\{n_i\}} \prod_{i=1}^{L} g(n_i)\; \delta\Big(\sum_{i=1}^{L} n_i - N\Big) \tag{5.2}$$

and the factors $g(n_i)$ are determined by the hopping rates

$$g(n) = \prod_{j=1}^{n} \frac{1}{u(j)} \quad \text{for} \quad n > 0 \quad \text{and} \quad g(0) = 1\ . \tag{5.3}$$

The delta functions in (5.1) and (5.2) simply enforce the constraint that the total number of particles on the lattice is fixed. The marginal probability that a given site has n particles is given by

$$p_i(n) = g(n) \frac{Z_{L-1,N-n}}{Z_{L,N}}\ . \tag{5.4}$$

As previously mentioned, the ZRP admits an interesting condensation transition. Although it can be worked out directly from the canonical ensemble [71], the condition for condensation is most easily seen in the grand canonical ensemble. Introducing a chemical potential μ and the single-site partition function $\mathcal{Z}_1(\mu)$,

the partition function for the L-site system reads

$$\mathcal{Z}_L(\mu) = \sum_N \exp(\mu\, N) Z_{L,N} = \left[\sum_n \mathrm{e}^{\mu\, n - \sum_{j=1}^{n} \ln[u(j)]}\right]^L \equiv [\mathcal{Z}_1(\mu)]^L \tag{5.5}$$

Note that the only correlations between different sites in the canonical ensemble come from the constraint on the total number of particles in (5.1). Since this constraint has been removed in favour of a chemical potential, the sites are now completely uncorrelated in the steady state and the L-site partition function reduces to a single-site problem. To get more insight into $\mathcal{Z}_1$, one can rewrite the hopping rate per particle as $d(j) = d_0\, \mathrm{e}^{h(j)}$, where d_0 is the hopping rate of a single particle and $\mathrm{e}^{h(j)}$ encodes the interaction between the particles. For instance, $h(j) = 0$ for all j corresponds to non-interacting particles. The partition function then reads

$$\mathcal{Z}_1(\mu) = \sum_n \exp[-F(n,\mu)] \tag{5.6}$$

where $F(n,\mu) = f(n) - \mu\, n$ and we have introduced

$$f(n) = \ln(d_0)\, n + \ln(n!) + \sum_{j=1}^{n} h(j)\ . \tag{5.7}$$

The marginal probability that a single site has n particles is then given by

$$\begin{aligned} p(n|\mu) &= \mathrm{e}^{\mu\, n} g(n) \frac{\mathcal{Z}_{L-1}(\mu)}{\mathcal{Z}_L(\mu)} \\ &= \frac{1}{\mathcal{Z}_1(\mu)} \exp[\mu n - f(n)] \end{aligned} \tag{5.8}$$

and the average number of particles per site by [6]

$$\langle n \rangle \equiv \rho = \frac{\mathcal{Z}_1'(\mu)}{\mathcal{Z}_1(\mu)}\ . \tag{5.9}$$

We thus see from (5.8) that $f(n)$ plays the role of a single-site free energy, and hence that $F(n,\mu)$ is a single-site grand canonical potential.

The general idea of ensemble equivalence is to ask what chemical potential μ should be imposed to get a given value of $\langle n \rangle$. To detect a possible condensation transition, one thus looks for the maximum density ρ_c for which equation (5.9)

has a solution. If this maximum is infinite, then (5.9) is always solvable and there is no transition. If, however, ρ_c is finite then equation (5.9) cannot be solved for a density greater than ρ_c and the excess mass condenses on a single site, which can thus carry a finite fraction of the total mass of the system. The breaking of ensemble equivalence between canonical and grand canonical ensemble is a signature of the condensation transition.

The condition for (5.9) to have a solution has been worked out and yields a criterion on the form of $u(n)$ to observe condensation. It can be summarised as follows [6]:

- if $u(n)$ decays to a non-zero constant more slowly than $u(n) \simeq \beta(1 + 2/n)$, one observes above a non-zero critical density the appearance of a single condensate in a background fluid which remains at the critical density.
- if $u(n) \to 0$ as $n \to \infty$, condensation occurs at all densities and the fraction of particles in the fluid phase tends to zero.
- otherwise, and in particular if $u(n)$ increases as $n \to \infty$, condensation does not occur.

The first two cases, in which there exists a true thermodynamic phase transition, have previously received much attention in the literature (as reviewed by Evans and Hanney [6]). What we shall show in the following is that the third case also may also exhibit interesting condensation-like features, despite the absence of a true condensation transition, where the stationary state supports a coexistence of sites at two characteristic densities. This is the case we refer to as *saturated condensation*.

5.1.2 Criteria for saturated condensation

As mentioned in the introduction to this chapter, it is natural to expect condensation in real space to saturate at some large but finite value for the mass of the condensate (e.g., in shaken granular gases when the finite size of the compartments prevents true condensation). We will therefore consider systems where the hop rate per particle $d(n)$ asymptotically decreases to a finite but non-zero value. Even if the total hop rate per site, $u(n)$, initially decreases with n, it eventually starts increasing again and there is no phase transition, as discussed

above. However, we will show that the initial decrease in $d(n)$ may suffice to destabilise a homogeneous state, whereas the asymptotic growth of $u(n)$ prevents the formation of condensates with a mass that diverges with the system size. One thus ends up with a steady-state containing an extensive number of finite-sized condensates. Since there is no thermodynamic transition, canonical and grand canonical ensembles remain equivalent. Therefore, we can perform our analysis solely within the latter ensemble, and dispense with the cumbersome constraint on the total number of particles. On the other hand, simulations are most straightforwardly conducted in the canonical ensemble. Since we shall use both ensembles in the following, we will refer equivalently to free energy or grand potential with the understood assumption that chemical potential μ and number of particles N are adjusted so that $\sum_n n\, p(n|\mu) = N$.

For the system to start forming condensates (in a sense to be defined more formally below) one needs the single site free energy $f(n)$ to be non-convex, that is $f''(n) < 0$ for some range of n. Flat profiles with such occupancies would then be unstable under the dynamics and undergo spinodal decomposition. Treating n as a continuous variable, we have $f(n) \simeq \int_1^n \ln u(n')\mathrm{d}n'$, and hence the second derivative with respect to n is given by

$$f''(n) \simeq \frac{u'(n)}{u(n)} \tag{5.10}$$

which implies spinodal decomposition for occupancies such that $u'(n) < 0$. This is exactly equivalent to the condition [4] that the hop rate per particle, $d(n) = u(n)/n$, should satisfy the equation

$$d'(n) < \frac{d(n)}{n}\ . \tag{5.11}$$

Such an instability could in principle lead to complete condensation: the criterion (5.11) is indeed satisfied when the condensation transition occurs. This is because the phase separation can lead to phase coexistence between a low-density phase and a high-density phase whose density can diverge with system size, i.e., a macroscopic condensate. This is, for instance, what was found by Schwarzkopf et al. [68], when the jump rates $u(n)$ depend on the system size L in such a way that the mass of each of the multiple condensates diverges in the thermodynamic limit. For the high density sites to have *finite* occupancies, we will further require

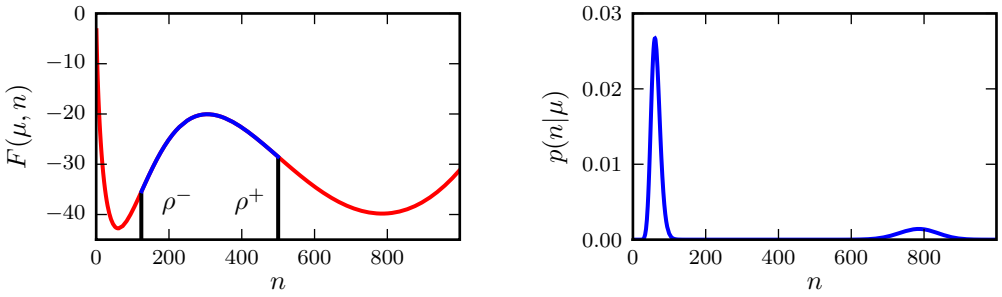

Figure 5.2: **Left:** The grand potential density per site, $F(\mu, n)$, for the choice $u(n) = d_0\, n\, \exp(-\lambda\phi \arctan(n/\phi))$ discussed in the text, with $d_0 = 2.5$, $\lambda = 0.01$, $\phi = 250$ and $\langle n \rangle = 100$. The region unstable to spinodal decomposition is in blue: it corresponds to the concave part of the grand potential. **Right:** The resulting, normalised, probability distribution.

that $f'(n) \to \infty$ when $n \to \infty$; if $fn \to \infty$ but $f'(n)$ remains finite the double tangent construction will be between a finite low density and an infinite high density. Combined with the fact $f(n)$ is not everywhere convex this implies that the free energy per site has a double tangent between two finite densities [72]. Under these conditions the grand canonical potential per site, $F(n, \mu)$, forms a double well whose minima occur for finite values of n and give the typical occupancy of the high- and low-density sites. 'Saturated condensation' now is to be understood as referring to this scenario. In terms of the microscopic jump rates, the requirement that $f'(n) \to \infty$ is equivalent to $u(n) \to \infty$ as $n \to \infty$, so $u(n)$ must be an unbounded increasing function of n or, correspondingly, $d(n)$ must either increase as $n \to \infty$, or decrease more slowly than $1/n$.

Let us illustrate this with a concrete example of a function $u(n)$ that leads to saturated condensation, and which we will use repeatedly throughout the remainder of this work, it reads

$$u(n) = d_0\, n\, \exp[-\lambda\phi \arctan(n/\phi)]\ . \tag{5.12}$$

Though this functional form may at first look rather unusual, we choose it here as a convenient example of a function which rapidly decays towards a non-zero constant value. With this definition, the hop rate per particle $d(n)$ initially decreases exponentially with n before it saturates at a constant value $d_0 \exp(-\lambda\phi\pi/2)$. A flat profile is unstable if $u'(n) < 0$, that is if $\lambda\phi > 2$ and

$n \in [\rho^-, \rho^+]$ where

$$\rho^{\pm} = \frac{\lambda\phi^2 \pm \phi\sqrt{\lambda^2\phi^2 - 4}}{2}. \tag{5.13}$$

As $n \to \infty$, $u(n) \sim d_0 n \exp(-\lambda\phi\pi/2)$ and is thus increasing linearly with n; the condensates have finite size. This choice of rates gives rise to the double-well free energy and bimodal probability distribution shown in fig. 5.2.

Note that the range $[\rho^-, \rho^+]$ corresponds to the concave part of the free energy, as expected from standard thermodynamics [73]. As long as the average density lies between the two minima of $F(\mu, n)$, the steady state will be dominated by configurations with condensates. Flat profiles will however be metastable outside $[\rho^-, \rho^+]$, thus requiring activated events to lead to condensation. Simulations of the systems for rates obeying (5.12) show the predicted behaviour. On the left panel of figure 5.3 one sees the results of simulations started with N particles distributed randomly over the L sites. The average density $\rho = N/L$ is chosen either within or outside the condensation regime. The criteria for the condensate to have finite mass can be checked by considering the family of rates defined by

$$d_\alpha(n) = d_0\, n^{-\alpha} \exp[-\lambda\phi \arctan(n/\phi)] \tag{5.14}$$

One indeed sees that the minimum in the grand potential corresponding to the high-density phase is at a finite value of n for $\alpha < 1$ and diverges when $\alpha \to 1$ (see right panel of figure 5.3).

5.1.3 Condensation and evaporation dynamics in the steady state

When the average density lies between the two minima of the grand potential, there is a coexistence of high- and low-density sites in steady-state. Since the grand potential barrier between them is finite (see figure 5.2), the instantaneous number of condensates will fluctuate as low-density sites condense and high-density sites evaporate. To discuss these processes in more detail, it is helpful to formally define a condensate (or high-density site) as a site with a density greater than the one at the peak in the grand potential between the two minima. Likewise, when the density on a site lies below the value corresponding to this peak, we refer to it as a low-density site. With this definition, the average densities

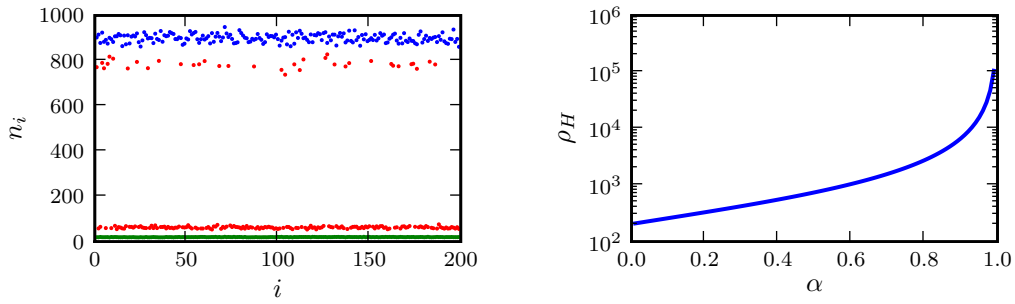

Figure 5.3: **Left**: Steady-states of stochastic simulations for $\phi = 250$, $\lambda = 0.01$, $d_0 = 2.5$. For these parameters, the minima in the grand potential correspond to $\rho_L \approx 60$ and $\rho_H \approx 800$. Occupancies are averaged over a time window $t \in [5000; 15000]$. Green and blue symbols correspond to initial average densities ($\rho = 20$ and $\rho = 900$ respectively) that are either below ρ_L or above ρ_H and are as expected stable. For an initial density $\rho = 300$ between ρ_L and ρ_H (red symbols), steady-state configurations typically exhibits a low density background at $\rho = \rho_L$ and high density condensates at $\rho = \rho_H$. **Right**: Semi-log plot of the typical mass of the high density phase for different value of α, using the rates (5.14). One sees that when $\alpha \to 1$, the mass of the condensate diverges as expected.

of the high- and low-density sites in the steady state are

$$\rho_L = \frac{\sum_{n=0}^{n_{\rm peak}} n\, p(n|\mu)}{\sum_{n=0}^{n_{\rm peak}} p(n|\mu)} \qquad \text{and} \qquad \rho_H = \frac{\sum_{n=n_{\rm peak}}^{\infty} n\, p(n|\mu)}{\sum_{n=n_{\rm peak}}^{\infty} p(n|\mu)} \tag{5.15}$$

while the average number of condensates in steady state is given by

$$n_c^{\rm eq} = L \sum_{n=n_{\rm peak}}^{\infty} p(n|\mu) = L\, \frac{\rho - \rho_L}{\rho_H - \rho_L}\ . \tag{5.16}$$

We may then also define the rate of evaporation of the condensates, $\mathcal{R}_{\rm evap}$, and condensation of the low-density sites, $\mathcal{R}_{\rm cond}$. At equilibrium these balance in such a way that the number and size of the condensates remain constant on average: $\mathcal{R}_{\rm evap}\, n_c^{\rm eq} = (L - n_c^{\rm eq})\, \mathcal{R}_{\rm cond}$.

Although formation and evaporation of a condensate require many hops and are thus complicated processes, the corresponding rates can be computed following a first-passage time approach [74]. Indeed if we know the first passage time $T_{n,n_{\rm peak}}$ from a high density site $n \simeq \rho_H$ to $n = n_{\rm peak}$, we can approximate

the evaporation rate for a site with n particles by

$$\mathcal{R}_{\rm evap}(n) = \frac{1}{2\,T_{n,n_{\rm peak}}}\ , \tag{5.17}$$

where the factor of a half arises as a site at the peak can fall in either direction with equal probability. To calculate the evaporation and condensation rates in the steady state, we must therefore calculate the relevant first-passage times for diffusion in a double well. To achieve this we follow previous approaches applied to ZRPs undergoing a thermodynamic condensation transition [67, 75].

We illustrate this procedure by computing the first-passage time to an evaporation event. We thus consider a high-density site with $n > n_{\rm peak}$ particles. The rates at which the occupancy decreases or increases are given by

$$\begin{aligned} &W(n \to n-1) = u(n) = 2\,d_0\,n\,e^{-\lambda\,\phi\,\arctan\left(\frac{n}{\phi}\right)} \\ &W(n \to n+1) \equiv u_L\ . \end{aligned} \tag{5.18}$$

In principle, the rate at which particles are added on top of a condensate depends on the neighbouring densities. We will however assume their fluctuations to be small and consider u_L to be constant. The first-passage time from n particles to $n_{\rm peak}$ is denoted $T_{n,n_{\rm peak}}$ and, in continuous time, is the solution to the equation

$$\begin{aligned} T_{n,n_{\rm peak}} \;=\; & {\rm d}t + [\,1 - (u_L + u(n))\ {\rm d}t\,]\,T_{n,n_{\rm peak}} \\ & + u(n)\,{\rm d}t\,T_{n-1,n_{\rm peak}} + u_L\,{\rm d}t\,T_{n+1,n_{\rm peak}} \end{aligned} \tag{5.19}$$

Lengthy but standard algebra (see Appendix B) leads to

$$T_{n,n_{\rm peak}} = \sum_{l=n_{\rm peak}+1}^{n} \frac{1}{u(l)\,p(l|\mu)} \sum_{m=l}^{\infty} p(m|\mu)\ . \tag{5.20}$$

Similarly one finds for the first passage time for condensation

$$T'_{n,n_{\rm peak}} = \sum_{i=n+1}^{n_{\rm peak}} \frac{1}{u_H\,p(i|\mu)} \sum_{j=0}^{i-1} p(j|\mu)\ . \tag{5.21}$$

Note that to determine more accurately the rates of evaporation and condensation we should in principle average over all starting positions above and

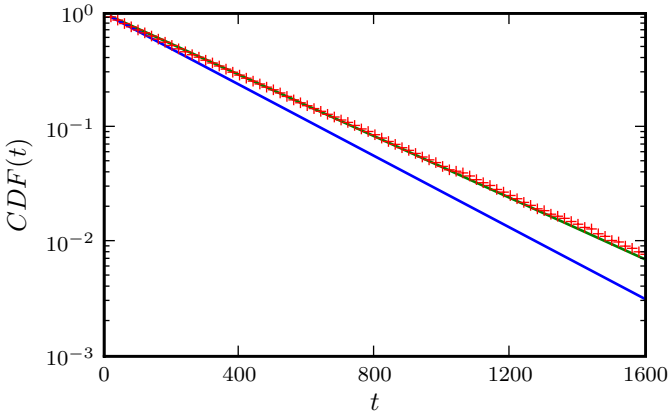

Figure 5.4: Semi-log plot of the cumulative distribution function of evaporation or condensation events in steady state for $\phi = 50$, $\lambda = 2.8/50$, $d_0 = 2.5$, $\langle n \rangle = 100$. The blue line corresponds to the cumulative distribution function of a Poisson distribution, $CDF(t) = \exp(-\gamma\, t)$ with $\gamma \approx 0.0036$ as predicted by equation (5.22). The red dots stem from 10000 simulations and can be fitted with a rate $\gamma \approx 0.0031$ (green line).

below the barrier, respectively:

$$T_{\text{evap}} = \frac{\sum_{n=n_{\text{peak}}}^{\infty} p(n|\mu)\, T_{n,n_{\text{peak}}}}{\sum_{n=n_{\text{peak}}}^{\infty} p(n|\mu)} \quad \text{and} \quad T_{\text{cond}} = \frac{\sum_{n=0}^{n_{\text{peak}}} p(n|\mu)\, T'_{n\, n_{\text{peak}}}}{\sum_{n=0}^{n_{\text{peak}}} p(n|\mu)} \,. \tag{5.22}$$

We can then define the escape rate from a configuration as the rate for either an evaporation or condensation to occur:

$$\mathcal{R}_{\text{total}} = \frac{n_c}{2\, T_{\text{evap}}} + \frac{L - n_c}{2\, T_{\text{cond}}} \,, \tag{5.23}$$

where n_c is the number of condensates. In this picture, the distribution of times between events, either evaporations or condensations, for a system of length L will be Poissonian with rate $\mathcal{R}_{\text{total}}$. For a given choice of parameters, $\phi = 50$, $\lambda = 2.8$, $d_0 = 2.5$, $L = 5000$ and $\langle n \rangle = 100$, for example, equation (5.23) can be evaluated numerically. First we compute μ so that $\langle n \rangle = 100$ by solving (5.9). We can then use expression (5.8) for $p(n|\mu)$ to compute T_{evap} and T_{cond} from (5.20), (5.21) and (5.22). We last obtain from (5.23) that the total rate is $\mathcal{R}_{\text{total}} \approx 0.0036$. To compare this theoretical prediction with numerics we compute the cumulative distribution function of evaporation and condensation events from

10000 runs: $F_{CD}(t)$ is the probability that the first evaporation or condensation occurs after time t. The simulation data are shown in fig. 5.4; as predicted by the theory the distribution is Poissonian and a fit to the simulation data gives $\mathcal{R}_{\text{total}} \approx 0.0031$, which is within $\sim 15\%$ of the predicted value. It may be inferred that the discrepancy between these two figures results from the approximations made in the first passage time calculation, namely that the neighbouring sites to a condensation or evaporation event remain at a constant density throughout.

5.2 Two-stage dynamics of condensate formation

We now examine the relaxation of the system to its steady-state, which is a nontrivial process. Starting from a homogeneous configuration within the unstable region ($n \in [\rho^-, \rho^+]$, see figure 5.2), the dynamics divides naturally into two regimes presented in figure 5.5. At early times in the dynamics, an instability, due to stochastic fluctuations, forms in the flat profile. This instability seeds a number (n_c) of condensates which then grow rapidly. At the end of this growth stage, n_c is in general not equal to the equilibrium number n_c^{eq} and the system has not yet reached stationarity. A second stage then follows, taking place on much longer timescales, during which activated events responsible for condensation and evaporation of condensates lead the system towards its ultimate steady state. This difference in relevant timescales between the two stages can be seen from figure 5.5. Our aim in this section is to understand these two distinct relaxational regimes.

Simulations of the stochastic system, started from random deposition of N particles over the L sites of the lattice with $N/L \in [\rho^-, \rho^+]$, show that the positions of the condensates are, initially, anti-correlated (see figure 5.6). Transient anti-correlations of this type are a general feature of systems obeying a conservation law, see, for example, Cornell et al. [76]. This can be understood as a consequence of the condensates being created through depletion of the neighbouring sites, thereby preventing the formation of other condensates in their immediate surroundings: if there is a condensate at site i, there is a decrease in the probability to find another condensate in its vicinity. These correlations survive until the late-stage dynamics when new condensates are formed and old

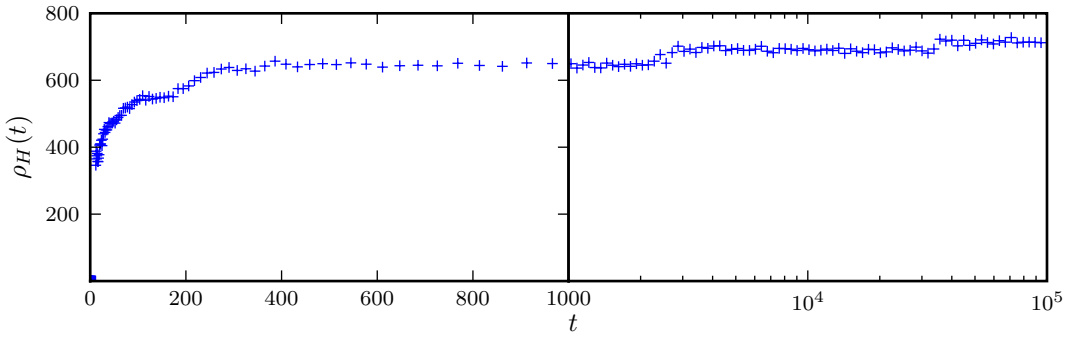

Figure 5.5: Average density in the high density sites as a function of time for parameters $\phi = 250$, $\lambda = 0.01$, $d_0 = 2.5$. The early dynamics ($t \sim 0 - 1000$) see the rapid formation of n_c condensates that are rapidly growing. The late stage dynamics $t \sim 10^3 - 10^5$ correspond to formation and evaporation of condensates that leads n_c to $n_c^{\rm eq}$ and the average mass of the condensates to its equilibrium value. Steps in the average density correspond to the evaporation of a condensate that is redistributed on the surviving ones. (Note the switch from linear to logarithmic scale on the time axis at $t = 1000$.)

condensates evaporate, thus smoothing out the correlations [1]. Note that if we started with the correct number of *regularly-spaced* condensates at the correct steady-state density (which would be a highly correlated initial condition) the correlations would be smoothed out on exactly the same timescales: correlations are mainly due to the immobility of the condensates, which only get randomised (by evaporation/condensation) in the late stage of the dynamics. Also, if one starts with a global density within $[\rho_L, \rho_H]$ but well outside $[\rho^-, \rho^+]$, there is no initial instability since the flat profile is metastable and the first stage is thus absent: the creation of condensates is then only due to activated events. We now turn to a more detailed analysis of both stages.

5.2.1 Initial instability and growth stage

The early stage dynamics corresponds to the rapid growth of an instability around the flat profile which leads to the formation of some number of condensates n_c. These condensates then rapidly grow and saturate at a density that generically differs from that at the minimum of the high density well in the free energy. Insight into this part of the dynamics can be gained by comparing the stochastic dynamics of the system with its deterministic mean-field limit. The latter is

[1] As the model is factorisable there can be no correlations in the true steady-state.

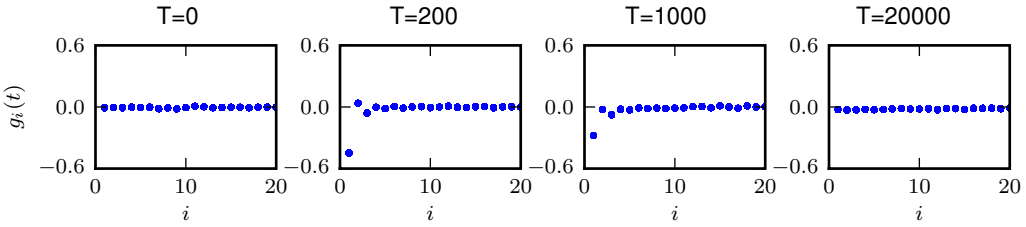

Figure 5.6: Snapshots of the correlation function $g_i(t) = \langle n_{j+i}(t) n_j(t) \rangle_c \,/\, \langle n_j^2(t) \rangle_c$, where $\langle x^2 \rangle_c \equiv \langle x^2 \rangle - \langle x \rangle^2$ and the averages are taken both over the lattice site j and many simulations. Starting from an initially flat profile, an anti-correlation between sites forms as the condensates condense which then gradually disappears at late times when subsequent evaporations and condensations randomise the positions of the condensates. The parameters of the simulation are $d_0 = 2.5$, $\Phi = 50$, $\lambda = .05$ and $\langle n \rangle = 80$.

obtained by replacing $\langle u(n_i) \rangle$ by $u(\langle n_i \rangle) = u(\rho_i)$; it reads

$$\dot{\rho}_i = u(\rho_{i-1}) + u(\rho_{i+1}) - 2\,u(\rho_i)\ . \tag{5.24}$$

and can be integrated numerically using, for example, a simple Euler scheme. Starting from an initial condition obtained by distributing at random N particles among the L sites of the lattice, we see in figure 5.7 that stochastic and mean-field dynamics agree very well, despite the fact that the mean-field approximation (by definition) neglects both noise and correlations. We infer from this that activated events and spatial correlations are not very important to understand the early-stage dynamics and we shall thus proceed using this more analytically-tractable mean-field framework.

At early times, the number of condensates that are created depends strongly on the initial condition. For instance, starting the mean-field simulation from a flat profile superposed by a cosine wave leads to the creation of a condensate from each peak of the cosine wave, as shown in the left panel of figure 5.8. We shall first focus on the case where the number of condensates is thus controlled. As time goes on, the mass for the condensates is drawn from neighbouring sites, which suggests a model of this particular condensate-formation process as one in which sites have one of two time-dependent densities. Specifically each high-density site has a density $\rho_H(t)$, and is surrounded by a pair of low-density sites, both with density $\rho_L(t)$.

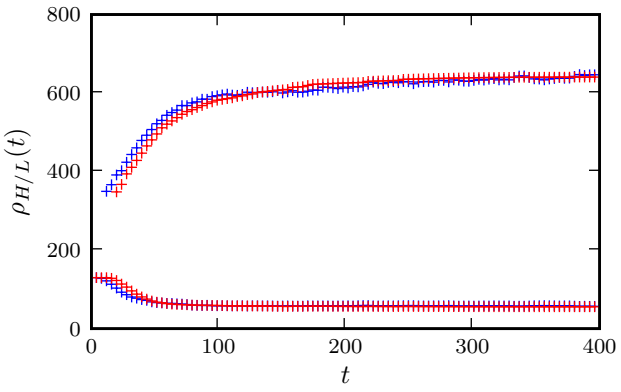

Figure 5.7: The evolution of the average high and low densities: using numerical simulations in the deterministic (red) and stochastic (blue) cases. Both simulations were run with random (Poissonian) initial conditions and with the parameters $\phi = 250$, $\lambda = 0.01$, $d_0 = 2.5$ and $\langle n \rangle = 130$. Although the agreement is not exact the qualitative behaviour is certainly similar. The slight lag between the stochastic and deterministic cases is due to activated events increasing the initial separation between high and low density sites and is not especially relevant to an understanding of the dynamics.

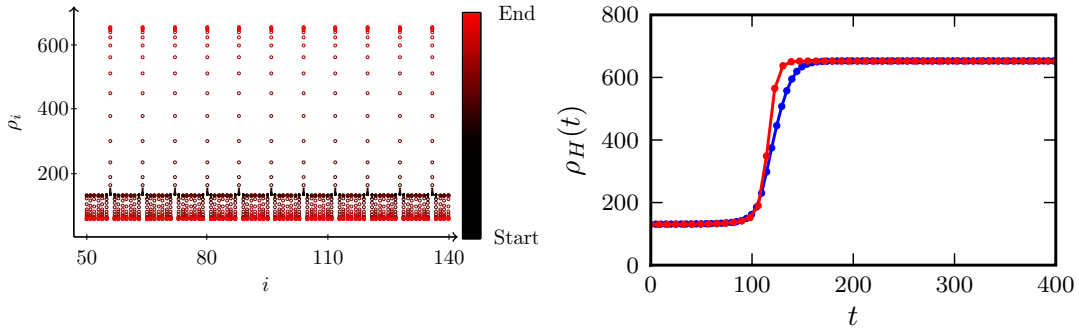

Figure 5.8: **Left**: Starting from an initial profile which is flat plus a cosine perturbation condensates grow at every peak (n_c is 35% higher than n_c^{eq}). Increasing time is represented by a change in colour. Parameters are $\lambda = 0.01$, $\phi = 250$, $d_0 = 2.5$ and $\langle n \rangle = 130$. **Right**: The mean-field stochastic simulations (red), as left, and the solutions to equations (5.25) (blue). The approximation to consider just two densities gives a sharper change but the end points are in excellent agreement.

Within this simplification, the mean-field equations (5.24) reduce to

$$\dot{\rho}_H = 2\,[u(\rho_L) - u(\rho_H)]\,; \qquad \dot{\rho}_L = p_{\ell c}\,[u(\rho_H) - u(\rho_L)] \tag{5.25}$$

where we used the fact that condensates have two low density neighbours whereas low density sites have a probability

$$p_{\ell c} = \frac{2\,n_c}{L - n_c} \tag{5.26}$$

of being next to a condensate. This simple approximation reproduces surprisingly well the mean-field dynamics for this particular initial condition, as can be seen from the right panel of figure 5.8. Inspection of equation (5.25) then gives a simple picture of what is happening: in the spinodal region $u'(n) < 0$, so that $u(\rho_L) - u(\rho_H) > 0$ and $\dot{\rho}_H$ is positive whereas $\dot{\rho}_L$ is negative. Consequently the high density will increase and the low density decrease. This continues as long as $u(\rho_H) < u(\rho_L)$ but stops at the first moment when $u(\rho_H) = u(\rho_L)$. This is indeed what happens during the simulation, as can be seen on figure 5.9.

Note that according to the previous discussion, the average values of ρ_L and ρ_H at the end of the growth stage can be deduced from the initial number of condensates, using conservation of mass and requiring that $u(\rho_H) = u(\rho_L)$ (see equation (5.25))

$$n_c\,\rho_H + (L - n_c)\rho_L = N\,; \qquad u(\rho_H) = u(\rho_L)\,. \tag{5.27}$$

That is, we require the flux from high to low to match that from low to high and that the total number of particles, N, is the sum of the number in a high density state, $n_c\rho_H$, and the number in a low density state, $(L - n_c)\rho_L$. Starting simulations with different wavelength for the initial cosine perturbation indeed leads to density ρ_H and ρ_L predicted by (5.27) where n_c equals the number of peaks of the cosine wave.

For more general initial conditions or in the stochastic case, we have not been able to find a simple way to predict the number of condensates to be formed. The saturation of their growth once formed however follows the same rules as above, leading to high and low densities that in general differ from the steady-state ones (see figure 5.9). Further changes in the average densities are due to activated

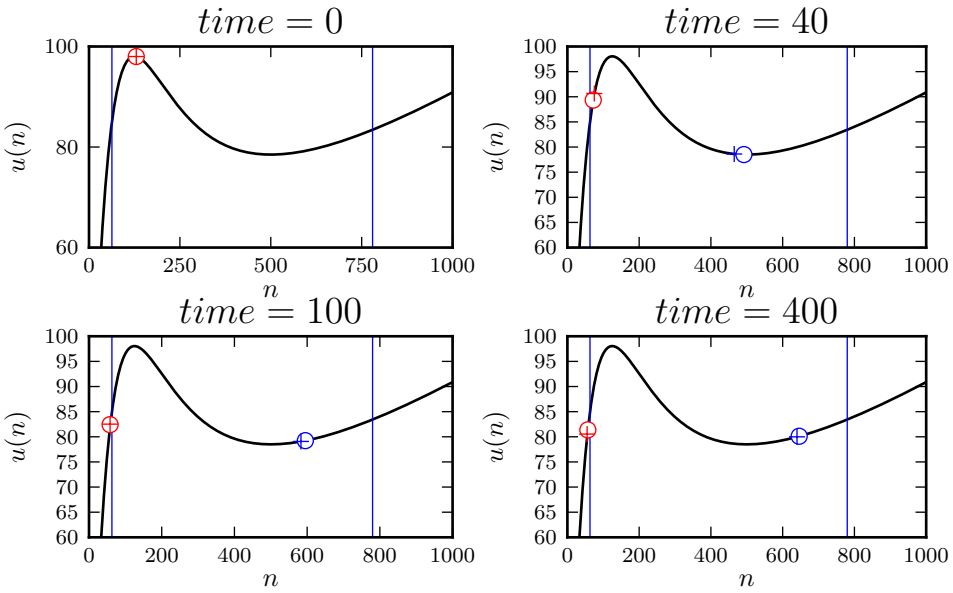

Figure 5.9: Snapshots of the hopping rate out of a site with n particles, $u(n) = d_0\, n \exp(-\lambda\phi \arctan(n/\phi))$, for mean-field simulations (crosses) and stochastic ones (circles). The red and blue symbols represents the average high density and low density sites. The blue lines show the steady state values of ρ_H and ρ_L and the black line the function $u(n)$. At $time = 400$, $u(\rho_H) = u(\rho_L)$ and the condensate thus stop increasing. One must then wait for activated events in the stochastic simulations to get closer to the equilibrium values. The difference between stochastic and mean-field predictions comes from the different number of condensates that results from the initial instability.

events which change the number of condensates and increase both ρ_L and ρ_H. These events are not captured by the mean-field approximation, and require a distinct analysis that is discussed in the next section.

5.2.2 Activated events and late-stage dynamics

To understand the late stage dynamics, which is mediated by stochastic nucleation and evaporation of condensates, we must investigate the activated crossing between the two wells in the grand-potential landscape shown in figure 5.2.

We have observed that during the late-stage relaxation, the total mass in the high-density sites remains approximately constant, despite the fact that the number of such sites changes over time. Thus, the average density per condensate increases in the step-wise fashion depicted in figure 5.10. When a

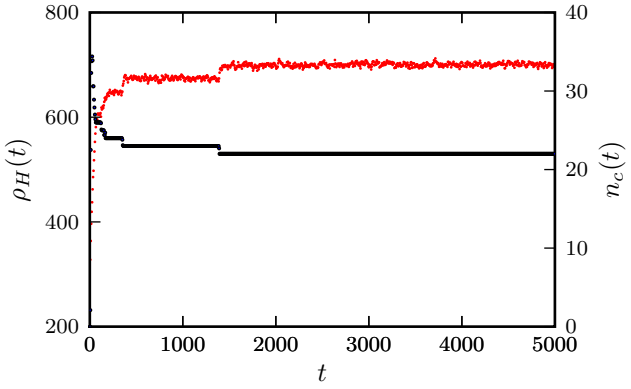

Figure 5.10: Typical evolution of the average density and number of condensate sites. Each steps correspond to the evaporation of a condensate that is redistributed over the other high density sites. The parameters of the simulations are $\lambda = 0.01$, $\phi = 250$ and $d_0 = 2.5$

condensate evaporates the excess density on that site is redistributed over the other high-density sites, thereby increasing their average density; conversely, when a new condensate forms, the average density decreases. Depending on whether the late stage starts with too many or too few condensates, evaporation or condensation will first dominate, before the two rates become closer and closer. Once evaporation and condensation of new condensates balance, the steady state described in section 5.1.3 is reached.

In the steady state, the rates of evaporation and condensation can be treated as a first passage problem in a grand potential landscape—as shown previously in section 5.1.3. Away from steady state, however, the rates are different from the equilibrium ones and depend in general on the dynamics. Numerically, we can measure the rates as a function of the fraction of condensates by recording how long the system spends in a given configuration with n_c condensates and averaging over many runs. We now show that these *nonequilibrium* rates can also be calculated by appealing to a fluctuation- dissipation-type argument and adapting the equilibrium formalism correspondingly. The key to this approach is to assume that when the number of condensates n_c is sufficiently close to its equilibrium value n_c^{eq}, the difference $n_c - n_c^{\mathrm{eq}}$ could be due either to a spontaneous fluctuation (which we are observing) or *equivalently* to the application of a small field. To this end, we introduce a new 'doubly-grand canonical' ensemble that involves an additional chemical potential μ' conjugate to the number of condensates n_c. The

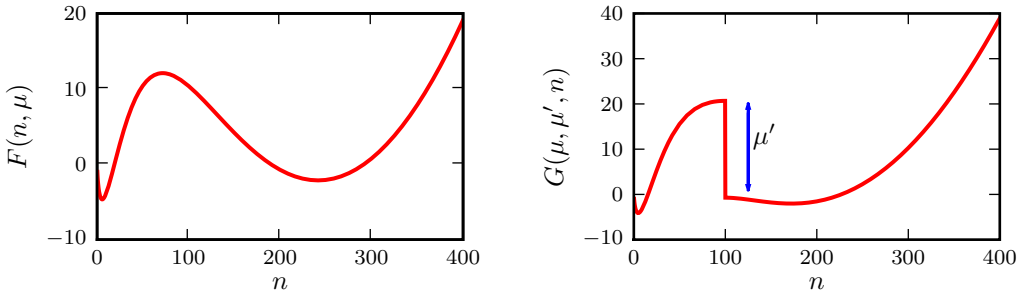

Figure 5.11: **Left**: the free energy per site for d_0=2.5, $\phi = 50$, $\lambda = 3/50$, $\langle n \rangle = 100$ at steady state, where there are 40% of condensate sites. **Right**: the free energy for the same microscopic rates and average occupancy but constrained to have 60% of condensate sites.

corresponding partition function is then given by

$$\Xi = \sum_{N=0}^{\infty} \sum_{n_c=0}^{L} \mathrm{e}^{\mu N} \mathrm{e}^{\mu' n_c} Z_{L,N} \ . \tag{5.28}$$

Defining a condensate, as before, as any site containing more than n_{peak} particles, the partition function can be re-written as

$$\Xi = \sum_{n_c=0}^{L} \mathrm{e}^{\mu' n_c} \left[\sum_{n=0}^{\infty} \mathrm{e}^{-f(n)+\mu n} \right]^L = \sum_{n_c=0}^{L} \left[\sum_{n=0}^{\infty} \exp[-G(\mu,\mu',n)] \right]^L \ . \tag{5.29}$$

where we have introduce a new thermodynamic potential

$$G(\mu,\mu',n) = f(n) - \mu\, n - \mu'\, \theta(n - n_{\mathrm{peak}}) \tag{5.30}$$

$G(\mu,\mu',n)$ can simply be obtained by introducing a step $-\mu'$ in the grand potential $F(\mu,n)$, see fig. 5.11. The new marginal probability to observe an occupancy n is then given by

$$p(n|\mu,\mu') = \frac{\mathrm{e}^{-G(\mu,\mu',n)}}{\Xi_1(\mu,\mu')}; \quad \text{where} \quad \Xi_1(\mu,\mu') = \sum_{n=0}^{\infty} \mathrm{e}^{-G(\mu,\mu',n)} \tag{5.31}$$

To evaluate the rates of evaporation and condensation of the system in the presence of n_c condensates, one can thus compute numerically the values of μ

and μ' such that

$$\sum_n n\, p(n|\mu,\mu') = N \quad \text{and} \quad \sum_n \theta(n - n_{\text{peak}})\, p(n|\mu,\mu') = n_c \tag{5.32}$$

We can then compute the rate of evaporation or condensation from a configuration with N particles and n_c condensates exactly as in section 5.1.3 where $F(\mu, n)$ is now replaced by $G(\mu, \mu', n)$ (with the additional constraint that the equalities in equation (5.32) must be solved simultaneously to derive μ and μ'). To compare the results of these calculations with numerics we started 100 runs from $n_c = 275$ and 100 from $n_c = 155$. While these runs relaxed to the equilibrium value $n_c = 199$ we recorded the average time spent, $\tau(n_c)$, by the system for each intermediate value of n_c and approximated $\mathcal{R}_{\text{total}}(n_c) = 1/\tau(n_c)$. The results of these simulations are compared with the theoretical predictions in figure 5.12. The fact that the agreement between theory and numerics is not as good as in section 5.1.3 may be due to the fact that we have poorer statistics (100 runs against 10000).

Another plausible explanation for this inconsistency is the assumption that the neighbouring sites will have a constant density throughout the evaporation or condensation process. In fact the neighbouring sites are likely to have higher densities than otherwise during an evaporation and lower densities during a condensation. As both high and low density sites sit in regions where $u'(n) > 0$, an increase in density will increase the rate at which particles enter the evaporating site whilst a decrease in neighbouring density will decrease the rate at which particles enter a condensing site. Both these processes will have the effect of increasing the average duration of a condensation or evaporation event, and reducing the rates at which they happen. Hence the calculated evaporation and condensation rates would be larger than the real rates as measured.

Nevertheless, we find that this 'doubly- grand canonical' construction provides remarkably good estimates for the evaporation and condensation rates: even where they are two orders of magnitude larger than in equilibrium, theory and simulations are still within a factor 2 of each other.

In this chapter we have identified a *saturated condensation* scenario that may occur within the zero-range process (ZRP). The steady state is characterized by an extensive number of finite-sized condensates, as opposed to a single macroscopic condensate that has previously been the focus of attention. Such a state may be

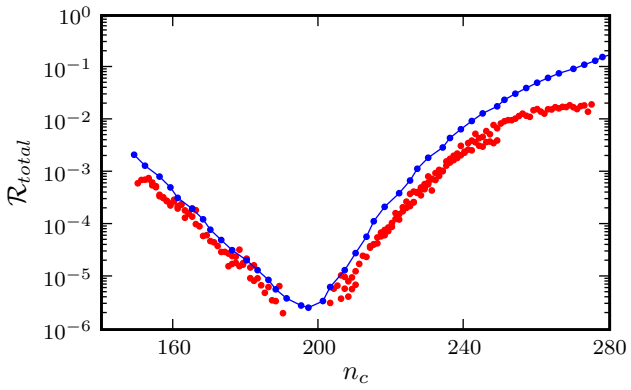

Figure 5.12: Red points show data from stochastic simulations of the microscopic dynamics. The time spent in a configuration with n_c condensates was averaged over multiple runs and the total rate to leave a given configuration was taken as the inverse of this average time. The blue curve shows the rate calculated by using equations (5.22) to determine the first-passage time to the peak and assuming a site at the peak is equally likely to fall into either well. All data calculated with $d_0 = 2.5$, $\phi = 50$, $\lambda = 3/50$, $\langle n \rangle = 100$ and on a lattice of length $L = 500$ sites.

brought about, for example, by a constraint on the total mass that may occupy a single site. We have determined the conditions on the hop rates within the ZRP that must be satisfied for saturated condensation to arise, and have investigated various aspects of the model's dynamics, both within and en-route to the steady state.

The scenario of isolated high and low density sites, however, does not correspond directly to the real bacterial systems we want, in the end, to model. In subsequent chapters we shall see similar separation into high and low density regions—though in these cases the domains will be spatially-extended, continguous regions rather than individual, isolated sites. Nevertheless, despite this distinction, the exact results we have been able to calculate here will be instructive in guiding our progress in investigating these more complex cases, where exact results will be difficult or even impossible.

Chapter 6

Interacting Particles II: Crowding Interactions and Finite Duration Tumbling

In the preceding chapter we investigated a zero-range interaction and identified a *saturated condensation* scenario that may occur within that model. Because the steady state of that system factorised we were able to exactly determine the steady state probability distribution and, from there, we could characterise the evolution of the system as it moved from a uniform flat profile towards its steady state. In particular, we found that the relaxation takes place in two stages: first, some number of condensate sites is selected which depends on the initial condition and is driven by a dynamic instability in the density profile, the conditions for which to exist we also derived. These condensates grow rapidly until arrested by the non-zero hopping rate even at very large on-site densities and a balancing of the rates into and out of the condensates. At this stage, however, the system remains in an out-of-equilibrium state that must then slowly relax through a process of activated evaporation and condensation events.

Isolated sites of high and low density are not, however, realistic as a model of real bacteria and in this chapter we will extend our analysis to the case of finite range interactions, where the isolated sites are replaced by extended domains. The manner in which we approach this change from zero to finite range interactions, and the way in which we coarse-grain the local density field in order to do so, turns out to be extremely important in determining the behaviour of

the system. Here, again, the example of the zero-range case is useful in guiding our examination.

Before we proceed with the finite range interaction, however, we first need to extend the zero-range model we analysed previously to account for the run and tumble nature of our bacterial dynamics and to move from a single particle species description to a two species model. We then use the field theoretic techniques from chapter 3 to derive the finite range results and, in so doing, re-derive the zero-range results from a new direction.

Towards the end of this chapter we shall further extend the results to higher dimensions and investigate the coarsening of the domains over time in two dimensions. Finally we consider means by which bacterial motility could be affected other than through a direct alteration of their mean velocity, and look at the effect of finite tumble duration.

6.1 Zero Range Interactions

Though there is no generic solution for the steady state of interacting run-and-tumble particles, there are limiting cases that can be solved exactly. We define the number of left and right going particles on a site as, respectively, n_i^- and n_i^+. The total occupancy of a site is then $n_i = n_i^+ + n_i^-$. The simplest interaction we can add is a zero-range interaction—as considered in chapter 5, though now generalised to multiple species of particle in order to account for run-and-tumble type dynamics—where the rate for a particle to jump from site i with occupancy (n_i^+, n_i^-) to site $i \pm 1$ is defined as $d_i^{\pm}(n_i^+, n_i^-)$ and is a function of the number of particles at the departure site but not dependent on the number of particles at the arrival site. With this addition we can now see more complex behaviour and non-trivial steady states, even for homogeneous and isotropic jump and tumble rates, but can still, under certain conditions presented below, calculate the stationary probability distribution exactly.

As for the single species zero-range process, we begin by assuming there exists a factorised form for the steady state probability distribution of the form

$$P\left(\left\{n_i^+, n_i^-\right\}\right) \propto \prod_{j=1}^{L} g_j(n_j^+, n_j^-). \tag{6.1}$$

This ansatz can then be substituted into the master equation for $P\left(\left\{n_i^+, n_i^-\right\}\right)$,

$$\begin{aligned}\partial_t P =& \sum_{k=1}^{L} (n_k^+ +1) d_k^+ (n_k^+ +1, n_k^-) P(n_k^+ + 1, n_{k+1}^+ - 1) - n_k^+ \, d_k^+ (n_k^+, n_k^-) P(n_k^+, n_{k+1}^+) \\ &+ (n_{k+1}^- + 1) \, d_{k+1}^- (n_{k+1}^+, n_{k+1}^- + 1) \, P(n_k^- - 1, n_{k+1}^- + 1) - \frac{\alpha_k^-}{2} n_k^- P(n_k^-, n_k^+) \\ &- n_{k+1}^- \, d_{k+1}^- (n_{k+1}^+, n_{k+1}^-) \, P(n_k^-, n_{k+1}^-) + \frac{\alpha_k^-}{2} (n_k^- + 1) P(n_k^- + 1, n_k^+ - 1) \\ &+ \frac{\alpha_k^+}{2} (n_k^+ + 1) P(n_k^- - 1, n_k^+ + 1) - \frac{\alpha_k^+}{2} n_k^+ P(n_k^-, n_k^+).\end{aligned} \tag{6.2}$$

Then, for periodic boundary conditions, one way we may choose to solve this equation is to separately balance the fluxes for right moving particles entering and exiting each site, left moving particles entering and exiting each site, and particles tumbling between species on each site. We then arrive at three sufficient conditions on the allowed rates for such a factorised form to exist:

$$\begin{aligned} g_i(n^+, n^- - 1) =& c \, n^- \, d_i^- (n^+, n^-) \, g_i(n^+, n^-) \\ g_i(n^+ - 1, n^-) =& c' \, n^+ \, d_i^+ (n^+, n^-) \, g_i(n^+, n^-) \\ g_i(n^+, n^-) \, n^- \, \alpha_i^- (n^+, n^-) =& g_i(n^+ + 1, n^- - 1) \, (n^+ + 1) \, \alpha_i^+ (n^+ + 1, n^- - 1), \end{aligned} \tag{6.3}$$

in which c and c' are arbitrary constants. The first two of these conditions are the same as Evans and Hanney found for their two species model without transmutation [6, 77], while the third arise from the need to balance tumbling between states on the same site. Note that, in principle, there may be other ways in which we can balance these terms which could arrive at different conditions on the rates.

Putting the three conditions (6.3) together and eliminating the factors $g_i(n^+, n^-)$ yields two constraints on our choice of rates:

$$d_i^- \left(n^+, n^-\right) \, d_i^+ \left(n^+, n^- - 1\right) = d_i^- \left(n^+ - 1, n^-\right) \, d_i^+ \left(n^+, n^-\right) \tag{6.4}$$

$$\frac{n^+ \, \alpha_i^+ \, (n^+, n^-)}{(n^- + 1) \alpha_i^- \, (n^+ - 1, n^- + 1)} = \frac{c}{c'} \frac{(n^- + 1) d_i^- \, (n^+ - 1, n^- + 1)}{n^+ \, d_i^+ \, (n^+, n^-)}. \tag{6.5}$$

One natural, but again not necessary, way to fulfil these conditions is to take

$$\begin{aligned} d_i^+(n^+, n^-) &= u_i^+(n^+)\,\omega_i(n^+ + n^-) \\ d_i^-(n^+, n^-) &= u_i^-(n^-)\,\omega_i(n^+ + n^-) \end{aligned} \tag{6.6}$$

for the jump rates. That is, the rate at which a left or right oriented particle moves is taken to be a product of a function of the number of particles oriented in that direction, and a function of the total number of particles on a site. Both functions can vary from site to site; the first can also depend on the particle species, but the second must be the same for both.

A sufficient conditions on the tumble rates is then to take

$$\alpha_i^+(n^+, n^-) = c u_i^+(n^+)\,A_i(n^+ + n^-) \tag{6.7}$$

$$\alpha_i^-(n^+, n^-) = c' u_i^-(n^-)\,A_i(n^+ + n^-). \tag{6.8}$$

The functions $u_i^+(n^+)$ and $u_i^-(n^-)$ are the same as in (6.6); $A_i(r)$ is a new, unconstrained, function that appears in both rates.

Up to a constant that can be subsumed into the normalisation, the marginals are given as

$$g_i(n^+, n^-) = \gamma^{n^-} \prod_{j=1}^{n^+} \frac{1}{j d_i^+(j, n^-)} \prod_{k=1}^{n^-} \frac{1}{k d_i^-(0, k)} = \gamma^{n^-} \prod_{r=1}^{n} \frac{1}{\omega_i(r)} \prod_{j=1}^{n^+} \frac{1}{j u_i^+(j)} \prod_{k=1}^{n^-} \frac{1}{k u_i^-(k)}, \tag{6.9}$$

where $\gamma = c/c'$ and $n = n^+ + n^-$. We can then re-write the probability of a given configuration as

$$P\left(\left\{n_i^+, n_i^-\right\}\right) = \frac{1}{Z} \prod_{i=1}^{L} g_i(n_i^+, n_i^-) = \frac{1}{Z} e^{\sum_{i=1}^{L} \ln\left(g_i(n_i^+, n_i^-)\right)}, \tag{6.10}$$

where Z is a normalisation, and define an effective single site free energy $f_i(n_i^+, n_i^-) = -\log(g_i(n_i^+, n_i^-))$. Note that this is independent of $\alpha_i^{\pm}(n^+, n^-)$; the way in which we chose to solve the master equation does not lead to factorised steady states for which the distribution can depend on the tumbling rates. As we saw that asymmetric tumble rates could affect the equilibrium distribution for the non-interacting case, we might suppose there are other solutions for the zero-range process which admit distributions dependent on the tumble rates. Whether

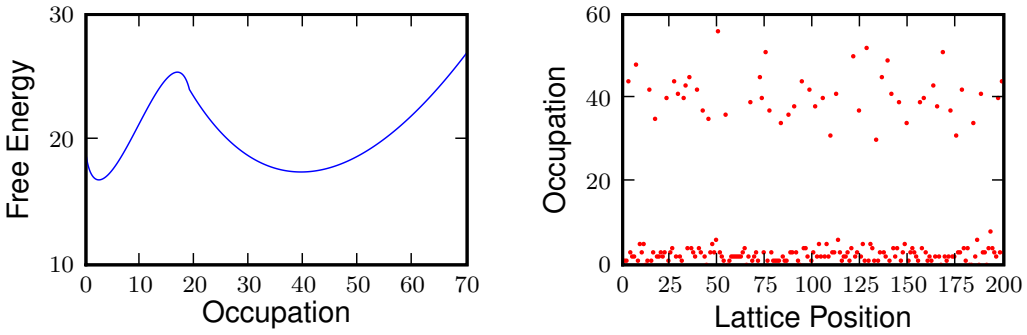

Figure 6.1: **Left**: The effective free energy density for the zero-range interaction with jump rate given by equation (6.11) for $\alpha_i^{\pm} = 1$, $\langle n_i \rangle = 12$, $n_m = 20$ and $v_0 = 10$. **Right**: A typical snapshot of the system during its relaxation towards equilibrium for the same parameters on a lattice of 200 sites and 2400 particles at $t = 1000$.

or not these allow for factorised steady states remains to be determined.

To foreshadow the finite range interaction we will examine in section 6.2, and to mimic the situation where an increase in density decreases the particles motility (as, for example, they get in each other's way) we now consider the following particular form of the steady state for this two-species ZRP for jump rates

$$d_i^{\pm}(n^+, n^-) = \begin{cases} v_0 \left[1 - (n^+ + n^-)/n_m\right] & \text{if } n^+ + n^- < n_m \\ v_0/n_m & \text{if } n^+ + n^- \geq n_m \end{cases} \tag{6.11}$$

and tumble rate $\alpha_i^{\pm} = \alpha$. That is, the tumble rate is constant per particle and the jump rate decreases linearly as density increases until reaching a constant rate of v_0/n_m at $n^+ + n^- = n_m - 1$. In this case the effective free energy is double welled and the system separates into isolated sites of high and low density. The relative numbers of high and low density sites to which the system first separates are initial condition dependent. The system then relaxes via a series of evaporations and condensations towards a fixed steady state. We see that the saturated condensation behaviour observed in chapter 5 is qualitatively reproduced for the two species zero range process. The free energy is shown in figure 6.1 along with a typical snapshot of the system.

To this behaviour we can then add a drift term, e.g. to simulate sedimentation, by biasing the jump rates in one direction and applying closed boundary conditions. We see all the high density sites collect at one end of the lattice

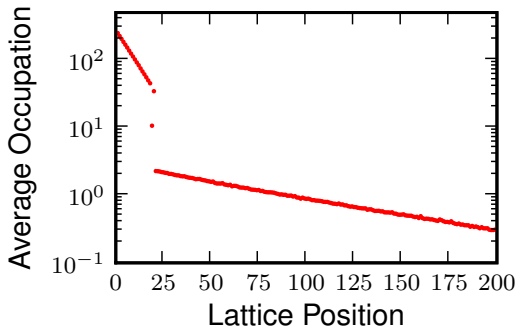

Figure 6.2: A time averaged snapshot of the steady state of zero-range process with parameters $n_m = 20$, $\langle n \rangle = 12$ $d_i^+ = 9$, $d_i^- = 11$, $\alpha_i^\pm = 1$. Data averaged from $10,000$ snapshots between $t = 40,000$ and $t = 50,000$

and the low density sites at the other, see figure 6.2.

6.1.1 Crowding Interactions

Having set up a field theory apparatus in chapter 3 to derive a fluctuating hydrodynamics for a general linear dependence on density in the jump rates, let us turn now to a specific class of interactions. In particular we consider a crowding interaction, where the velocity of the bacteria decreases with increasing density, in which case we expect to see our system separate into regions of high and low density as particles become trapped in regions of high density [4].

In general we expect to see qualitatively similar behaviour for any choice of $v(\rho)$ which decreases sufficiently quickly towards a finite non-zero velocity at high densities. In the following we use

$$v^\pm(\bar{\rho}^\pm) = \begin{cases} v_0\ (1 - (\bar{\rho}^\pm)/\rho_m) & \text{if } \bar{\rho}^\pm < \rho_m \\ v_0/\rho_m & \text{if } \bar{\rho}^\pm \geq \rho_m \end{cases}, \tag{6.12}$$

as we did for the exactly solvable zero-range process described in section 6.1.

6.1.2 Derivation of the Zero Range Steady State by Field Theoretic Methods

The field theory approach can describe many types of interaction, in particular let us now consider the zero range interaction we met in section 6.1 in the context of the fluctuating hydrodynamics we developed in section 3.2.1. This provides

us with a benchmark to check that our fluctuating hydrodynamics is consistent with the exact results we obtained previously.

For the zero-range process, where the velocity depends only on the occupation at the departure site, our kernel is given by $K_i^{\pm} = \delta_{i0}$ and in continuum $\bar{\rho}^{\pm}(x) = \rho(x)$. For simplicity, and to compare with our previous results we shall take $\alpha^{\pm}(\bar{\rho}) = \alpha$. This simplifies equation (3.38) considerably and, indeed, guarantees that $\alpha^+ v^- - \alpha^- v^+ = 0$. From section 3.2.3 we know that the fluctuating hydrodynamics describing the run-and-tumble bacteria with velocity given in equation (6.12) are given by

$$\begin{aligned} \dot{\rho} &= -\nabla J; \quad J = -D\nabla\rho - \frac{v_0}{\alpha}\Big(1-\frac{\rho}{\rho_m}\Big)\nabla\Big[v_0\Big(1-\frac{\rho}{\rho_m}\Big)\Big]\rho + \sqrt{2D\rho}\eta; \\ D &= \frac{v_0^2\Big(1-\frac{\rho}{\rho_m}\Big)^2}{\alpha}. \end{aligned} \tag{6.13}$$

The corresponding Fokker-Planck equation is given by

$$\dot{\mathcal{P}} = \int \mathrm{d}x \frac{\delta}{\delta\rho(x)}\partial_x\left[-\frac{v_0}{\alpha}\Big(1-\frac{\rho}{\rho_m}\Big)\partial_x\Big[v_0\Big(1-\frac{\rho}{\rho_m}\Big)\Big]\rho - D\partial_x\rho - D\rho\left(\partial_x\frac{\delta}{\delta\rho(x)}\right)\right]\mathcal{P}. \tag{6.14}$$

Note that a term $\nabla\frac{\delta}{\delta\rho}[D(\rho)]$ could be present in equation 6.14, but vanishes for symmetry reasons (See [4, 78]). Looking for a free energy $P \propto \exp[-\mathcal{F}[\rho]]$ one gets

$$-\nabla\frac{\delta\mathcal{F}}{\delta\rho} = -\nabla\Big[\log\rho + \log\Big(\Big(1-\frac{\rho}{\rho_m}\Big)\Big)\Big], \tag{6.15}$$

whose solution is

$$\mathcal{F}[\rho] = \int \mathrm{d}x\rho(\log\rho - 1) - (\rho_m - \rho)\Big[\log\Big(1-\frac{\rho}{\rho_m}\Big) - 1\Big], \qquad \text{for } \rho < \rho_m. \tag{6.16}$$

For $\rho \geq \rho_m$ the free energy density $f(\rho(x))$ is given by

$$f(\rho(x)) = \rho\left(\log\left(\frac{\rho}{\rho_m}\right) - 1\right), \tag{6.17}$$

which corresponds precisely to the free energy calculated exactly in section 6.1 (and shown in figure 6.1) for the total occupancy and in the continuum limit. An example of this free energy for one choice of parameters is shown in figure 6.1 (left).

6.2 Finite Range Interactions

We saw in section 6.1.2 that our fluctuating hydrodynamics admitted a free energy and accurately reproduced the exact results for the zero-range process detailed in section 6.1. Let us now extend that analysis to a system with finite range interactions. As before we now take the coarse grained density $\bar{\rho}^{\pm}$ to be given by

$$\bar{\rho}^{\pm}(x) = \int K^{\pm}(x-y)\rho(y)\mathrm{d}y. \tag{6.18}$$

For smooth profiles, we hope that the differences between $\bar{\rho}^{\pm}$ and ρ are small so we can treat the free energy in equation (6.16) as a mean field theory. This way we can still use the free energy we derived in section 6.1.2 to predict the coexistence densities and instability to spinodal decomposition. The finite range nature of the interactions will introduce correlations between sites which we hope will manifest only via the surface tension [4]. We hope that this surface tension will only effect a clustering of the high and low density sites without affecting the coexistence densities. If the mean field theory captures the picture correctly, spinodal decomposition occurs whenever the second derivative of the free energy density is negative, i.e. for

$$\frac{1}{\rho} + \nabla \log v[\rho] < 0 \Leftrightarrow \frac{1}{\rho} - \frac{1}{\rho_m - \rho} < 0. \tag{6.19}$$

Thus, whenever $\rho_m > \rho > \rho_m/2$, the system should be unstable with respect to spinodal decomposition.

Isotropic Kernels

If we use an isotropic kernel to calculate $\bar{\rho}^{\pm}$ in our jump rates we do indeed recover results consistent with the zero-range free energy. That is, if we take $K^{+}(x-y) = K^{-}(x-y)$ our simulations match the free energy predictions. In particular, we have worked with a Gaussian kernel, where $K^{\pm}(x) = \exp(-x^2/k)/Z$, with Z a normalisation and k a parameter to control the range of the interaction. The results of simulations using this kernel are shown in figure 6.3 along with the predicted average high and low densities from the free energy. To calculate the coexisting densities of the high and low density sites we form a double tangent construction on the free energy [79]. As hoped the finite range nature of the

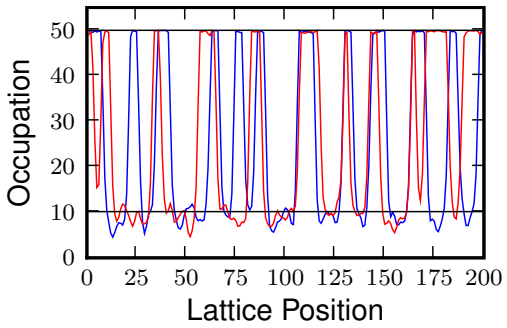

Figure 6.3: Snapshot of typical density profiles for an average run length of 100 sites (red) and 10 sites (blue) for the isotropic, Gaussian kernel. The black lines show the predicted average high and low densities. Data recorded at $t = 1000$ using 5000 particles with $n_m = 50$, $k = 2$ and $\alpha = 1$.

interactions effectively creates a surface tension, but does not significantly alter the coexistence densities. Further, as expected we see no dependence in the steady state on our choice of v_0 and α.

Anisotropic Kernels

For anisotropic coarse graining kernels, however, the situation is more complex. One simple and natural way to introduce an anisotropic kernel is to account for the finite volume of bacteria by stating that there can be at most n_m bacteria on each lattice site and taking the occupancy at the arrival site as our $\bar{n}$ in equation (3.10). This forms a generalisation of the partial exclusion process [50, 80] and results in the jump rates

$$d_i^{\pm}(n_i^+, n_i^-) = d_i^{\pm}\left(1 - \frac{n_{i\pm1}}{n_m}\right). \tag{6.20}$$

In this case the effective free energy is limited to a region where $\rho < \rho_m$ and this section is sketched in figure 6.4. A double tangent construction amounts to looking for a density ρ_{low} such that the tangent of the free energy density at this point meets with the free energy density at $\rho = \rho_m$, as can be seen from inspection of figure 6.4. This amounts to finding ρ such that

$$2\left(\frac{\rho}{\rho_m} - 1\right) = \log\frac{\rho}{\rho_m}, \tag{6.21}$$

which can be solved numerically and yields for the low density ρ_{low} that coexists

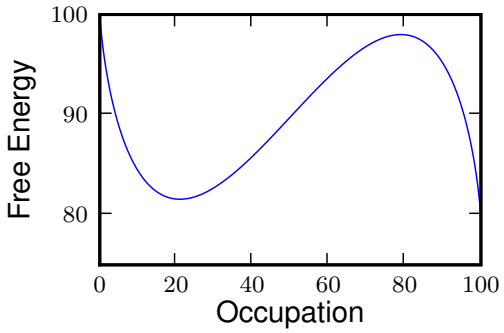

Figure 6.4: Free energy density of the exclusion model where the occupation of a site is constrained to be smaller or equal to 100 particles by the choice of rates (6.20).

with ρ_m

$$\frac{\rho_{low}}{\rho_m} = .203188. \tag{6.22}$$

For a total average density larger that ρ_{low}, the steady state should thus be a combination of two phases, one with $\rho = \rho_{low}$ and one with $\rho = \rho_m$, the ratio of the amounts of the two phases being set by constraint on the global mass.

Interestingly, although the theory correctly predicts a change from a flat profile to phase separation, on examining the results of simulations of the underlying lattice system we found that the densities into which the system separates do not correspond to those predicted by the continuum theory. Indeed, while the continuum theory had no dependence on the tumble rate α or the coefficient of the jump rate v_0, the simulations for an anisotropic kernel showed a strong dependence on the ratio of these two parameters. The lower and upper densities both varied considerably with the average run length $r \equiv v_0/\alpha$, as shown in figure 6.5, and below $r = 4$ we see no separation at all.

This discrepancy is not limited to the particular choice of anisotropic kernel we use as illustration above and is general to any anisotropic choice of $K^{\pm}(x)$. We have also conducted simulations with smooth anisotropic kernels without a hard limit on the number of particles per site, and saw exactly the same qualitative effect. Thus we have seen that the relevant factor is indeed the isotropy of the kernel but although the origin of the difference has been established, a comprehensive explanation for the variation between isotropic and anisotropic kernels is yet to be formulated.

Note that it is not in itself surprising that a fluctuating hydrodynamics

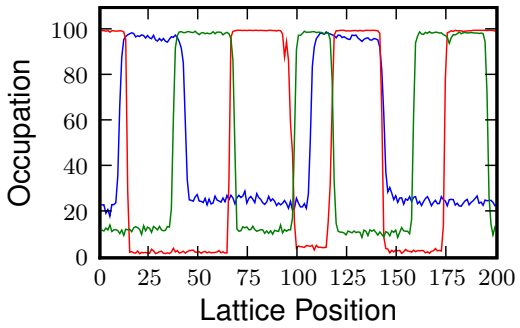

Figure 6.5: Snapshots of typical density profiles for an average run length of 100 sites (red), 20 sites (green) and 10 sites (blue). Data recorded at $t = 1000$ with $\alpha = 1$, $n_m = 100$ and from $10,000$ particles.

developed to describe smooth profiles fails to quantitatively amount for the coexisting densities of profiles of alternating high and low densities. One of the reasons our fluctuating hydrodynamics works so well for the isotropic case is that we always consider large occupancies on each lattice site. This means that the model is close to mean-field in the same sense as the large spin limit of a spin chain is well described by a continuous spin chain [50]. Smaller occupancies would lead to quantitative differences between the predicted coexisting densities and those predicted from the fluctuating hydrodynamics, even for isotropic kernels. Furthermore, the Ito drift that was neglected in equation (6.14) for symmetry reasons would not vanish for the anisotropic case. In fact even for the off-lattice model, the fluctuating hydrodynamics developed previously [4] is only valid for isotropic kernels and the quantitative mismatch between the fluctuating hydrodynamics and the simulations on lattice for anisotropic kernels is thus not that surprising. We nevertheless now try to shed some light on its origin.

Stability Analysis

One way we can analyse the difference between the isotropic and anisotropic interaction kernels is to examine the dynamic stability of the two systems. We consider a one dimensional system evolving from a homogeneous state under a small perturbation and determine whether the system is dynamically stable or unstable, whether the perturbations will, on average, grow or shrink.

One possibility is that the discrepancies we saw in figure 6.5 between the theory and simulations arise from the assumptions behind the diffusive limit taken

in the field theory, see section 3.2.1 and Appendix A. We therefore start from the continuum microscopic mean field equations for homogeneous and isotropic rates, i.e. after the continuum limit has been taken but before the diffusive limit,

$$\dot{\rho}^+ = -v\nabla\left[\rho^+\left(1-\frac{\rho}{\rho_m}\right)\right] - \frac{\alpha\,\rho^+}{2} + \frac{\alpha\,\rho^-}{2} \tag{6.23}$$

$$\dot{\rho}^- = v\nabla\left[\rho^-\left(1-\frac{\rho}{\rho_m}\right)\right] + \frac{\alpha\,\rho^+}{2} - \frac{\alpha\,\rho^-}{2}. \tag{6.24}$$

We expand around a flat profile and Fourier transform. We take $\rho^{\pm}(x) = \rho_0/2 + \sum_q \delta_q^{\pm}\exp(i\,q\,x)$ and arrive at

$$\dot{\delta}_q^+ = -v\,\delta_q^+\,i\,q\left(1-\frac{\rho_0}{\rho_m}\right) + v\,i\,q\,\frac{\rho_0}{2\,\rho_m}\left(\delta_q^+ + \delta_q^-\right) - \frac{\alpha}{2}\left(\delta_q^+ - \delta_q^-\right) \tag{6.25}$$

$$\dot{\delta}_q^- = v\,\delta_q^-\,i\,q\left(1-\frac{\rho_0}{\rho_m}\right) - v\,i\,q\,\frac{\rho_0}{2\,\rho_m}\left(\delta_q^+ + \delta_q^-\right) + \frac{\alpha}{2}\left(\delta_q^+ - \delta_q^-\right). \tag{6.26}$$

We can re-write these two equations in matrix form as

$$\dot{\delta_{\mathbf{q}}} = \begin{pmatrix} -v\,i\,q\left(1-\frac{3\,\rho_0}{2\,\rho_m}\right) - \frac{\alpha}{2} & v\,i\,q\frac{\rho_0}{2\,\rho_m} + \frac{\alpha}{2} \\ -v\,i\,q\frac{\rho_0}{2\,\rho_m} + \frac{\alpha}{2} & v\,i\,q\left(1-\frac{3\,\rho_0}{2\,\rho_m}\right) - \frac{\alpha}{2} \end{pmatrix}\delta_{\mathbf{q}}; \qquad \delta_{\mathbf{q}} = \begin{pmatrix} \delta_q^+ \\ \delta_q^- \end{pmatrix}. \tag{6.27}$$

The eigenvalues of this matrix, which will then tell us whether the flat profile is stable or unstable to small perturbations, are

$$\lambda_{\pm}(q) = -\frac{\alpha}{2} \pm \left(\frac{\alpha^2}{4} + v^2\,q^2\left(1-\frac{\rho_0}{\rho_m}\right)\left(\frac{2\,\rho_0}{\rho_m}-1\right)\right)^{1/2}. \tag{6.28}$$

It is clear that one of these eigenvalues will always be negative while the other is negative for $\rho_0 < \rho_m/2$ and positive for $\rho_0 > \rho_m/2$. Hence a homogeneously flat profile is stable when the average total density is less than half the maximum density and unstable above that, with no dependency on run length. This corresponds precisely with the stability predicted by the free energy derived in section 6.2. That stability analysis was derived from a free energy which considered only the total density (rather than the density of left and right moving particles separately) and was itself calculated only after assuming a diffusive scaling. That the diffusive scaling does not alter the criterion for instability supports taking that limit and implies that the discrepancy between our lattice

simulations and continuum free energy arises from another source.

We turn, then, to consider the dynamic stability of the lattice dynamics directly. Beginning with the mean field equations for the anisotropic partial exclusion process,

$$\dot{n}_i^+ = d\, n_{i-1}^+ \left(1 - \frac{n_i}{n_m}\right) - d\, n_i^+ \left(1 - \frac{n_{i+1}}{n_m}\right) - \frac{\alpha\, n_i^+}{2} + \frac{\alpha\, n_i^-}{2} \tag{6.29}$$

$$\dot{n}_i^- = d\, n_{i+1}^- \left(1 - \frac{n_i}{n_m}\right) - d\, n_i^- \left(1 - \frac{n_{i-1}}{n_m}\right) + \frac{\alpha\, n_i^+}{2} - \frac{\alpha\, n_i^-}{2} \tag{6.30}$$

we expand around a flat profile, taking $n_k^\pm = n_0 + \sum_q \delta_q^\pm \exp(i\, q\, k)$. After some algebra, detailed in Appendix C, we arrive at a condition for there to exist positive eigenvalues, i.e. for a flat profile to be unstable to small perturbations. Specifically we see instability whenever the run length $r = d/\alpha$ satisfies the following inequality

$$r > \frac{1}{2\left(1 - \frac{n_0}{n_m}\right)\left(\frac{2\,n_0}{n_m} - 1\right)}. \tag{6.31}$$

Graphing this we can see that a flat profile will be stable in region I of figure 6.6 and unstable in region II. We see that for short run lengths the range of densities in which the system will spinodally decompose is restricted and at run lengths below 4 sites there is no separation at all. Conversely, in the limit that the run length tends to infinity, i.e. where we effectively have two totally asymmetric partial exclusion processes on the same lattice, the system is unstable for any density between $\frac{n_0}{n_m} = 0.5$ and $\frac{n_0}{n_m} = 1$. This instability is in accordance with that seen in our simulations.

In our simulations we found that when we replaced the anisotropic kernel in the interaction terms with an isotropic one we recovered the density profiles predicted by the continuous theory. We can also analyse the effect of an isotropic density kernel on the dynamic stability.

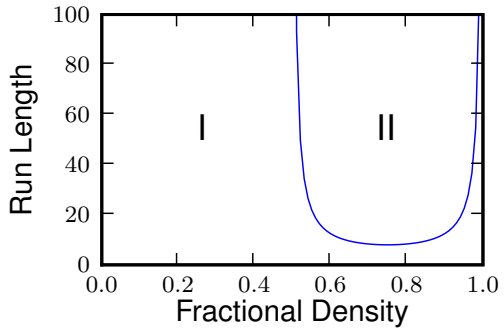

Figure 6.6: A flat profile is stable when in region I, but unstable in region II, for a system with exclusion and homogeneous, isotropic jump and tumble rates. The x-axis is the fractional density, i.e. n/n_m.

Consider now the microscopic mean field equations

$$\begin{aligned}\dot{n}^+ &= dn^+_{i-1}\left(1-\frac{1}{n_m}\sum_j K^+_j n_{i+j-1}\right) - dn^+_i\left(1-\frac{1}{n_m}\sum_j K^+_j n_{i+j}\right) - \frac{\alpha n^+_i}{2} + \frac{\alpha n^-_i}{2}\\ \dot{n}^- &= dn^-_{i+1}\left(1-\frac{1}{n_m}\sum_j K^-_j n_{i+j+1}\right) - dn^-_i\left(1-\frac{1}{n_m}\sum_j K^-_j n_{i+j}\right) + \frac{\alpha n^+_i}{2} - \frac{\alpha n^-_i}{2}.\end{aligned} \tag{6.32}$$

In general $K^\pm_j$ can take any values, we enforce only that they are both normalised, i.e. that $\sum_j K^\pm_j = 1$. Relaxing this constraint would effectively re-normalise the maximum density. This more general interaction reduces to the simple exclusion case if we take $K^\pm_j = \delta_{\pm 1,j}$ and to the zero-range case if we take $K^\pm_j = \delta_{0,j}$.

For an isotropic kernel, where $K^\pm_i = K_i$, when we expand around a flat profile we find that there exists a q such that $\lambda_+(q)$ is greater than 0 if and only if $n_m > n_0 > 0.5\,n_m$, see Appendix C for details, which matches the condition we derived from our continuum free energy. Thus for an isotropic interaction kernel we recover the continuum stability result while an anisotropic kernel will, in general, not produce the same result. It thus seems the error comes from the continuum limit itself, which is not valid for anisotropic kernels. While the stability analysis accounts qualitatively for the difference between isotropic and anisotropic kernels a theory which quantitatively accounts for the differences in coexistence densities at steady state remains to be constructed.

6.3 Finite Range Interactions in 2D

Most cases of physical interest require a model in more than one dimension; it is therefore natural to extend our analysis to higher dimensions. This can be done on lattice relatively easily. On a square lattice in two dimensions we allow the particles to jump between nearest neighbours. We therefore consider 4 types of particle now instead of 2. We find that in two dimensions, the behaviour of the run-and-tumble crowding model is qualitatively the same as in one. The system separates into regions of high and low density, where those co-existent densities are given by the same free energy as in one dimension. The field theoretic approach developed in section 3.2.1 indeed generalises straightforwardly to higher dimensions and yields the same fluctuating hydrodynamics. We find, however, that allowing only nearest neighbour hopping results in an unrealistic surface tension because of the anisotropy of the lattice [81, 82]; the regions of high and low density form elongated, and thus anisotropic, domains, see figure 6.7 (left).

To correct this unphysical characteristic of our model we extend our dynamics to allow next to nearest hopping along diagonal directions and consider 8 species of particles, where the jump rates in the diagonal directions are scaled by a factor of $\sqrt{2}$. The droplets then coarsen into more realistic curved domains, see figure 6.7 (right).

The stability conditions remain the same as do the coexistence densities and the discrepancy between isotropic and anisotropic kernels. We examined simulations with both the anisotropic partial exclusion kernel, and the isotropic, Gaussian kernel on lattices of 500x500 sites for densities above the spinodal point. The systems were seen to separate into droplets of higher and lower density which then coarsened into discrete, contiguous domains, see figure 6.7.

We measured the coarsening of these domains and found them to scale as $t^{1/3}$, as we would expect for conserved model B type dynamics[1] [84]. An approximate measurement of the size of the domains was calculated by randomly sampling the system and measuring the horizontal and vertical size of the encountered droplet

[1]Under the classification determined by Halperin and Hohenberg, model B is defined as a Time-Dependent Ginzburg-Landau model with (critically) a conserved n-component order parameter. Their schema classifies dynamic critical phenomena into a variety of models listed from A to J [83].

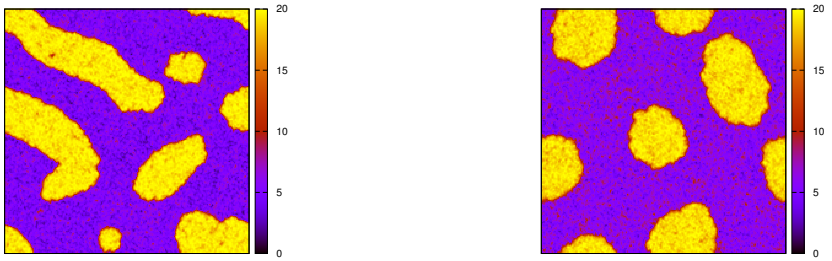

Figure 6.7: Snapshots of the two dimensional system using the partial asymmetric exclusion and parameters $n_m = 20$, $d_0 = 10$ and $\alpha = 1$. Explicitly, the jump rates are given by $d(\bar{n}) = 10(1 - \bar{n}/20)$ for $\bar{n} < 20$ and $d(\bar{n}) = 1/2$ for $\bar{n} > 20$, where $\bar{n}_{ij} = \sum_k \sum_l 1/Z \exp(-((i-k)^2 + (j-l)^2)/\kappa) n_{kl}$ and $\kappa = 2$. Occupation of sites is indicated by colour (see the bar next to each plot for numbers). **Left**: allowing only nearest neighbour hops and no diagonal movement. **Right**: allowing for diagonal hops. Both simulations performed using $400,000$ particles and recorded at $t = 2500$.

at that point. Mathematically, we define

$$\begin{aligned} L_x(i,j) &= \max\{k \in \mathbb{N} : |n_{i,j} - n_{i+m,j}| < n^*,\ \forall m \in [0,k]\} \\ &+ \max\{k \in \mathbb{N} : |n_{i,j} - n_{i-m,j}| < n^*,\ \forall m \in [0,k]\}, \end{aligned} \tag{6.33}$$

where n^* is an arbitrary cutoff to distinguish the two domains but ignore random fluctuations. Computations were made with a number of choices for n^* and the particular choice of cutoff was found to have no significant effect on the results. We calculate the vertical size in an analogous fashion and average the lengths over a large number of points on the lattice. Though this does not give an exact measure of the droplet size it is sufficient to show the scaling of the domain size with time whilst being quick to calculate numerically.

Using this procedure we determine that the domains increase in size with an exponent of approximately 1/3, i.e. $\langle L_x \rangle (t') = (t'/t)^{1/3} \langle L_x \rangle (t)$. The two-point, connected, equal time correlation function $C(j,t) = \langle n_i(t)\, n_{i+j}(t) \rangle - \langle n_i(t) \rangle \langle n_{i+j}(t) \rangle$ was also calculated numerically from the data and fit reasonably with a re-scaling $C(x,t) = C(x/a^{1/3}, t\,a)$. The data for both these measurements can be seen in figure 6.8.

As can be seen from the figures the choice of kernel does not change the

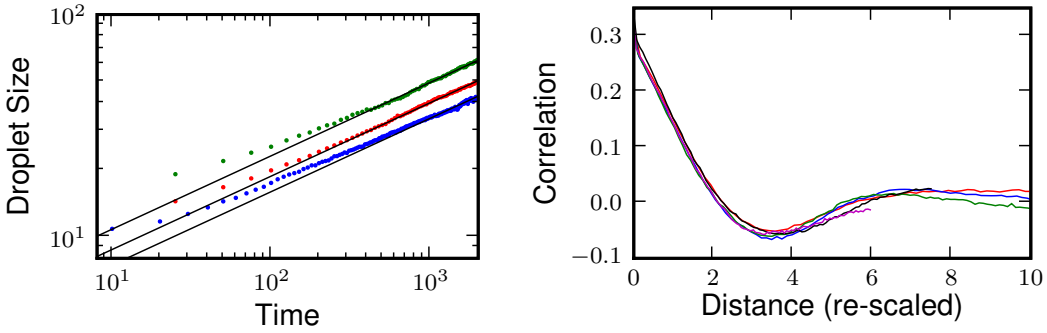

Figure 6.8: **Left**: The average diameter of domains over time for an anisotropic kernel (green), Gaussian kernel with $k = 1$ (red) and $k = 2$ (blue). The solid lines show asymptotic behaviour with an exponent of $1/3$. **Right**: The correlation function $C(j, t)$ for the anisotropic kernel simulations. The x-axis has been rescaled $x \to x/t^{0.33}$ so that data computed at $t = 250$ (red), $t = 500$ (blue), $t = 1000$ (green), $t = 2500$ (black) and $t = 5000$ (magenta) superimpose. Both figures derived from data for $240,000$ particles and with parameters $n_m = 10$, $\alpha = 1$ and $d_0 = 10$ on a lattice of 200×200 sites.

coarsening exponent, only the relative speed of coarsening, with interactions over a larger number of sites taking longer to reach a steady state than those with shorter ranges.

6.4 Hydrodynamics with Finite Tumbling Duration

For wild-type *E. coli* the typical tumble duration is much shorter than the time between two tumbles (approximately $0.1s$ tumbling against $1s$ swimming) so that most of the literature on bacterial motility relies on models with instantaneous tumbles. The implications of finite tumble duration have been considered in several papers [4,24,27], but in those cases it was concluded that such modification resulted primarily in only minor quantitative changes.

As we will show in this section (and expand upon further in chapter 7), however, when we allow the switching rates between tumbling and running to depend on bacterial density, the finite tumble duration can play a major role in patterning processes and must be explicitly included within the model. We therefore define our system by two densities, that of running bacteria and that of tumbling bacteria, and three dynamical parameters, the swim speed, the tumble

rate and tumble duration. We shall also perform these calculations explicitly in an arbitrary number of dimensions, d, in order that they be as general as possible and can be easily applied to the two dimensional results we will examine in chapter 7.

We start with a single run-and-tumble particle at position $\mathbf{x}$ at time t and with velocity $\mathbf{v} = v\,\mathbf{u}$, where $\mathbf{u}$ is a unit vector denoting the direction the particle faces. We define $R(\mathbf{u}, \mathbf{x}, t)$ and $T(\mathbf{x}, t)$ as the probability of finding it in a running or tumbling state respectively. Note that in the tumbling state we do not define a direction $\mathbf{u}$.

For clarity we will, initially, consider only constant run speed v, R to T interconversion rate α and reverse conversion rate β. Our dynamics are then governed by the equations

$$\begin{aligned} \dot{R}(\mathbf{u}, \mathbf{x}, t) &= -\nabla \cdot (\mathbf{v} R(\mathbf{u}, \mathbf{x}, t)) - \alpha R(\mathbf{u}, \mathbf{x}, t) + \frac{1}{\Omega}\beta T(\mathbf{x}, t) \\ \dot{T}(\mathbf{x}, t) &= \alpha \int_S R(\mathbf{u}, \mathbf{x}, t) \mathrm{d}S - \beta T(\mathbf{x}, t), \end{aligned} \tag{6.34}$$

where the integral in the second line is over all directions and Ω is the solid angle, in d dimensions given $d\pi^{d/2}/\Gamma(d/2+1)$. Introducing the total density of running particles (in any direction) $P = \int_S R \mathrm{d}S$ and the total density of all particles (in any state) $\rho = P + T$, we see by summing equations (6.34) that

$$\begin{aligned} \dot{\rho}(\mathbf{x}, t) &= -\nabla \cdot \mathbf{J}(\mathbf{x}, t) \\ \dot{\mathbf{J}}(\mathbf{x}, t) &= \int_S \left[\mathbf{v} \nabla \cdot (\mathbf{v} R(\mathbf{u}, \mathbf{x}, t)) + \frac{\beta}{\Omega} \mathbf{v} T(\mathbf{x}, t) - \alpha \mathbf{v} R(\mathbf{u}, \mathbf{x}, t) \right] \mathrm{d}S. \end{aligned} \tag{6.35}$$

We now define $G_i = \int_S v_i \partial_j v_j \, R(\mathbf{u}, \mathbf{x}, t) \mathrm{d}S$ and $H_{ij} = \int_S v_i v_j \, R(\mathbf{u}, \mathbf{x}, t) \mathrm{d}S$, so that

$$\dot{J}_i = -G_i - \alpha J_i. \tag{6.36}$$

If we now take the time derivative of G_i we obtain

$$\begin{aligned} \dot{G}_i = &\int_S v_i \partial_j v_j \partial_k v_k R \mathrm{d}S \\ &+ \int_S v_i \partial_j v_j \frac{\beta T}{\Omega} \mathrm{d}S - \int_S v_i \partial_j v_j \alpha R \mathrm{d}S. \end{aligned} \tag{6.37}$$

The final term in equation (6.37) can be split to read

$$\begin{aligned}\int_S v_i\partial_j v_j \alpha R \mathrm{d}S &= (\partial_j\alpha)\int_S v_i v_j R\mathrm{d}S + \alpha\int_S v_i\partial_j v_j R\mathrm{d}S \\ &= (\partial_j\alpha)\, H_{ij} + \alpha G_i.\end{aligned} \tag{6.38}$$

Then, taking the time derivative of H_{ij} we obtain

$$\dot{H}_{ij} = -\int_S v_i v_j \partial_k v_k R\mathrm{d}S + \frac{\beta T}{\Omega}\int_S v_i v_j \mathrm{d}S - \alpha H_{ij} \tag{6.39}$$

Noting that the second term in that equation can be simplified by the identity

$$\int_S u_i u_j \mathrm{d}S = \frac{\Omega}{d}\delta_{ij}, \tag{6.40}$$

so that

$$\dot{H}_{ij} = -\int_S v_i v_j \partial_k v_k R\mathrm{d}S + \frac{v^2\beta T}{d}\delta_{ij} - \alpha H_{ij}. \tag{6.41}$$

In general we will want to examine the large length scale behaviour of the system and so, following the rescaling we applied in section 3.2.2, we now make a diffusive approximation; that is we let $t \to \ell^2 t$ and $x \to \ell x$ and match terms of equal order in powers of $1/\ell$. In doing this we arrive at the approximation for H,

$$H_{ij} = \frac{v^2\beta T}{d\alpha}\delta_{ij}. \tag{6.42}$$

Returning to equation (6.37), the second term on the right hand side can be expanded as

$$\begin{aligned}\int_S v_i\partial_j v_j \frac{\beta T}{\Omega}\mathrm{d}S &= \int_S u_i u_j \mathrm{d}S \frac{v\beta\partial_j vT}{\Omega} + \int_S u_i\partial_j u_j \mathrm{d}S\frac{v^2\beta T}{\Omega} \\ &= \frac{v\beta\partial_i vT}{d},\end{aligned} \tag{6.43}$$

where the second term on the right hand side vanishes by symmetry and the first term was simplified using equation (6.40). Equation (6.37) can then be simplified to read

$$\dot{G}_i = \int_S v_i\partial_j v_j\partial_k v_k R\mathrm{d}S - \alpha G_i - (\partial_j\alpha)\frac{v^2\beta T}{d\alpha}\delta_{ij} + \frac{v\beta\partial_i vT}{d}. \tag{6.44}$$

Finally, under another diffusive rescaling, and combining terms, we can write G_i as

$$G_i = \frac{v\beta}{d}\partial_i\left(\frac{vT}{\alpha}\right), \tag{6.45}$$

and, subsequently,

$$J_i = -\frac{1}{\alpha}\frac{v\beta}{d}\partial_i\left(\frac{vT}{\alpha}\right). \tag{6.46}$$

To now remove the explicit reference to the probability density of tumbling particles, and leave us with a single probability density to find a particle in any state, we return to equation (6.34) and take the second time derivative of T to yield

$$\begin{aligned}\ddot{T} &= \alpha\int_S \dot{R}\mathrm{d}S - \beta\dot{T} \\ &= \alpha\left[-\nabla\cdot\mathbf{J} + \beta T - \alpha P\right] - \beta\alpha P - \beta^2 T.\end{aligned} \tag{6.47}$$

Again, following a diffusive approximation, we find that only the final four terms of equation (6.47) are relevant under the re-scaling and we can write

$$0 = \alpha\beta T - \alpha^2 P - \beta\alpha P - \alpha\beta^2 T. \tag{6.48}$$

Replacing $P = \rho - T$ and rearranging this equation then leads us to

$$T = \frac{\alpha}{\beta}P \quad \rightarrow \quad T = \frac{\alpha}{\alpha+\beta}\rho. \tag{6.49}$$

Putting all this together, then, we arrive at the equations

$$\begin{aligned}\dot{\rho} &= -\nabla\cdot\mathbf{J} \\ \mathbf{J} &= -D\nabla\rho + \mathbf{V}\rho \\ D &= \frac{v^2}{d\alpha(1+\alpha/\beta)} \\ \mathbf{V} &= -\frac{v}{d\alpha}\nabla[\frac{v}{1+\alpha/\beta}].\end{aligned} \tag{6.50}$$

The hydrodynamic equations derived by Cates and Tailleur [4] for the behaviour of run-and-tumble bacteria in one dimension and with instantaneous tumbles, are thus generalised to cover finite duration tumbling and movement in an arbitrary number of dimensions.

6.5 Density Dependent Tumbling Rate and Duration

Consider now, as an explicit example, the case where v is independent of the local density but the tumbling rate α and tumble duration $\tau = \beta^{-1}$ are functions of ρ. The large scale long time dynamics is then given by

$$\begin{aligned} \dot{\rho} &= -\nabla \cdot \mathbf{J} \\ \mathbf{J} &= -D\nabla\rho + \mathbf{V}\rho \\ D &= \frac{v^2}{\alpha(1+\alpha\tau)} \\ \mathbf{V} &= D\frac{\nabla[\alpha\tau]}{1+\alpha\tau} = D\nabla\log(1+\alpha\tau) \end{aligned} \tag{6.51}$$

Note that this dynamics can be recast under a pure diffusion equation with density dependent *collective* diffusivity D_c

$$\dot{\rho} = \nabla \cdot (D_c(\rho)\nabla\rho)\,; \quad D_c = D(1 - \frac{\frac{\mathrm{d}}{\mathrm{d}\rho}(\alpha\tau)}{1+\alpha\tau}) \tag{6.52}$$

If the tumbling rate or the tumbling duration increases with density, this can have the same effect as the velocity of the particles decreasing with density. Consider, as a mathematically simple example, an exponentially increasing rate, $\alpha\tau = \alpha_0\tau_0 \mathrm{e}^{\lambda\rho}$, then a flat profile becomes unstable when $D_c < 0$, i.e. when

$$\frac{1}{\rho} < \frac{\alpha\tau}{1+\alpha\tau}\lambda \tag{6.53}$$

When $\rho \to \infty$, the r.h.s goes to λ while the l.h.s goes to zero, so that at high enough density, flat profiles will indeed be unstable, as shown in the illustrative snapshot in figure 6.9.

In chapter 7 we shall return to a variant of this model and discuss the implications and relevance of it in more detail in the context for a colony of bacteria undergoing both density dependent interactions and cell division.

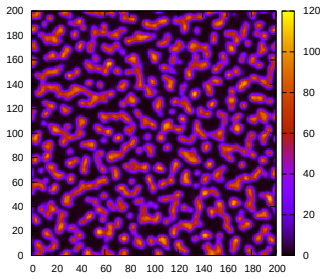

Figure 6.9: Snapshot of a simulation of a system with $\tau = \exp(0.1\bar{\rho})$, $\alpha = 1$, $v = 10$. Recorded at $t = 100$ from a simulation of $1,000,000$ particles on a lattice of length $L = 200$ sites.

6.6 Non-local interactions and surface tension

In section 6.2 we considered the implications of finite range interactions and defined a kernel $K(x)$. One effect of allowing the dynamics to depend on a coarse-grained density, which is not strictly local, is to create an effective surface tension and replace isolated sites of high or low density with continuous, extended domains.

In previous, continuum studies interacting run-and-tumble bacteria (such as the no-growth limit of Cates et al. [1]), a semi-phenomenological approach was taken to the dynamics and to the diffusion equation was added an ad-hoc surface tension:

$$\dot{\rho} = \nabla[D_c(\rho)\nabla\rho] - \kappa\Delta^2\rho. \tag{6.54}$$

In equation (6.54) D_c is the collective diffusion, as in the previous section, ρ_0 is a carrying capacity and κ controls the surface tension.

The parameter κ in equation (6.54) is phenomenological. Following our procedure to coarse-grain the local density, however, we can derive an expression for κ from our microscopic parameters.

In principle, the density field of N interacting bacteria is defined as $\rho(x) = \sum_{i=1}^{N} \delta(x - x_i)$. However, physically the Dirac functions have to be smoothed out, at least on the level of particle size, or more probably at the level of the run-length, on which bacteria measures the local gradient of chemicals. Replacing $\delta(x - x_i)$ by a smooth slightly non-local function creates higher order gradient in

the equations of motion that are responsible for the surface tension term. Let us define

$$\bar{\rho}(x) = \int \mathrm{d}y K(x-y)\rho(x) = \int \mathrm{d}y K(y)\rho(x-y) \tag{6.55}$$

and expand $\bar{\rho}(x)$ in gradients of ρ

$$\begin{aligned} \bar{\rho}(x) &= \rho(x) + a\nabla\rho + \sigma\Delta\rho + \mathcal{O}\left(\nabla^3\rho\right) && (6.56)\\ a &= \int \mathrm{d}y K(y)\, y && (6.57)\\ \sigma &= \int \mathrm{d}y K(y)\, y^2 && (6.58)\\ & && (6.59) \end{aligned}$$

Note that for a symmetric kernel, $K(x)$, $a = 0$ and thus $\bar{\rho}(x) = \rho(x) + \sigma\Delta\rho$.

Then, for a system interacting through a density dependent tumble rate α, one thus has to replace $\alpha(\bar{\rho})$ by $\alpha(\rho(x) + \sigma\Delta\rho)$ in the equations of motion and expand. In practise this will generate many higher order gradients. The only one that interests us here, though, is the first correction term that is linear in the derivative of ρ. Indeed, any terms like $(\Delta\rho)^2$ are of the same order as $\Delta^2\rho$ but only the latter plays a role in analysing the stability of a flat profile. In practise this term is given by

$$-D\frac{\rho(\alpha\tau)'}{1+\alpha\tau}\sigma\Delta^2\rho \tag{6.60}$$

and indeed corresponds to the term introduced phenomenologically in equation (6.54). The value of the parameter κ is thus constrained by the microscopic details of the model:

$$\kappa = D\frac{\rho(\alpha\tau)'}{1+\alpha\tau}\int \mathrm{d}y K(y) y^2 \tag{6.61}$$

Given this mapping, we can, then, determine all the parameters required to describe the behaviour of the system at a mesoscopic level from the microscopic dynamics. To apply these results to real experiments, however, we shall have to add one final feature to our model: population dynamics.

The timescales on which our patterns form are sufficiently long that we cannot neglect the effect of birth and death processes if we wish to accurately characterise their behaviour. Further, experiments are often carried out from a small inoculation in the centre of a plate which then grows outwards to fill a dish forming patterns in the wake of an expanding front. Mimicking this type of

behaviour is impossible without explicitly including cell division.

We therefore turn to this issue in the next chapter and consider how regulated cell division will affect the results we have so far determined.

Chapter 7

Arrested Coarsening: the Effect of Regulated Cell Divison

In chapter 6 we investigated a number of two dimensional models of run-and-tumble bacteria interacting through density dependent motility. We saw that when the collective diffusivity becomes negative, homogeneous systems can become unstable with respect to small stochastic fluctuations and the system can split into regions of high and low bacterial density. In figure 6.8 we saw that these domains coarsen over time, and eventually, for any finite system, we will be left with a single region of high density and a single region of low density—this separation being driven by the need to minimise the interface between the two domains.

If, however, we want to form more complex patterns at steady state, as we see in many real bacterial colonies, this coarsening process will have to be arrested at some point. Some other feature of the dynamics will have to balance the surface tension and fix the domain size at some finite scale, independent of the total system size. To this end, in this chapter, we add to our model a description of the population dynamics. On the timescales on which the coarsening of domains occurs we can no longer ignore the effects of cell division, which, as we shall see, are precisely what is required to arrest the coarsening.

The effect of regulated cell division or the birth and death of bacteria, is to allow the formation of long-lasting patterns. These patterns appear to be robust to the precise form of the interactions and to the method by which "death" is modelled. The precise meaning of this term is discussed in some detail in

section 7.4. Previously Cates et al. [1] showed, using a semi-phenomenological model, that a birth-death process could arrest separation in bacterial colonies and lead to pattern formation. Here I show both that their phenomenological model can naturally arise from a variety of microscopic dynamics and that a regulation of cell division at high densities (with no death) can lead to qualitatively similar results to their model.

The model of a density dependent motility which instigates an instability, which is driven to coarsen by a surface tension before being arrested by cell division is thus shown to provide all the dynamics required for patterning to occur. This simple and generic mechanism, which can arise from a variety of microscopic models, thus provides a null hypothesis for pattern formation in bacterial colonies which has to be falsified before appealing to more elaborate alternatives.

As I described in chapter 2, bacterial colonies are capable of producing quite striking pattern formation [34–41, 85–87]. These patterns can arise from many different microscopic interactions; be they chemotaxis, quorum sensing, steric interactions, competition for food, or even a combination thereof. The simple model we investigate here shows, for differing parameter ranges and initial conditions, the formation of both regular and amorphous dots, concentric rings and discs and regular or amorphous stripes or lamellae.

7.1 Presentation of the Model

Let us consider a population of run-and-tumble bacteria, modelled with finite tumble time as in section 6.4, interacting through some density dependence in one or more of their motility parameters: the swim speed v, the rate to enter a tumbling state α or the rate to start swimming again β (or equivalently the tumble duration $\tau = 1/\beta$).

As we have seen previously, at the end of chapter 6, (and now working explicitly in two spatial dimensions) on time scales longer than $1/\alpha$ and $1/\beta$, but shorter than the cell generation time, this dynamics gives rise to a diffusive behaviour which, to second order in a gradient expansion, can be approximated

mathematically by the equation

$$\dot{\rho}(\mathbf{r}) = \nabla \cdot \left[D_0 \left(1 + \rho \frac{\mathrm{d}}{\mathrm{d}\rho} \log \frac{v}{1+\alpha\tau} \right) \nabla\rho \right]; \qquad D_0 = \frac{v^2}{2\alpha(1+\alpha\tau)}. \tag{7.1}$$

If $v/(1+\alpha\tau)$ is a decreasing function of ρ, the collective diffusivity,

$$D_c = D_0 \left(1 + \rho \frac{\mathrm{d}}{\mathrm{d}\rho} \log \frac{v}{1+\alpha\tau} \right), \tag{7.2}$$

can become negative. In this case any flat profile will be unstable and equation (7.1) leads to infinitely sharp gradients. In reality, higher order terms in the gradient expansion will smoothen these gradients and including these terms we discover an effective surface tension given by $-\kappa\Delta^2\rho$. As described in section 6.6, we can calculate κ from the microscopic dynamics and find that in this case it will be given by

$$\kappa = \frac{D_0 \sigma \rho}{2} \frac{\mathrm{d}}{\mathrm{d}\rho} \log \frac{v}{1+\alpha\tau}. \tag{7.3}$$

Interestingly, it should be noted that the instability requires only that D_c become negative; the bare diffusivity, D_0, can, however, remain constant or even be an increasing function of ρ while the system overall leads to instability and patterning. This highlights the need experimentally for a measure of the collective diffusivity and to go beyond the mean-squared displacement, which would yield only the bare diffusivity D_0.

To illustrate this point, consider choosing the tumble rate and velocity to be given by

$$v = v_0 \exp(-\lambda\rho/2), \qquad \alpha = \frac{-C + \left(C^2 + 2\tau C v^2\right)^{1/2}}{2\tau C}, \tag{7.4}$$

so that the bare diffusivity is constant, $D_0 = C$, and the collective diffusivity is given by

$$D_c = \frac{C^{5/2} \left(-2\sqrt{1 + \frac{2\tau v_0^2 e^{-\lambda\rho}}{C}} - 2 - \frac{4\tau v_0^2 e^{-\lambda\rho}}{C} + \lambda\rho\sqrt{1 + \frac{2\tau v_0^2 e^{-\lambda\rho}}{C}} + \lambda\rho \right) \tau e^{-\lambda\rho} v_0^2}{\left(1 - \sqrt{1 + \frac{2\tau v_0^2 e^{-\lambda\rho}}{C}} \right) \left(1 + \sqrt{1 + \frac{2\tau v_0^2 e^{-\lambda\rho}}{C}} \right)^2 \sqrt{1 + \frac{2\tau v_0^2 \mathrm{e}^{-\lambda\rho}}{C}}}, \tag{7.5}$$

so that λ is some parameter we can then control to change the collective diffusivity

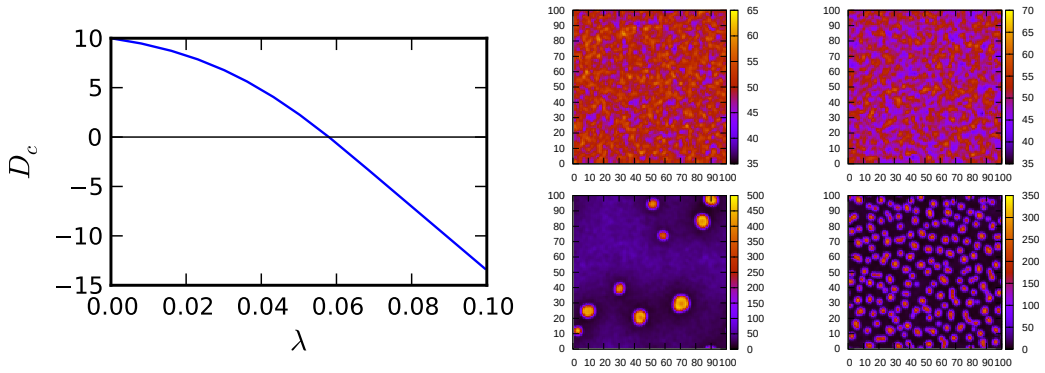

Figure 7.1: **Left**: The collective diffusivity, $D_c(\lambda)$, as a function of λ. Calculated at $\rho = 50$, $C = 10$, $v_0 = 10$, $\tau = 1$. The critical value of λ is $\lambda_c = 0.05798$ (calculated numerically). **Right**: Snapshots of systems with different values of λ either side of λ_c. Top left: $\lambda = 0.02$. Top right: $\lambda = 0.04$. Bottom left: $\lambda = 0.06$. Bottom right: $\lambda = 0.08$. As predicted the bottom two systems are unstable, while the top two remain homogeneous. All simulations recorded at $t = 100$.

from positive to negative. At some critical value of λ, denoted λ_c, the collective diffusivity should become negative and the uniform profile becomes unstable (see figure 7.1).

To measure the collective diffusivity directly, one could, for example, consider the decorrelation of density fluctuations on time scales short than the generation time and extract D_c from the Fourier transform of the Van Hove pair correlation function [88]

$$\langle \delta\rho(\mathbf{q}, t)\delta\rho(-\mathbf{q}, t)\rangle \propto \exp\left[-D_c q^2 t\right]. \tag{7.6}$$

This may be difficult to perform experimentally, but has recently been performed by *Differential Dynamic Microscopy* (DDM) in homogeneous suspensions of bacteria where interactions were minimal [89].

On larger timescales the population dynamics of the bacteria become important, however, and we must explicitly extend our model to include the birth-death dynamics. In section 7.4 we shall consider more specifically what birth-death dynamics are most appropriate for our model and what effect the choice has on our results. For now, let us simply add a logistic growth term to equation (7.1). The full evolution of the density is then given by

$$\dot{\rho} = \nabla \cdot [D_c \nabla \rho] - \mu\rho\left(1 - \frac{\rho}{\rho_0}\right) - \kappa\Delta^2\rho, \tag{7.7}$$

where μ controls the timescale of the population dynamics relative to the motility and ρ_0 sets an average carrying capacity at any given point in space.

Equation (7.7) is exactly that proposed by Cates et al. [1] as a semi-phenomenological description of interacting and dividing run-and-tumble bacteria. Their analysis showed that it could lead to pattern formation and might be a generic mechanism underlying more complex models previously proposed. In this chapter we show that this equation is not artificially created to provide the desired behaviour but can arise from a variety of microscopic models and is robust to changes in the details of such microscopic behaviour.

7.2 Qualitative Behaviour and Simulation Results

Though the analysis in this chapter concerns purely continuum descriptions of the dynamics, and indeed continuum descriptions modelled after a diffusive approximation and without explicit noise, the simulations against which they are compared remain of the stochastic, lattice variety described in previous chapters. As the coarse-grained density $\bar{\rho}$ is determined with an isotropic, Gaussian kernel, we expect, as shown in chapter 6, that the results thus obtained will nevertheless coincide.

We simulate a uniform population of bacteria in a two dimensional box with periodic boundary conditions and choose to implement all interactions in the motility through a tumbling rate given by

$$\alpha[\bar{\rho}(x)] = \alpha_0 \exp[\lambda \bar{\rho}(x)], \tag{7.8}$$

that is a tumbling rate which increases with increasing density and, therefore, produces a diffusion which decreases as density increases. In the simulations we adopt a simple logistic dynamics as in equation (7.7) (and detailed microscopically in section 7.4). The coarse-graining of density is performed using an isotropic Gaussian kernel so that

$$\bar{\rho}(x) = \int \mathrm{d}y \frac{1}{\sqrt{2\sigma\pi}} \exp(-y^2/(2\sigma))\rho(x-y). \tag{7.9}$$

We see an initially uniform suspension of bacteria become unstable and aggregate into high density dots surrounded by a low density background. (Note that changing the parameters of the models, the converse (low density dots against a high density background), or even lamellae, is also possible.) As time increases we see these dots of high density coarsen into larger domains, as we did in section 6.3.

In this model, however, on longer timescales the population dynamics begins to play a significant role, and acts to arrest the coarsening process, resulting in the aggregates of higher density stabilising at a finite size.

To understand the origin of the arrest, consider the flux of bacteria between a high density droplet and its low-density surroundings. The transfer of bacterial mass is given by the flux through the interface. This is proportional to the length of the interface and thus to the radius of the droplet. The variation of the mass in the droplet due to the birth-death process is however proportional to the area of the droplet, and thus to the square of its radius. Balancing the two contributions to guarantee a steady state is thus only achieved for a given radius beyond which the droplets will not coarsen.

Most experiments on patterning in bacterial colonies are performed in soft agar, to prevent convection and maintain steady conditions over long times. This makes considering a uniform initial condition difficult experimentally and most of the interesting patterns have been observed starting from a central inoculum. We therefore ran simulations where a small colony of bacteria starts in the centre of the 2d box. The agar concentration used experimentally is low enough that we can assume it has little impact on the run-and-tumble dynamics [90]. In this case we see an unstructured lawn propagate through the box in a manner reminiscent of a Fisher wave. Once the density in the central part of the lawn rises above a given threshold, determined by λ, a ring is nucleated and the density in its wake drops again. This process occurs repeatedly and results in a sequence of static concentric rings (see figure 7.2). These dynamics are strikingly similar to those observed experimentally for *S. Typhimurium* [36, 38].

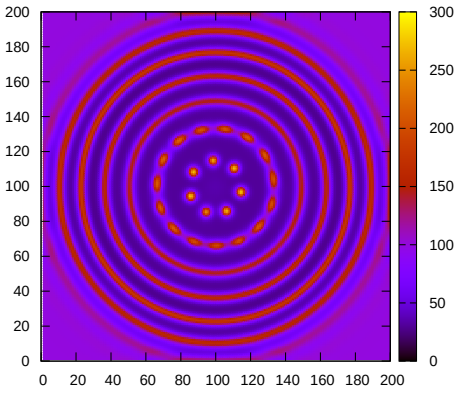

Figure 7.2: A snapshot of the concentric rings formed behind the front when starting from a central inoculum. By altering the parameters of the system the rings can remain stable or be transient eventually breaking into dots, as seen at the centre of this graph. Simulation performed on a lattice of 200×200 sites with the parameters: $v_0 = 3.3$, $\alpha_0 = 1$, $\lambda = 0.037$, $\mu = 0.01$, $\rho_0 = 100$, $\sigma = 2.2$.

7.3 Determining the Phase Diagram from Simulation and Analytics

Let us now try to understand this behaviour analytically and to show that the coarsening is indeed arrested by the birth-death process (and not by some other effect). We will begin by analysing the linear stability of the dynamics and investigate the effect of a small stochastic fluctuation around a flat profile. Following Cates et al. [1] let us consider a perturbation around the fixed point of the logistic term $\rho = \rho_0 + \sum_q \mathrm{e}^{iqx}$. After Fourier transforming, we find that the growth rate Λ_q of each Fourier mode is given by

$$\dot{\delta}\rho_q = \Lambda_q \delta\rho_q; \qquad \Lambda_q = -\mu - q^2 D_c(\rho_0) - \kappa q^4, \tag{7.10}$$

for full details see Cates et al. [1].

If the growth rate Λ_q is positive for any of these modes the system will be unstable and random fluctuations should grow, destroying any uniform flat profile. Conversely, if Λ_q is negative for all q then a profile $\rho(\mathbf{x}) = \rho_0$ will be stable with respect to small fluctuations.

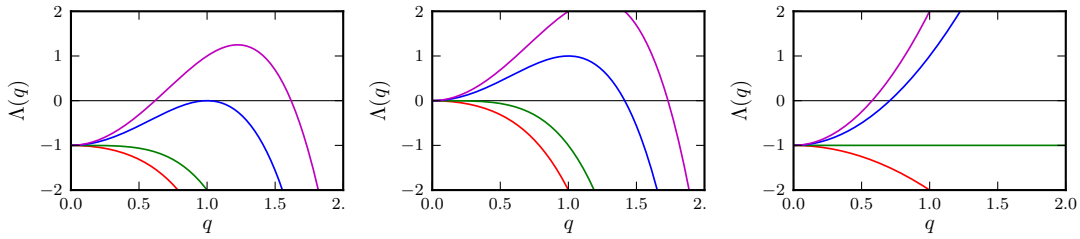

Figure 7.3: **Left**: Characteristic curves for $\Lambda(q)$ in the precense of both stabilising features, growth and surface tension. **Centre**: Curves for $\Lambda(q)$ for the same parameters but without birth and death. **Right**: The same plot of $\Lambda(q)$ with birth and death but for strictly local interactions—that is without any surface tension.

Note that the presence of the logistic term in equation (7.7) now means that, in contrast to the stability analysis we examined in section 6.2, the rate Λ_0 is always strictly negative. The presence of the birth and death terms stabilises the small q modes, and thus sets an upper bound on the length scale for any pattern formation, as we described earlier.

At the other end of the scale, as κ is strictly positive, the surface tension term in equation (7.7) stabilises large q modes. We thus see a characteristic length scale emerge from the linear stability analysis and any instability in the dynamics will lead to the formation of finitely sized domains, exactly as we require for steady state pattern formation. In figure 7.3 we can see examples of characteristic curves for Λ_q as a function of q with and without the stabilising features of the dynamics. Without the surface tension no coarsening occurs as the largest eigenvector occurs for $q \to \infty$, as seen in figure 7.3.

By determining under what conditions equation (7.10) can be solved for $\Lambda_q > 0$, we can then determine criteria on the microscopic parameters for ρ_0 to be unstable. Those criteria read

$$\frac{1}{\rho_0} < -\frac{\mathrm{d}}{\mathrm{d}\rho}\left(\log\frac{v}{1+\alpha\tau}\right); \quad \frac{-v^2}{2\alpha(1+\alpha\tau)}\left(1+\frac{\mathrm{d}}{\mathrm{d}\rho}\left(\log\frac{v}{1+\alpha\tau}\right)\rho_0\right) > 2\sqrt{\mu\kappa} \tag{7.11}$$

Recalling from section 6.6 that we can express κ in terms of the microscopic parameters as

$$\kappa = \sigma\rho\frac{v^2}{2\alpha(1+\alpha\tau)}\frac{\mathrm{d}}{\mathrm{d}\rho}\left(\log\frac{v}{1+\alpha\tau}\right) \tag{7.12}$$

we can therefore express our criteria for the stability or otherwise of ρ_0 purely in

terms of the microscopic parameters that enter into our simulations.

This formulation of the criteria allows us to easily determine whether, for any set of microscopic parameters, a given system will be unstable to fluctuations around the carrying capacity ρ_0. To compare with the results of Cates et al. [1], however, let choose a set of microscopic motility parameters that lead to the same diffusivity as they consider. Specifically let us take $v(\rho) = v_0 \exp(-\lambda\rho/2)$, $\alpha(\rho) = \alpha_0$ and $\tau(\rho) = \tau_0$ so that the collective diffusivity is given by

$$D_c = \frac{v_0^2}{2\alpha_0(1+\alpha_0\tau_0)} e^{-\lambda\rho}\left(1 - \frac{\rho\lambda}{2}\right). \tag{7.13}$$

Let us further simplify, non-dimensionalising the equations by replacing

$$t' = \mu t; \qquad \mathbf{x}' = \mathbf{x}\left(\frac{\mu}{\kappa}\right)^{1/4}; \qquad u = \frac{\rho}{\rho_0}, \tag{7.14}$$

and defining the new parameters R and Φ via

$$R = \frac{v_0^2}{2\alpha_0(1+\alpha_0\tau_0)\sqrt{\mu\kappa}}; \qquad \Phi = \frac{\lambda\rho_0}{2}. \tag{7.15}$$

In terms of these parameters the stability criteria are given by

$$\Phi \geq 1; \qquad R \geq R_c = 2\frac{\exp(2\Phi)}{\Phi - 1}, \tag{7.16}$$

and the resulting phase diagram, as reported by Cates et al. [1], is shown in figure 7.4.

In addition to calculating the phase diagram analytically, however, we can also run simulations. This allows us a method to check the mapping derived in section 6.6. If our mapping is accurate, and we can calculate the mesoscopic parameters R and Φ from the microscopic ones, we should be able to determine precisely where we are in the phase diagram for any particular simulation.

To check the mapping I thus ran 90 simulations for different values of R and Φ (6 different values of R for Φ in steps of 0.1 from 1.1 to 2.5). For each simulation I chose values of R on either side of the predicted transition line and recorded the qualitative pattern (or lack of pattern) observed. In each simulation I held $\rho_0 = 40$, $v_0 = 10$, $\alpha_0 = 1$ and $\sigma = 1.5$ constant. I then changed the growth rate μ and interaction strength λ to alter the two parameters R and Φ.

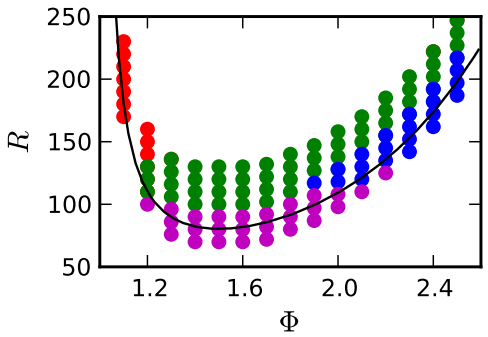

Figure 7.4: The phase diagram for the arrested phase separation. The black line marks the theoretical boundary as determined by Cates [1]—above the line the system is unstable and will separate, below the line the system will remain homogeneous. The points mark the results of simulations of my lattice-based code. Pink circles denote no separation, blue denote lamellae, green denote amorphous dots of high density against a low density background and red denote regular dots.

In figure 7.4 I therefore include not only the analytic lines, but also the computational data for the phase diagram, which reveal a remarkable overlap, despite the approximations that were required in moving from lattice simulations to continuum equations, in taking a diffusive limit and in coarse-graining the non-locality of the interactions.

Cates et al. [1] calculated (via an amplitude equation, detailed in the supplementary information of their paper) that in the range $1.08 \leq \Phi \leq 1.58$ the transition is supercritical (continuous), while outside this range the transition is subcritical. In the subcritical case there may be nucleation type events which could lead to separation and pattern formation due to fluctuations prior to crossing the transition line, as we see in figure 7.4. The results are, however, broadly in quantitative agreement and those discrepancies we do see fit easily within our analytic understanding of how the diagram should appear.

This level of analysis tells us only whether a uniform flat profile in a particular parameter range is unstable or not, however; not the steady state pattern that would then be formed. For that detail we would need to go beyond a linear stability analysis to address the amplitude equation for each possible pattern. In this work we instead look qualitatively at our simulations across a range of parameters and observe a variety of pattern forms—droplets of high density in a sea of low density, inverted droplets of low density against a high

density background and lamellae, interspersed strips of high and low density. Interestingly, these generally random and irregular lamina can even be regularised into evenly spaced stripes by breaking the underlying dynamical symmetry and adding a drift in one direction (see figure 7.5).

We see then a variety of patterns which can be formed by this relatively simple microscopic model, and which can arise from a variety of microscopic interactions—through the tumble rate, tumble duration or velocity—so long as certain conditions are met. One might be concerned, however, at the somewhat arbitrary nature of manner in which the birth-death process was added to the model and to what extent it could affect our results. We turn, then, to consider more carefully what we mean by death in the context of these models and how precisely to model it.

7.4 What do we mean by "Death": a Comparison of Different Methods to Limit Growth

"Death", for bacteria, is not a simple, spontaneous act, easy to capture in a mathematical model or simulation, but a slow, complex process that happens in stages. Bacteria progressively stop swimming and dividing, but can still be recovered by being placed in a more advantageous environment, (i.e. where there is more nutrient) then eventually die, (i.e. cannot be recovered) and finally undergo lysis [91, 92]. In our simple logistic model we should thus consider that "death" is simply the bacteria leaving the standard run-and-tumble-and-divide dynamics, but the question arises: should we record each stage as a separate population?

To some extent our answer may depend on the type of interactions we want to model—for steric interactions, immobile, non-reproducing bacteria will still take up space and block mobile bacteria—for chemical signalling, they may not interact in any significant way with the still active bacteria. We may have a situation where we must replace a velocity which depends on density via the exchange $v(\rho) \to v(\rho_{active}, \rho_{inactive})$ or via $v(\rho) \to v(\rho_{active})$. In the latter $\rho_{inactive}$ disconnects from the evolution of the active population and can be neglected if all we are concerned about is the number of active bacteria. (If we wish to know the total number of bacteria for some reason, to compare with observed experimental

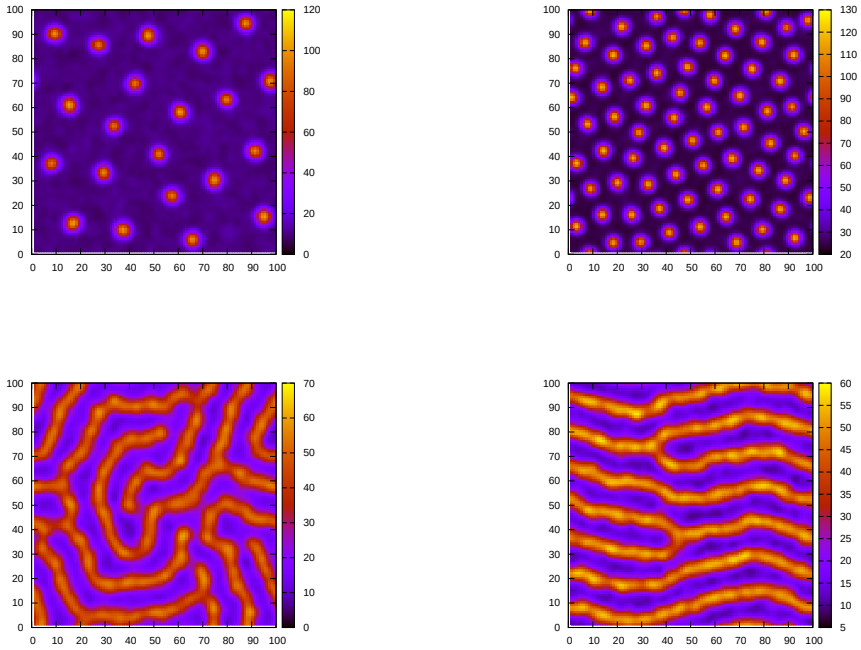

Figure 7.5: Snapshots of a variety of patterns which can be formed by the mechanism of an instability instigated by density dependent motility, arrested by logistic growth. **Top Left**: amorphous droplets of high density against a low density background ($v_0 = 10$, $\lambda = 0.09$, $\alpha_0 = 1$, $\mu = 0.0338$, $\rho_0 = 40$, $\sigma = 1.5$). **Top Right**: regular droplets of high density against a low density background ($v_0 = 10$, $\lambda = 0.06$, $\alpha_0 = 1$, $\mu = 0.1$, $\rho_0 = 50$, $\sigma = 1$). **Bottom Left**: amorphous lamina of high and low density ($v_0 = 10$, $\lambda = 0.11$, $\alpha_0 = 1$, $\mu = 0.1354$, $\rho_0 = 40$, $\sigma = 1.5$). **Bottom Right**: regularised lamina - with the same parameters as the bottom left, but with an added drift towards the right of the graph (we replace $v(\rho) = v_0 \exp(-\lambda\rho)$ with $v(\rho, \theta) = v_0(1 + 0.2\cos(\theta))\exp(-\lambda\rho)$, where θ is the angle between the direction in which the bacteria is moving and the horizontal).

evidence, for example, we must of course record the inactive population as well.) The question becomes clouded still further if we allow that the bacteria may still be motile, and indeed interacting, but no longer dividing. In this case our logistic growth model may need closer examination. Do the non-reproducing motile bacteria count towards the carrying capacity to the same extent, for example?

Indeed, more broadly, should the growth be treated as logistic at all? What does that mean microscopically? The logistic term, unlike the diffusion an drift terms, did not arise in equation (7.7) from coarse-graining or averaging microscopic behaviour but was added phenomenologically after the continuum, diffusive approximation was performed. How, then, do we back that into the microscopic dynamics?

Generally, to model logistic growth microscopically, one can consider the reactions $A \to A + A$ occurring with some rate $a + b\rho$ and $A \to \varnothing$ with a rate $c + d\rho$ (where a, b, c and d are some arbitrary constants and A denotes a single particle). What, then, do we take for the four constants? In most of the simulations presented in this thesis I take $b = c = 0$, i.e a constant per particle birth rate independent of local density and a "death" rate which increases as density increases. To check whether this choice of parameters affects the results qualitatively let us consider some other possible rates. One significantly different choice could be to eliminate death entirely and simply have a growth rate which decreases as density increases and food becomes relatively scarcer; we would then take $c = d = 0$ and $b < 0$. This would imply that $\rho = \rho_0$ is no longer a stable fixed point from above—that is $\rho = \rho_0$ is still a solution to the deterministic dynamics but is not stable to fluctuations increasing ρ—and, as such, we might therefore expect to see qualitatively different results in the simulations.

Pushing the boundaries even further, we could eliminate any fixed point entirely and replace the logistic growth with a decreasing growth rate which never reaches zero, whilst still removing death. We could, for example, take the growth rate to be proportional to $\exp(-\rho/\rho_0)$. In this case there is no fixed carrying capacity and growth will continue indefinitely. Note that this is not presented as a realistic choice, but represents an extreme implementation of the population dynamics where we might expect our previous results to break down.

In fact, when we run simulations with both these choices for the population dynamics we still see patterns form, albeit on a strictly transient basis (see

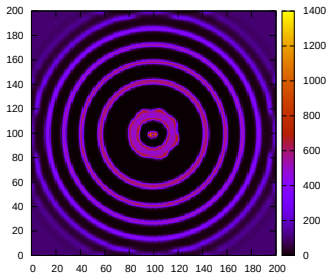

Figure 7.6: A snapshot of rings formed from growth of an initial inoculum in the centre of the graph for a system with no death. There is a slight broadening of the central ring, but otherwise the pattern is qualitatively the same as the rings seen in figure 7.5. The simulation is performed on a lattice of 200×200 sites with parameters: $\alpha_0 = 1$, $v_0 = 3.3$, $\lambda = 0.037$, $\sigma = 2.19$, with growth rate obeying $\mu(\rho) = 0.01 \exp(-\rho/100)$.

figure 7.6). Eventually the rings would coarsen and the gaps between them would be filled in. In a real system the dead bacteria would also undergo Brownian diffusion, again leading to a coarsening over time of the rings. The time taken to see such effects however is far beyond that of the simulations or experiments (an immotile bacteria would take several months to diffuse the width of one of the rings, which is around $2mm$).

To understand why we still see ring formation and regions of very low density even at relatively late times (as compared to the spread of the colony), consider an inoculum of bacteria growing from a very low density. As the density of bacteria passes through the instability formed by the interaction (which we can now no longer calculate analytically as there is no fixed point around which to expand our stability analysis but which still exists as the interaction term has not changed) the population separates into high and low density regions. As there is no death, the density of the high density regions is now no longer fixed and continues to rise. Both the growth and dynamics are exponentially damped; however, this increase, in absolute density and in spatial extent, is extremely slow. Over the characteristic timescales on which the colony as a whole expands and the patterns initialise, we see very little difference between this quite extreme population dynamics and the more analytically tractable and perhaps realistic logistic birth-death process. Our results seem, therefore, to be resistant

to changes in the method used to model the population dynamics so long as the net rate of growth per bacterium—taking into account any "death"—decreases with increasing density. Overall it appears that the mechanism that hinders the coarsening is the saturation of the birth term and not the existence of a stable fixed point. We can be confident that, though there is debate as to the precise microscopic dynamics, the resolution of this debate is not essential to our results and indeed our mechanism for patterning is quite general.

Beyond the various modifications to the microscopic dynamics we have considered, there is, however, one important difference between real experimental systems [14, 20, 28, 90, 93] and our models. In chapter 3 we considered the coarse-graining of the density to account for dependence of the motility on the density in some region around the bacteria. We said then that to be strictly accurate we should include time delays when considering, for example the interactions to be mediated by some chemical components. Explicitly adding these external fields to our simulations is possible, but would simply return us to the same complex description already present in the literature [23, 37, 38, 40, 94, 95] and that we wanted to avoid.

Chapter 8

Multiple Species Models

Until this point we have considered only systems in which we have a single species and type of bacteria growing and interacting. In most real world situations, however, living organisms will not exist in a state of isolation but in an environment in which many agents of different forms interact, whether through competition for resources, predation or some other form of competitive or collaborative interaction. To understand the origins and role of cooperation, competition and biodiversity we need to consider multiple types of particles at once.

One common method to study such systems in recent years has been evolutionary game theory—particularly for the study of cyclic competition between species, where, for example, species A has some advantage over species B, B an advantage over C and C an advantage over A. These simple systems can reveal quite complex behaviour for the emergence of co-existence and extinction of species and both spatial and temporal pattern formation. Though in this chapter we consider only the situation of neutral evolution, where no species has an inherent fitness advantage, the interested reader is recommended the review by Frey [96] for an overview of the evolutionary game theory concept and application to microbial colony dynamics.

Even in systems that are neutral with respect to fitness, and in fact in systems with purely diffusive motility (without predation, kinesis, taxis or environmental variability) stochastic birth and death processes can lead to clustering and patterns [97]. The inherent irreversibility of the birth-death process at a microscopic level—where death can occur anywhere, but birth only where there

are already parent organisms—means that even if the steady-state of a system is uniform on average, in particular realisations clustering can occur and species can become dissociated—that is separate into regions of only one species or the other—purely through the effect of random fluctuations.

Here we consider both the effects of these random fluctuations and more direct interactions between species of bacteria. Specifically we introduce a model of multiple, interacting "species" of bacteria and consider the case first where bacteria can switch stochastically between species (to model for example some genetic switch which alters growth or motility) and then the case of completely distinct species. We will examine the limiting case where the type switching model can be solved analytically, and investigate approaches to solving it more generally. A related model of swarming and swimming *Proteus mirabilis* colonies is developed and compared to the existing literature. Finally, competition between multiple species of bacteria eating the same food source is considered and the potential for pattern formation in such a system is analysed.

8.1 Presentation of the Two Type Model

Consider two type of particles, for simplicity of notation initially in one dimension, potentially with different dynamics and with transmutation between type. Each type can then be in either a left or a right moving state. Each particle can switch from left to right moving and vice versa at rates $\alpha_{L/R}$, from type S to F, denoting, say, a slower and a faster type, at rates $\beta_{SL/R}$ and from F to S at rates $\beta_{FL/R}$. The evolution of the probabilities to find a particle in a given state, left or right moving, type F or S, at some position x at time t is then given by

$$\begin{aligned}
\dot{F}_R &= -\nabla\left(v_{FR}\,F_R\right) - \frac{\alpha_{FR}\,F_R}{2} + \frac{\alpha_{FL}\,F_L}{2} - \beta_{FR}\,F_R + \beta_{SR}\,S_R \\
\dot{F}_L &= \nabla\left(v_{FL}\,F_L\right) + \frac{\alpha_{FR}\,F_R}{2} - \frac{\alpha_{FL}\,F_L}{2} - \beta_{FL}\,F_L + \beta_{SL}\,S_L \\
\dot{S}_R &= -\nabla\left(v_{SR}\,S_R\right) - \frac{\alpha_{SR}\,S_R}{2} + \frac{\alpha_{SL}\,S_L}{2} + \beta_{FR}\,F_R - \beta_{SR}\,S_R \\
\dot{S}_L &= \nabla\left(v_{SL}\,S_L\right) + \frac{\alpha_{SR}\,S_R}{2} - \frac{\alpha_{SL}\,S_L}{2} + \beta_{FL}\,F_L - \beta_{SL}\,S_L.
\end{aligned} \tag{8.1}$$

For the moment let us take all rates to be symmetric between left and right movement and change variables to

$$\begin{aligned} F &= F_R + F_L & S &= S_R + S_L \\ J_F &= v_F(F_R - F_L) & J_S &= v_S(S_R - S_L). \end{aligned} \tag{8.2}$$

Then our equations become

$$\begin{aligned} \dot{F} &= -\nabla J_F - \beta_F F + \beta_S S \\ \dot{S} &= -\nabla J_S + \beta_F F - \beta_S S \\ \dot{J}_F &= v_F \left(-\nabla (v_F F) - (\alpha + \beta_F)\frac{J_F}{v_F} + \beta_S \frac{J_S}{v_S} \right) \\ \dot{J}_S &= v_S \left(-\nabla (v_S S) - (\alpha + \beta_S)\frac{J_S}{v_S} + \beta_F \frac{J_F}{v_F} \right). \end{aligned} \tag{8.3}$$

Taking the diffusive limits $\dot{J}_F = 0$ and $\dot{J}_S = 0$ but $\dot{F} \neq 0$ and $\dot{S} \neq 0$, i.e. where $\alpha \gg \beta_{F/S}$ so the type switching occurs on a much longer timescale than the run-and-tumble behaviour, leaves us with two equations for the diffusion and reaction of two types of particles, F and S:

$$\begin{aligned} \dot{F} &= -\nabla \left[\frac{-v_F}{\alpha(\alpha + \beta_F + \beta_S)} \left(\beta_S \nabla (v_S S) + (\alpha + \beta_S) \nabla (v_F F) \right) \right] - \beta_F F + \beta_S S \\ \dot{S} &= -\nabla \left[\frac{-v_S}{\alpha(\alpha + \beta_F + \beta_S)} \left(\beta_F \nabla (v_F F) + (\alpha + \beta_F) \nabla (v_S S) \right) \right] + \beta_F F - \beta_S S. \end{aligned} \tag{8.4}$$

8.1.1 Stopped Limit

Equations (8.4) are, in general, not easy to solve, even at steady state. There is, however, one limit we can immediately consider in which the dynamics become considerably more simple. In section 6.4 we examined bacteria which took a finite time to tumble. In this case we had, in effect, multiple alternating "types" of bacteria: a swimming type and a tumbling type. If we now take the limit where the speed of the S particles, v_S, equals zero, we approach a qualitatively similar, though not identical, situation. In this case, as for the finite tumble problem considered previously, progress is more tractable. The evolutions of $F(x,t)$ and

$S(x,t)$ now reduce to

$$\begin{aligned}\dot{F} &= -\nabla\left[\frac{-v_F}{\alpha(\alpha+\beta_F+\beta_S)}(\alpha+\beta_S)\nabla\left(v_F\,F\right)\right]-\beta_F\,F+\beta_S\,S\\ \dot{S} &= \beta_F\,F-\beta_S\,S.\end{aligned} \tag{8.5}$$

The steady state of these equations is then easy to calculate and is given by

$$\begin{aligned}S(x) &= \frac{\beta_F}{\beta_S}F(x)\\ F(x) &\propto \frac{1}{v_F(x)}.\end{aligned} \tag{8.6}$$

That is we find that in this limit the distribution of F particles is unchanged from their distribution in the absence of a switching interaction and functionally depends only on their velocity. The switching interaction acts only to control the relative number of fast and slow particles and so as an overall normalisation on the distribution of F particles.

8.2 Switching interaction

Let's now consider the case where one of the switching rates, say β_S—the S to F rate—depends on the local density of particles. For simplicity we'll take $\beta_S(S)$ and not $\beta_S(S,F)$, though, in the absence of other interactions the behaviour would be similar. All other rates are constant and homogeneous. In the $v_S = 0$ case, then, at steady state $F(x)$ must be constant and independent of position—$F(x)$ is proportional to $1/v_F(x)$, which is constant as we are considering the only interaction or inhomogeneity to be in β_S. $S(x)$, however, need not be. If we take, for example, our standard form of interaction

$$\beta_S(S) = \exp(-\lambda\phi\arctan(S/\phi)), \tag{8.7}$$

where the switching rate decreases as density increases but stops at a finite value, never entirely stopping, then we have

$$S\,\exp(-\lambda\phi\arctan(S/\phi)) = \beta_F\,F \equiv \text{constant},$$

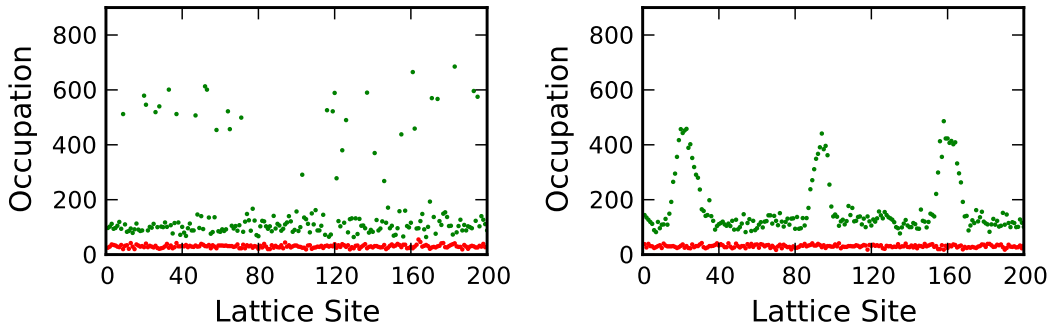

Figure 8.1: **Left:** A snapshot of the lattice system with parameters $\alpha = 1$, $v_S = 0$, $v_F = 10$, $\beta_F = 1$, $\lambda = 0.01$, $\phi = 250$ and $\langle n \rangle = 200$. f type particle occupations are shown in red, s type particles in green. **Right:** A snapshot of the lattice system with the same parameters except with $v_S = 0.1$.

which, for certain values of β_F and F may have more than one solution. Hence, S can show separation into different densities. On lattice this manifests as a constant, flat background of F particles and isolated sites of high densities of S particles, with lower densities of S particles on other sites, see figure 8.1 (left).

If we now restore v_S to be non-zero and run the simulations again we once more see separation into high and low densities of S particles, but now with extended domains of high density, figure 8.1 (right).

For the stopped limit we can, however, go further and calculate the full probability distribution for a given site to have s particles of type S and f of type F. Treating the problem as a zero range process and considering the case where both switching rates and the jump rate for the F particles can depend on the local density at the departure site, then the master equation is

$$\begin{aligned}\frac{\mathrm{d}P(\{s_i, f_i\})}{\mathrm{d}t} = \sum_{i=1}^{L} \Big[& u_{F_{i-1}}(s_{i-1}, f_{i-1}+1) P(\ldots, s_{i-1}, f_{i-1}+1, s_i, f_i - 1, \ldots) \\ & + u_{F_i}(s_i, f_i + 1) P(\ldots, s_{i-1}, f_{i-1} - 1, s_i, f_i + 1, \ldots) \\ & + B_{S_i}(s_i + 1, f_i - 1) P(\ldots, s_i + 1, f_i - 1, \ldots) \\ & + B_{F_i}(s_i - 1, f_i + 1) P(\ldots, s_i - 1, f_i + 1, \ldots) \\ & - \left(B_{S_i}(s_i, f_i) + B_{F_i}(s_i, f_i) + 2\, u_{F_i}(s_i, f_i)\right) P(\ldots, s_{i-1}, f_{i-1}, s_i, f_i \ldots) \Big] ,\end{aligned} \tag{8.8}$$

where $u^F(s, f)$, $B^F(s, f)$ and $B^S(s, f)$ are the per site rates. We now look for steady state solutions and assume the probability of a given configuration can be

written in the factorised form

$$P(\{s_i, f_i\}) = \frac{1}{Z}\prod_{i=1}^{L} g_i(s_i, f_i). \tag{8.9}$$

Balancing the fluxes at each site for particles jumping between sites and changing from one type to the other we arrive at the conditions

$$\begin{aligned} u_{F_{i-1}}(s_{i-1}, f_{i-1}+1)g_{i-1}(s_{i-1}, f_{i-1}+1)g_i(s_i, f_i-1) &= u_{F_i}(s_i, f_i)g_i(s_i, f_i)g_{i-1}(s_{i-1}f_{i-1}) \\ B_{F_i}(s_i, f_i)g_i(s_{,i}\,, f_i) &= B_{S_i}(s_i+1, f_i-1)g_i(s_i+1, f_i-1). \end{aligned} \tag{8.10}$$

The first of these can be rewritten as

$$g_i(s_i, f_i) = \frac{g_i(s_i, f_i-1)}{u_F(s_i, f_i)}, \tag{8.11}$$

and, hence, the probability of a given configuration can be written as

$$P(\{s_i, f_i\}) = \frac{1}{Z}\prod_{i=1}^{L}\prod_{j=1}^{s_i}\frac{B_F(s_i-j, f_i+j)}{B_S(s_i+1-j, f_i-1+j)}\prod_{k=1}^{s_i+f_i}\frac{1}{u_F(0,k)}, \tag{8.12}$$

where without loss of generality we have taken $g(0,0) = 0$ and the normalisation factor, Z, is chosen such that $\sum_{\{s_i,f_i\}} P(\{s_i, f_i\}) = 1$. Switching, then, to a grand canonical ensemble, and introducing a chemical potential, μ, to fix the total number of particles $N = \sum_{i=1}^{L} s_i + f_i$, we can write the partition function, $\mathcal{Z}$, as

$$\mathcal{Z} = \sum_{s_i,f_i} e^{\sum_{i=1}^{L}\left(\left[\sum_{j=1}^{s_i}(\ln(B_F(s_i-j,f_i+j))-\ln(B_S(s_i-j+1,f_i+j-1)))-\sum_{k=1}^{s_i+f_i}\ln(u_F(0,k))\right]+\mu\,(s_i+f_i)\right)}. \tag{8.13}$$

For a homogeneous set of transition rates the probability for a given site to have s particles of type S and f particles of type F is then given by

$$p(s, f|\mu) = \frac{1}{\mathcal{Z}(\mu)}e^{\left[\sum_{j=1}^{s}(\ln(B_F(s-j,f+j))-\ln(B_S(s-j+1,f+j-1)))-\sum_{k=1}^{s+f}\ln(u_F(0,k))\right]+\mu\,(s+f)}. \tag{8.14}$$

For an S to F switching interaction as in equation (8.7), a constant F to S rate, and constant jump rate per particle, the distribution is shown in figure 8.2.

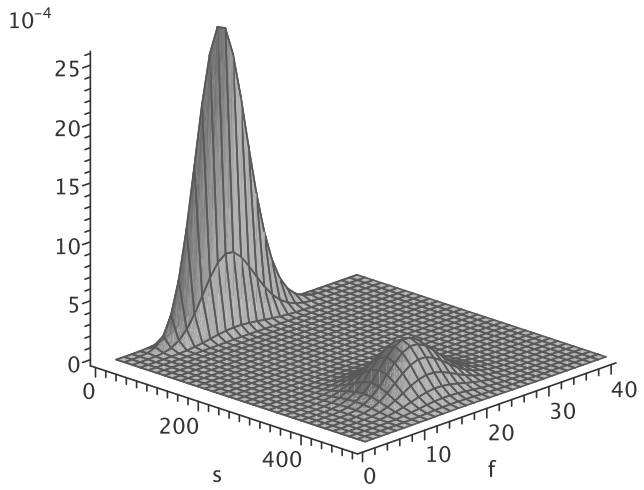

Figure 8.2: The probability distribution for a site to have s S particles and f F particles for rates $u_F(s,f) = 10\,f$, $B_F(s,f) = f$, $B_S(s,f) = s\exp\left(-2.5\arctan\left(\frac{s}{250}\right)\right)$ and an average density of $\langle n\rangle = 200$.

8.2.1 Stability Analysis

To understand this instability better let us linearise equations (8.4) around a flat profile and Fourier transform. We will take

$$\begin{aligned} F &= f_0 + \sum_q \delta f_q \, \exp(-i\, q\, x) \\ S &= s_0 + \sum_q \delta s_q \, \exp(-i\, q\, x), \end{aligned} \tag{8.15}$$

which lead to the matrix equation $\dot{\mathbf{P}}_q = \Lambda_q \mathbf{P}_q$, where $\mathbf{P}_q = \begin{pmatrix} \delta f_q \\ \delta s_q \end{pmatrix}$ and

$$\Lambda_q = \begin{pmatrix} \frac{-v_F\, v_F}{\bar{\alpha}}(\alpha + \beta_S(s_0))q^2 - \beta_F & \frac{-v_F\, v_S}{\bar{\alpha}}\beta_S(s_0)q^2 + \beta_S(s_0) + \beta_S'(s_0)s_0 \\ \frac{-v_S\, v_F}{\bar{\alpha}}\beta_F q^2 + \beta_F & \frac{-v_S\, v_S}{\bar{\alpha}}(\alpha + \beta_F)q^2 - \beta_S(s_0) - \beta_S'(s_0)s_0 \end{pmatrix}, \tag{8.16}$$

where β_S' denotes the derivative of $\beta_S(s)$ with respect to s and $\bar{\alpha} = \alpha(\alpha + \beta_F + \beta_S(s_0))$. The flat profile will be stable if the eigenvalues of Λ_q are negative for all q. For $q = 0$ the eigenvalues of Λ_0 are

$$\lambda^{(1)} = 0 \qquad \text{and} \qquad \lambda^{(2)} = -\beta_S(s_0) - \beta_S'(s_0)\, s_0 - \beta_F.$$

Thus the condition for the $q = 0$ mode to be unstable is $\beta_S' \leq -\frac{\beta_S + \beta_F}{s}$. For $q \neq 0$ we can look for the eigenvalues crossing zero for some value of q and find that there is a crossing if

$$\beta_S'(s_0) \leq -\frac{\alpha\beta_S\,(s_0) + \frac{v_S^2}{v_F^2}\alpha\beta_F + \frac{v_S^2}{v_F^2}{\beta_F}^2 + (\beta_S\,(s_0))^2 + 2\beta_F\frac{v_S}{v_F}\beta_S\,(s_0) + \frac{v_S^2}{v_F^2}q^2}{\left(\alpha + \beta_F\frac{v_S}{v_F} + \beta_S\,(s_0)\right) s_0}. \tag{8.17}$$

In the $v_S = 0$ limit this reduces to the condition $\beta_S'(s_0) \leq -\frac{\beta_S(s_0)}{s_0}$. The stability analysis also predicts that at large enough v_S a flat profile will become stable for any density. By solving (8.17) for v_S for the marginal case where the inequality becomes equality we obtain a maximum value for v_S for any given density, as plotted in figure 8.3.

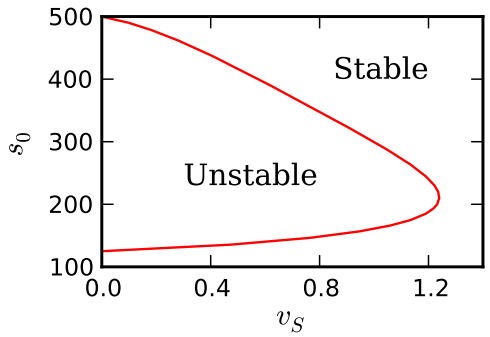

Figure 8.3: The density of S particles, s_0, for which a flat profile will be unstable as a function of v_S. Within the area bounded by the curve the system is unstable and outwith stable. Other parameters are $v_F = 10$, $\alpha = 1$, $\beta = 1$, $\lambda = 0.01$, $\phi = 250$.

8.3 Perturbation Analysis

To move beyond the stability analysis, and to determine something about the steady state distribution for the $v_S \neq 0$ case, let us take a perturbative approach to the problem. We know what the steady state for the $v_S = 0$ case looks like, so perhaps we can expand around this in some form for small but non-zero v_S.

Starting from the basic equations for multiple type run-and-tumble, (8.1), let us look at the isotropic case where $v_S/v_F \ll 1$; here we might possibly be able to perturbatively expand around the solvable limit of one type being immotile, i.e. $v_S = 0$. We define the densities of F and S particles as a series in $v_S/v_F \equiv \epsilon$:

$$\begin{aligned} F_R &= F_{R0} + \epsilon\, F_{R1} + \epsilon^2\, F_{R2} + \dots \\ F_L &= F_{L0} + \epsilon\, F_{L1} + \epsilon^2\, F_{L2} + \dots \\ S_R &= S_{R0} + \epsilon\, S_{R1} + \epsilon^2\, S_{R2} + \dots \\ S_L &= S_{L0} + \epsilon\, S_{L1} + \epsilon^2\, S_{L2} + \dots \end{aligned} \tag{8.18}$$

We define the total number of fast and slow particles at a given position, S and F, and the currents, J_S and J_F, similarly. To zeroth order, the system is identical to the $v_S = 0$ limit, so, for the case considered before of $\beta_S = \beta_S(x)$ and all other

rates constant, we can immediately write down that at steady state

$$\begin{aligned} F_{0R} &= \frac{F_0}{2} = F_{0L} \\ S_{0R} &= \frac{\beta_F F_0}{2\,\beta_S} = S_{0L} \equiv \frac{S_0}{2}. \end{aligned} \tag{8.19}$$

At first order in ϵ we have

$$\begin{aligned} \dot{F}_{1R} &= -v_F\,\nabla\left(F_{1R}\right) - \frac{\alpha\,F_{1R}}{2} + \frac{\alpha\,F_{1L}}{2} - \beta_F\,F_{1R} + \beta_S\,S_{1R} \\ \dot{F}_{1L} &= v_F\,\nabla\left(F_{1L}\right) + \frac{\alpha\,F_{1R}}{2} - \frac{\alpha\,F_{1L}}{2} - \beta_F\,F_{1L} + \beta_S\,S_{1L} \\ \dot{S}_{1R} &= -\frac{v_F}{2}\,\nabla\left(S_0\right) - \frac{\alpha\,S_{1R}}{2} + \frac{\alpha\,S_{1L}}{2} + \beta_F\,F_{1R} - \beta_S\,S_{1R} \\ \dot{S}_{1L} &= \frac{v_F}{2}\,\nabla\left(S_0\right) + \frac{\alpha\,S_{1R}}{2} - \frac{\alpha\,S_{1L}}{2} + \beta_F\,F_{1L} - \beta_S\,S_{1L}. \end{aligned} \tag{8.20}$$

At steady state $\dot{S}_1 = \dot{S}_{1R} + \dot{S}_{1L} = 0$ and $\dot{F}_1 = \dot{F}_{1R} + \dot{F}_{1L} = 0$ which imply that

$$0 = \beta_F\,F_1 - \beta_S\,S_1 \qquad \text{and} \qquad 0 = -\nabla J_1^F. \tag{8.21}$$

Then defining $\sigma_n^{F/S} = F/S_n^R - F/S_n^L$ and taking the differences between the equations for left and right movers for each type we have

$$\begin{aligned} 0 &= -\nabla S_0 - (\alpha + \beta_S)\sigma_1^S + \sigma_1^F \\ 0 &= -v_F \nabla F_1 - (\alpha + \beta_F)\sigma_1^F + \sigma_1^S. \end{aligned} \tag{8.22}$$

Now, if we look for states with no overall current for either fast or slow particles when considered on their own, i.e. where $\int J^{S/F}(x)\mathrm{d}x = 0$, then we can take $J^{S/F} = v^{S/F}\left(\sigma_0^{S/F} + \epsilon\,\sigma_1^{S/F} + \epsilon^2\,\sigma_2^{S/F} + \dots\right)$ so that to first order in ϵ

$$\begin{aligned} J_S &= -v_F\,\epsilon\,\frac{v_F\,\epsilon\,\nabla S_0}{\alpha + \beta_S} \\ J_F &= 0 \\ F &= F_0 + \epsilon \int -\frac{\beta_S}{v_F\,(\alpha + \beta_S)}\nabla S_0 \\ S &= \frac{F_0\,\beta_F}{\beta_S} + \epsilon\,\frac{\beta_F}{\beta_S}\int -\frac{\beta_S}{v_F\,(\alpha + \beta_S)}\nabla S_0. \end{aligned} \tag{8.23}$$

At second order in ϵ

$$\begin{aligned}
\dot{F}_{2R} &= -v_F \nabla (F_{2R}) - \frac{\alpha F_{2R}}{2} + \frac{\alpha F_{2L}}{2} - \beta_F F_{2R} + \beta_S S_{2R} \\
\dot{F}_{2L} &= v_F \nabla (F_{2L}) + \frac{\alpha F_{2R}}{2} - \frac{\alpha F_{2L}}{2} - \beta_F F_{2L} + \beta_S S_{2L} \\
\dot{S}_{2R} &= -v_F \nabla (S_{1R}) - \frac{\alpha S_{2R}}{2} + \frac{\alpha S_{2L}}{2} + \beta_F F_{2R} - \beta_S S_{2R} \\
\dot{S}_{2L} &= v_F \nabla (S_{1L}) + \frac{\alpha S_{2R}}{2} - \frac{\alpha S_{2L}}{2} + \beta_F F_{2L} - \beta_S S_{2L},
\end{aligned} \tag{8.24}$$

which imply that

$$\begin{aligned}
-v_F \nabla \sigma_2^F - \beta_F F_2 + \beta_S S_2 = 0 \\
v_F \nabla - \sigma_1^S + \beta_F F_2 - \beta_S S_2 = 0.
\end{aligned} \tag{8.25}$$

These two equations together then imply that $\nabla \sigma_2^F = -\nabla \sigma_1^S$. In fact if we check equations (8.3), we see that the currents $J_S(x)$ and $-J_F(x)$ can, at steady state, differ by, at most, an overall additive constant and for systems with no overall mass current $J_F(x) = -J_S(x)$, i.e. $\sigma_n^F = -\sigma_{n-1}^S$.

Now let us compare these results with simulations of equations (8.1). We will consider the case where the switching rate from slow to fast is given by

$$\beta_S(x) = \frac{1}{1 + 9 \exp\left(-(100 - x)^2/100\right)}, \tag{8.26}$$

i.e. constant far from $x = 100$ and with a sharp decrease around that point. All other rates will be independent of position. The results of this comparison are shown in figures 8.4 and 8.5. As we can see the perturbation expansion approaches the correct form for the probability densities F and S but is a less good prediction of the currents as these are defined slightly differently for the spatially continuous theory and lattice simulations. Specifically, in the lattice simulations the currents that balance are defined as $J_S(i) = S_R(i) - S_L(i-1)$ and $J_F(i) = F_R(i) - F_L(i-1)$, i.e. over a bond between sites, not on site, whereas in the continuous theory $J_S(x) = S^R(x) - S^L(x)$ and $J_F(x) = F^R(x) - F^L(x)$.

To check the veracity of the perturbation expansion we consider the rms deviation between the densities predicted by the theory and those recorded in the simulations. To calculate this difference we subtract the predicted density from the measured density for each lattice site, square these differences, average them over the extent of the lattice and plot the square root of the resulting mean.

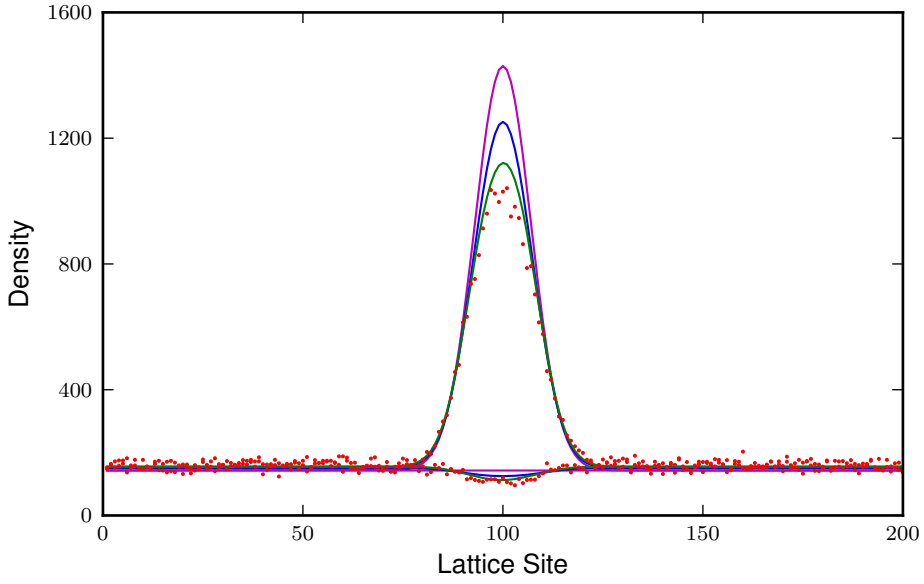

Figure 8.4: Data for a switching rate $\beta_S(x)$ as in equation (8.26). All other rates are constant. $v_S = 0.1$, $v_F = 1$. The density of slow particles (upper curves) and fast ones (lower curves) are shown for mean-field (deterministic) simulations and at 0th, 1st and 2nd order in the perturbation expansion. The simulation data points are shown in red, the 0th order theory in pink, 1st order in blue and 2nd order in green.

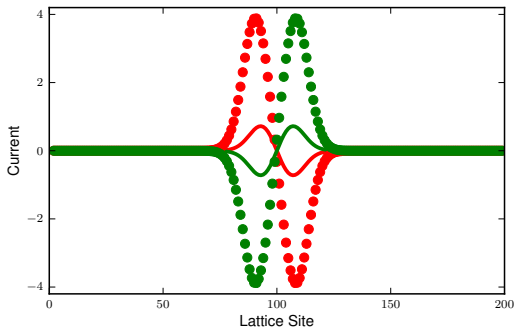

Figure 8.5: Data for a switching rate $\beta_S(x)$ as in equation (8.26). All other rates are constant. $v_S = 0.1$, $v_F = 1$. Plotted are the currents for fast particles, $J_F = v_F(F_R - F_L)$, and for slow particles, $J_S = v_S(S_R - S_L)$, as calculated from the simulations (points) and at 2nd order in the perturbation theory (solid lines).

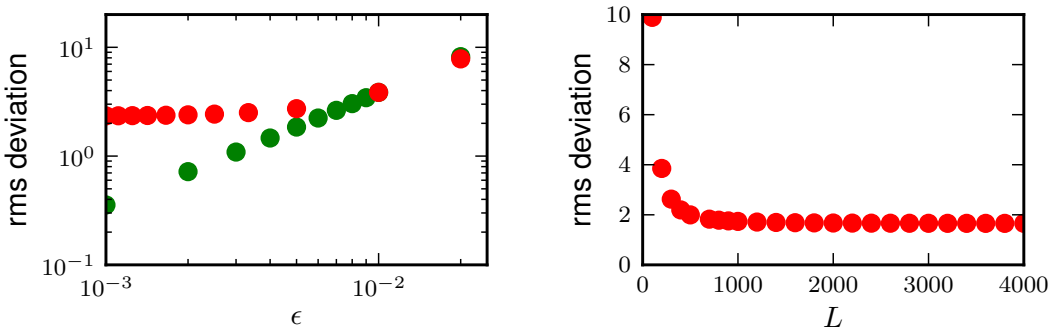

Figure 8.6: **Left**: The rms deviation between simulation and perturbation expansion, to first order, as a function of the ratio $\epsilon = v_S/v_F$. In red the data for v_S held constant equal to 0.1 and in green with v_F held constant equal to 10.0, both for a lattice of 200 sites. **Right**: The rms deviation as a function of lattice length with $v_S = 0.1$, $v_F = 10.0$. In both figures $\alpha = 1$, $\langle n \rangle = 400$, $\beta_F = 1$ and $\beta_{S_i} = \left(1 + 9\, e^{-\frac{1}{100}\left(100 - \frac{200}{L} i\right)^2}\right)^{-1}$, where L is the lattice length.

This average deviation is recorded for a fixed lattice size and choice of rates α and $\beta_{S/F}$ for a number of different values of the jump rate ratio, ϵ, see figure 8.6 (left). ϵ can be taken towards zero in two manners, by decreasing v_S or by increasing v_F. It was found that on decreasing v_S the average deviation tends to zero as would be expected. However, if v_S is held constant and v_F is increased the average deviation does not tend to zero in the limit $\epsilon \to 0$, but instead tends to a finite value. This suggests that there exists some other scale, call it v^*, in relation to which v_S must also be small, i.e. that we require not only that $v_S \ll v_F$ but also that $v_S \ll v^*$.

One immediate place we can look to improve the perturbation approach is to consider how decreasing the lattice spacing and increasing the number of sites on the lattice (so that the rates, which are a function of position, vary more smoothly) affects the deviations between theory and simulation. Effectively, as lattice length increases the system should resemble the continuum limit to a greater degree and, hence, deviations due to the discretization should be minimised. Indeed, it appears that below a lattice length of around 1000 sites, for this choice of parameters, the deviations increase considerably, but above that level there is little change with lattice length, see figure 8.6 (right).

The error from the perturbative expansion can therefore be attributed partially to the discretisation of the system, though this can be avoided if one uses suitably smooth profiles, i.e. a large enough number of sites. Note that we have

no analytical method to predict what 'enough' means, however. (We determine that empirically from the simulation data.) Even for small discretisations, i.e. large lattices, an error remains, though. This increases quickly with ϵ and never disappears if $v_S \neq 0$. Hence the perturbation method is of limited use for most practical applications. We need, then, to find a better method if we want to determine the steady state for two transmuting, motile species. Note also that we deal here only with static colony sizes; for colonies with realistic population dynamics the problems will become more pronounced still.

As we saw from the analysis in section 8.2.1 and in chapter 7, however, even in these complex cases we can still make qualitative predictions about the nature of the steady state and the stability of a homogeneous phase.

8.4 *Proteus mirabilis* and Periodically Expanding Colonies

Proteus mirabilis offers us one example of a species of bacteria which exists in multiple states during its life, which has been known of for over a century [98]. *Proteus* cells exist in two forms: a shorter *swimming* type, which in the dense agar concentrations we shall consider is immotile but can grow, and an extended *swarming* type, which can join with other swarming cells to form *rafts* which are then motile. As the swimming cells grow, instead of dividing into multiple swimming cells, they can, instead (if the local density is large enough), continue to grow as one cell and form a hyper-flagellated swarming cell—a process called differentiation. The swarming cells, which are motile when formed into rafts, will after some period of existence eventually turn back into multiple swimming cells (*consolidation*), which then grow as normal. For a review of the behaviour and microscopic swarming dynamics of *Proteus* see Rauprich et al. [99] or Allison and Hughes [100].

We therefore see a cycle of behaviour where a population of swimming cells grow and divide until they reach some threshold density ρ_1, at which point some fraction of them r will begin to differentiate into swarming cells. The densities of both the swimming cells, ρ_{swim}, and swarming cells, ρ_{swarm} then both increase for some time. This phase carries on only for a limited time, however, so once the density of swimmer cells passes a second threshold ρ_2 the differentiation process

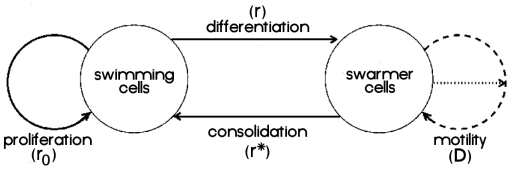

Figure 8.7: Schematic of the lifecycle of a *Proteus* cell. Swimming cells can reproduce at a rate r_0 or differentiate into swarmer cells at a rate r (which is a function of *rho* given in equation (8.28)). Swarmer cells can diffuse with a diffusivity D (which again is a function of the density, this time of swarmer cells) or consolidate back into swimmer cells at a rate r^*.

ends. Once the number of swarming cells increases above a third threshold ρ_3 they can form rafts and become motile. These motile rafts then spread out from the initial colony position, increasing the size of the colony, until enough swarming cells have consolidated back into swimming cells that $\rho_{swarm} < \rho_3$. The rafts are then no longer motile. The newly formed swimming cells—the product of the consolidation of the swarming cells—at the edge of the colony then grow until $\rho_{swim} > \rho_1$ again, more swarming cells can be formed, and the process repeats. In this way we see the boundary of the colony grow through a series of periodic expansions, for a schematic of the behaviour of a cell see figure 8.7.

Czirók et al. [101] modelled this behaviour via the coupled differential equations

$$\begin{aligned} \dot{\rho}_{swim} &= r_0\rho_{swim} + r^*\rho_{swarm} - r(\rho_{swim})\rho_{swim} \\ \dot{\rho}_{swarm} &= -r^*\rho_{swarm} + r(\rho_{swim})\rho_{swim} + \nabla D(\rho_{swarm})\nabla\rho_{swarm}, \end{aligned} \tag{8.27}$$

where r_0 is the growth rate of swimming bacteria, r^* is the consolidation rate to turn back into swimming bacteria from swarming, $r(\rho_{swim})$ is the rate to differentiate into swarmer cells and $D(\rho_{swarm})$ is the diffusivity. The functions r and D are given by

$$\begin{aligned} r(\rho_{swim}) &= \begin{cases} r & \text{if } \rho_1 < \rho_{swim} < \rho_2 \\ 0 & \text{otherwise} \end{cases} \\ D(\rho_{swarm}) &= \frac{D_0}{2}\left(1 + \tanh\left(2\alpha\frac{\rho_{swarm} - \rho_3}{\rho_{swarm}}\right)\right), \end{aligned} \tag{8.28}$$

where D_0 and α are two constants which allows us to tune the motility of the

swarmer cells.

This phenomenological model was able to reproduce the observed expansion of the colony front—though they were only able to test their results in one dimension and did not take into account the effect of noise on the system, nor could they reproduce the steady state behind the front. In their model the density of bacteria behind the front continues to grow indefinitely with no upper bound. Previous studies, such at Hallatschek and Korolev's [102] analysis of Fisher waves in the stochastic Fisher-Komolgorov-Petrovsky-Piscounov (sFKPP) equation, have shown that the presence of noise can have significant qualitative effects on front dynamics. It is, therefore, interesting to consider whether the results of the Czirók model are altered if we consider an inherently stochastic particle based description, instead of their PDEs.

To extend their analysis, we simulate a two-dimensional lattice model of the *Proteus* dynamics based on the multiple transmuting species model described in section 8.1, though now coupled to a logistic population dynamics for the swimming cells. Because we simulate the bacteria as individual agents the simulations presented here have an innate stochasticity built into them. The rates for switching between type and diffusivity of the swarming cells are taken as in equations (8.28). The swimming cells are taken to be non-motile, i.e. $v_s = 0$ in the language of section 8.1.

As Czirók et al. observed [101], we see a periodic extension of the colony front, which proceeds isotropically. Defining the colony as including any site on the lattice with a total bacterial density above some arbitrary threshold ρ_4 we can measure the average diameter of the colony and plot that against time (see figure 8.8). We see that the inclusion of noise and the extension to higher dimensions do not radically alter the results obtained from the deterministic one dimensional equations. (Note that changing the arbitrary threshold ρ_4 does not significantly alter any of our results, merely introducing a small overall shift in the colony size at any given time and increasing or reducing the susceptibility of the measurements to small fluctuations at the boundary.)

Our model still does not account for the observed behaviour behind the colony front; to describe that correctly would probably require the explicit introduction of a field describing the food source—which could be depleted and lead to an arresting of the growth of the colony in its interior. Such an extension of our

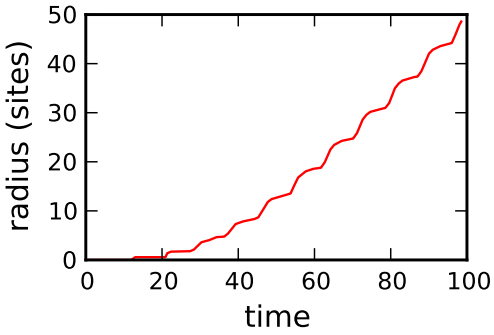

Figure 8.8: The average radius of a colony of *Proteus* bacteria. The radius is calculated by counting the number of lattice cells which have a total bacterial density greater than an arbitrary threshold dividing the result by π and taking the square root. The data come from a simulation carried out with parameters: $\alpha = 20$, $r_0 = 0.7$, $r^* = 0.7$, $r = 0.07$, $\rho_1 = 1000$, $\rho_2 = 1500$, $\rho_3 = 15$ and $D_0 = 50$.

model would be relatively simple to add computationally, though would add significant additional analytic complexity.

The model thus described seems to capture the front dynamics well, though at the expense of a considerable number of free parameters (r, r^*, r_0, D_0, α, ρ_1, ρ_2 and ρ_3). When planning this study it was hoped that this could be reduced, though this was not found to be possible (though it was neither shown to be not possible!). These exploratory simulations do, however, successfully extend the model of Czirók et al. to a more realistic dimensionality and properly account for the effect of noise.

8.5 Competition Between Multiple Species

Rather than consider a single species of bacteria which can exist in multiple forms, we may wish instead to consider a situation where we have multiple different species of bacteria occupying the same substrate. We can then think how the multiple species could interact with each other and what sort of qualitative states could be formed.

One obvious consideration would be to determine if, as a result of birth and death processes, one species or other will come to dominate the space, either through some fitness advantage or through random fluctuations. We then need to connect the multiple species models to the population dynamics of chapter 7.

Let us consider first just two species of bacteria, of equal fitness, occupying the

same space, consuming the same food supply and interacting, therefore, through coupled logistic growth terms. We want to know how the populations of the two species vary over time—whether one species does come to dominate—and how interactions in the motility, either of one species or across species, affect the overall populations. Can interactions lead to separation of the species into different spatial region? Can they lead to the dominance of one or other species happening more quickly than in a neutral environment?

To determine if interactions in either the population or motility can lead to separation of species, let us examine the linear stability of the diffusion level equations governing the populations' dynamics, given by

$$\begin{aligned}\dot{\rho}_A(\mathbf{x},t) &= \nabla\cdot\left[D_A^{col}\nabla\rho_A(\mathbf{x},t)\right] + \mu_A\rho_A\left(1-\frac{\rho_A+\rho_B}{\rho_0}\right) - \kappa_A\Delta^2\rho_A \\ \dot{\rho}_B(\mathbf{x},t) &= \nabla\cdot\left[D_B^{col}\nabla\rho_B(\mathbf{x},t)\right] + \mu_B\rho_B\left(1-\frac{\rho_A+\rho_B}{\rho_0}\right) - \kappa_B\Delta^2\rho_B.\end{aligned} \tag{8.29}$$

The collective diffusivities for each species in equation (8.29) may depend on either or both of the bacterial densities, depending on the form of microscopic motility interaction. There may be no motility interaction between species—so that $D_i^{col} = D_i^{col}(\rho_i)$—there may be an interaction which depends on the total density, a steric interaction for example—so that $D_i^{col} = D_i^{col}(\sum_i \rho_i)$—or an interaction which depends on both densities in some non-symmetric manner—so that $D_i^{col} = D_i^{col}(\{\rho_i\})$.

As ever, we expand around a flat profile at the carrying capacity ρ_0 and Fourier transform to determine the stability of the dynamics. We now have potentially two growth rates and two surface tension coefficients. We choose to rescale the densities, space and time by

$$u_{A/B} = \frac{\rho_{A/B}}{\rho_0}; \qquad \tilde{x} = \left(\frac{\mu_A}{\kappa_A}\right)^{1/4} x; \qquad \tilde{t} = \mu_A t. \tag{8.30}$$

We end up, after expanding around $u_A = u_B = 1/2$, with the two equations

$$\begin{aligned}\dot{\delta q}_A &= -q^2\frac{D_A^{col}}{\sqrt{\mu_A\kappa_A}}\delta q_A - \frac{1}{2}\delta q_A - \frac{1}{2}\delta q_B - q^4\delta q_A \\ \dot{\delta q}_B &= -q^2\frac{D_B^{col}}{\sqrt{\mu_A\kappa_A}}\delta q_A - \frac{\bar{\mu}}{2}\delta q_A - \frac{\bar{\mu}}{2}\delta q_B - \bar{\kappa}q^4\delta q_A,\end{aligned} \tag{8.31}$$

where we have defined the ratios $\mu_B/\mu_A = \bar{\mu}$ and $\kappa_B/\kappa_A = \bar{\kappa}$.

Note that even when $D^{col}_{A/B}$ depend on both densities, in the linear analysis the only cross terms come from the birth-death competition. This is in contrast to the transmuting case presented in section 8.2.1 where there are cross terms of the form $\nabla\left(D_{AB}\nabla\rho_B\right) + \nabla\left(D_{AA}\nabla\rho_A\right)$ for $\dot{\rho}_A$ (and similar terms for $\dot{\rho}_B$) which lead to additional cross terms in the stability analysis.

The matrix Λ in the equation $\dot{\delta\mathbf{q}} = \Lambda\delta\mathbf{q}$ will always be of the form

$$\Lambda = \begin{pmatrix} A(\rho_0)q^2 - q^4 - \frac{1}{2} & -\frac{1}{2} \\ -\frac{\bar{\mu}}{2} & B(\rho_0)q^2 - \bar{\kappa}q^4 - \frac{\bar{\mu}}{2} \end{pmatrix}, \tag{8.32}$$

where $A(\rho_0)$ and $B(\rho_0)$ are two functions of the density ρ_0 around which we expand. The resulting eigenvalues from this matrix are of the form

$$\begin{aligned} \Lambda^{\pm}(q) = \frac{1}{2}\Bigg(&\left(A(\rho_0) + B(\rho_0)\right)q^2 - (1+\bar{\kappa})q^4 - \frac{1}{2}(1+\bar{\mu})\Bigg) \\ &\pm \frac{1}{2}\left(\left(\left(A(\rho_0) - B(\rho_0)\right)q^2 - (1\bar{\kappa})q^4 - \frac{1}{2}(1-\bar{\mu})\right)^2 + \bar{\mu}\right)^{1/2}. \end{aligned} \tag{8.33}$$

As in section 8.2.1 we have two eigenvalues now. In the limiting case where the dynamics of the system is symmetric between the two species, that is where $\bar{\kappa} = 1$, $\bar{\mu} = 1$ and $D^{col}_A = D^{col}_B$, these eigenvalues simplify considerably to be

$$\Lambda^{+}(q) = \frac{D^{col}}{\sqrt{\mu\kappa}}q^2 - q^4; \qquad \Lambda^{-}(q) = \frac{D^{col}}{\sqrt{\mu\kappa}}q^2 - q^4 - 1. \tag{8.34}$$

The corresponding eigenvectors also simplify considerably. Where in general they depend on q and the microscopic parameters in some complex fashion and cannot be easily related back to the two species' densities, for symmetric dynamics they are given by

$$\mathbf{v}^{+} = \begin{pmatrix} 1 \\ 1 \end{pmatrix}; \qquad \mathbf{v}^{-} = \begin{pmatrix} 1 \\ -1 \end{pmatrix}. \tag{8.35}$$

One of these eigenvalues then tells us the stability of total density $\rho = \rho_A + \rho_B$, and the other which gives us the relative stability between species—whether the two species will dissociate. Neither of these eigenvalues may be positive, implying we have a homogeneous flat profile at steady state, one may be positive, and the

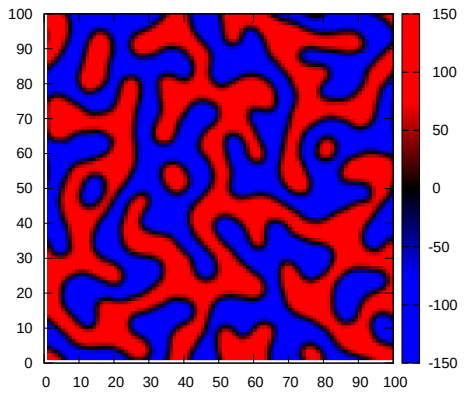

Figure 8.9: A snapshot of a system of two species of bacteria with identical microscopic dynamics competing for a common food supply. The simulation is performed with an interaction in the jump rate so that $v_{A/B} = 2\exp(-0.1\rho_{A/B})$, i.e. each species' velocity depends only on the density of that species. The other simulation parameters are: $\alpha_0 = 1$, $\mu = 0.1$ and $\rho_0 = 100$.

other negative, implying that the system will just separate into high and low density regions but with no systemic separation between A and B, or both could be positive, such that bacteria separate into different regions for each species. For an illustration of the species dissociated state see figure 8.9.

Though this work is only at a preliminary stage (and included as an illustration of the more complex situations we can model using the frameworks developed throughout this thesis) the results obtained so far are already interesting. The above analysis, for example, suggests that even where the microscopic dynamics have no obvious mechanism for dissociating species—where D^{col} depends on the total density only, say—we can still see such an instability. Further, we calculated only the stability around $\rho_A = \rho_B = \rho_0/2$; the stability around some other solution of $\rho_A + \rho_B = \rho_0$ could yield different results. Indeed, an instability around equal densities could force the system into a dissociated state which then subsequently was unstable to changes in total density.

8.6 Outlook

There are a number of avenues open for further work on the topic of multiple interacting and reproducing bacteria. It may be interesting to calculate the fixation times for one or other species to completely dominate a space, by means of a first passage approach for one species to disappear (to go extinct). Is this time then altered by interactions in any systemic manner? In the case of separation into micro-colonies, one could expect the smaller effective population size to equate to a faster fixation time; a quantitative analysis of this effect for various interaction strengths would be worthwhile.

Related to this project, and returning to the models of switching between multiple phenotypes, there may be more we can investigate. The survival probability and average density after some catastrophe (in which some large fraction of all bacteria are killed), with or without switching to an immune/dormant state, could be interesting to examine. Assaf et al. [103] analysed a non-spatial (well-mixed or mean-field) logistic growth model and considered the effect of a catastrophe implemented by a drastic reduction in the birth rate for some fixed time. Following a generating function approach to solving the master equation and making an eikonal approximation (similar to the WKB approximation in quantum physics) they were able to calculate the phase trajectories with an effective classical Hamiltonian and find some analytic solutions. Our models are considerably more complex than that considered there, though there may be results we can obtain, at least in a well-mixed environment. Further results for spatially structured systems could then be examined numerically. The two measures $\langle\rho\rangle$ and $P(\rho > 0)$ could be determined (either analytically or measured from simulations) and compared. Are there conditions for conflict between them—when might one be favoured over the other?

Chapter 9

Conclusion

In this work I have presented several classes of lattice models based on the run-and-tumble dynamics of certain species of bacteria, notably *Escherichia coli*. I calculated the exact steady state probability distributions for both inhomogeneous, anisotropic, non-interacting and zero-range interaction models. For more general types of interaction I used a field theoretic approach to derive the continuum fluctuating hydrodynamic equations and from there derived a mapping to a free energy like functional describing the steady state profile for a crowding interaction. I analysed the linear stability of both the continuum and lattice microscopic mean field equations. This allowed me (in chapter 6) to isolate a condition on the coarse-graining I employed in the interaction terms. If the coarse-graining is taken in an isotropic manner then the zero-range free energy will work as a mean field theory.

This work builds on earlier treatments of run-and-tumble bacteria where interactions between bacteria were not included [2, 22]. It provides a lattice counterpart to prior continuum approaches and qualitatively reproduces results obtained off lattice, where a similar, though not exactly equivalent, density dependence was considered [4]. My approach on lattice provides a microscopic justification for the manner in which this density dependence is addressed; previously it was added in an ad-hoc manner after the diffusive approximation had been taken, whereas in this work the dependence is intrinsic from the microscopic definition of the dynamics. That this produces qualitatively similar results justifies the way in which the dependence was handled previously. My work also reveals a condition on the coarse-graining procedure for this density dependence

for free energy mapping to work; it must be taken isotropically, so that particles moving in any direction feel the same effective local density. Further, in deriving a mapping between the method of this coarse-graining and an effective surface tension, I have shown that it is possible to calculate all the parameters required to determine the dynamic linear stability from the microscopic dynamics.

This work provides a means to simulate microscopic run-and-tumble dynamics efficiently, which is particularly important in two or more dimensions where microscopic simulations off lattice are very computationally expensive. It illustrates potential hazards in comparing lattice simulations and continuum theoretical predictions and offers some insight into how to avoid those problems by carefully choosing how to implement non-local interactions in the lattice dynamics. Note that early studies of off-lattice run-and-tumble dynamics actually had to discretise space to do simulation for position dependent swimming speed in order to compare with their theoretical predictions [22].

My work in chapter 6 has extended those prior models [2, 4, 22] to consider more carefully the effect of a finite tumble duration in the context of a density dependent motility. Whilst most previous work has taken tumbling to be instantaneous I have shown that in this context the finite nature of the tumbling can have a significant effect on the dynamics and steady state behaviour.

By coupling the microscopic model of run-and-tumble motility to a model of population dynamics I have (in chapter 7) been able to produce a simple mechanism by which patterning can arise in bacterial colonies. A dynamic instability arising from a density dependent motility is driven to coarsen by a small non-locality in the interaction which induces an effective surface tension. This coarsening is then arrested by the population dynamics. This mechanism is quite generic and I believe should form the basis of a null hypothesis against which more complex models of pattern formation should be tested.

Indeed, in chapter 7 I showed that this mechanism can arise from a variety of microscopic models and that 'death', as such, is not even required for patterns to exist. It is merely required that the net growth rate decreases as density increases. Currently this statement is of a qualitative nature only, and the patterns may be fleetingly transient depending on the precise choice of parameters. It would be a productive exercise, in the future, to form more precise mathematical conditions here.

Nevertheless, I hope the techniques presented in this thesis will further develop the use of lattice simulations in the context of bacterial population growth. The lattice approach may, for example, help to provide new analytic and computational results for run-and-tumble dynamics in higher dimensions, generalizing previous studies to more general external potentials for sedimentation and trapping [3]. Or, as described in chapter 8, the work may lead to new possibilities to study competition between multiple species of bacteria.

In terms of the specific results presented in this thesis, the saturated condensation process considered in chapter 5 complements existing treatments of the condensation dynamics for the version of the ZRP with a true condensation transition [64–68]. In those works the focus has primarily been on the late-time scaling behaviour of cluster size, and the characteristic timescales for evaporation and reformation of condensates. Within the model of saturated condensation discussed here, I have obtained a more complete account of the dynamics—including the nontrivial behaviour of the number of condensate sites—from very early times right through to the steady state. In particular, I found that the relaxation takes place in two stages: first, some number of condensate sites is dynamically selected which depends on the initial condition. These condense rapidly, but leave the system in an out-of-equilibrium state that slowly relaxes through activated evaporation and condensation events. A mean-field approximation proved reliable in analysing the first stage, and a first-passage calculation conducted within a specially-constructed 'doubly' grand canonical ensemble well described the second.

This first-passage calculation, while reasonably accurate (within a factor of two over two orders of magnitude), does show some discrepancy when compared with the relaxation rate measured from simulation data. As I discussed at the end of chapter 5 this difference may arise from the approximations made in order to perform the analytic calculation. It is not clear, however, how (or indeed if) this could be improved upon.

More serious, perhaps, is the absence of a satisfactory explanation for the number of condensate sites formed from a uniform initial condition. One would anticipate that the early-time noise would play a major role in determining this number, although I have been unable to relate these two quantities directly. This very early time dynamics presents itself as one possible route by which this work

could be continued.

Additionally, since I believe the model to reproduce more faithfully experimental situations such as the shaken granular gases than the traditional version of the ZRP, it would be very interesting to investigate both early- and late-time dynamics of the corresponding experiments [63].

With regards to the work presented in chapter 6, there remain a number of open questions regarding the coexistence densities for interacting bacteria. Although the fluctuating hydrodynamics correctly predicts the existence of phase separation, the coexistence densities are accurately predicted only for isotropic kernels and large lattice occupancies. Quantitative predictions beyond this case are yet to be derived. More general non-linear interaction kernels have also not yet been considered.

Questions and potential openings for future study arise from the work on population dynamics considered in chapters 7 and 8 as well. Firstly, there is a need to calculate the collective diffusivity, D_{col}, empirically from the simulations by measuring the decorrelation of fluctuations. Holding the single particle diffusivity, D, constant and changing D_{col}, as described in section 7.1, we can look at the correlation functions as you approach the transition and verify that it is the collective and not single particle diffusivity (as measured by the mean-squared displacement of the bacteria) that controls the onset of instability. Though we have shown via simulation that homogeneous profiles become unstable at the point when the microscopic parameters are predicted to result in a negative collective diffusivity, backing this measurement directly from the data would strengthen the argument further.

Secondly, different 'death' mechanisms require further investigation to ensure that these do not qualitatively alter the results. In section 7.4 I detailed some work in ensuring the robustness of the model; more could be done explicitly counting bacteria in different states (motile and growing, motile non-growing, non-motile, dead). A more quantitative account of the conditions on the net growth rate (as a function of density) required for pattern formation could also be formulated.

Finally, a derivation of the two-dimensional, finite tumble time results conducted using the full field theoretic treatment would allow us to determine the noise terms in the resulting reaction-diffusion equation governing the evolution

of the bacterial density. It could then be interesting to check the noise terms explicitly against the simulations.

Further to these obvious extensions of the work presented in this thesis, a number of other avenues for future work also present themselves. In relation to the ring formation seen in chapter 7, the role of the front dynamics in facilitating patterning in the trailing bulk phase could be investigated in more detail. It appears from preliminary examination that even where no instability exists at the target density—that is where $\lambda(q) < 0$ for all q at $\rho = \rho_0$—patterning can still occur if the front passes through a density region of instability—if $\lambda(q) > 0$ at some $\rho < \rho_0$. It remains an open question, however, as to under what circumstances and in what manner such patterning can become fixed behind the front. If the pattern is not stable and permanently fixed, can we estimate the length or time scales for patterns behind the front to remain? Can we make analytic progress in analysing the front stability? If we can determine the front shape, $\rho(x, t)$, and look for a frame in which it is time independent, can we perform the stability analysis in that frame? It may be very difficult (or indeed impossible) analytically, but can we find simulations in which the shape is important? i.e where the stability around a flat profile gives a different result to that seen in simulations, implying that the stability around the front shape is different? All these questions remain to be answered.

Appendix A

Hydrodynamic Limit and Scaling of Fields in the Action

The microscopic action for the non-interacting, homogeneous and isotropic model can be written as

$$\begin{aligned} S &= -\int_0^T \sum_i \Big[\hat{\rho}_i \dot{\rho}_i + \frac{1}{d}\hat{J}_i \dot{J}_i + \frac{d}{2}\rho_i \left(e^{-(\hat{\rho}_{i+1}-\hat{\rho}_i+\hat{J}_{i+1}-\hat{J}_i)} + e^{\hat{\rho}_{i+1}-\hat{\rho}_i-(\hat{J}_{i+1}-\hat{J}_i)} - 2 \right) \\ &+ \frac{J_i}{2}\left(e^{-(\hat{\rho}_{i+1}-\hat{\rho}_i+\hat{J}_{i+1}-\hat{J}_i)} - e^{\hat{\rho}_{i+1}-\hat{\rho}_i-(\hat{J}_{i+1}-\hat{J}_i)} \right) \\ &+ \frac{d}{2}(\rho_{i+1}-\rho_i-\frac{J_{i+1}-J_i}{d})\left(e^{\rho_{i+1}-\hat{\rho}_i-(\hat{J}_{i+1}-\hat{J}_i)} - 1 \right) \\ &+ \frac{\alpha\rho_i}{4}\left(e^{2\hat{J}_i} + e^{-2\hat{J}_i} - 2 \right) + \frac{\alpha J_i}{4d}\left(e^{2\hat{J}_i} - e^{-2\hat{J}_i} \right) \Big]. \end{aligned} \tag{A.1}$$

The continuous limit can be taken by explicitly introducing the lattice spacing a and making the substitutions

$$\begin{aligned} \rho_i \to a\rho(x); \quad \hat{\rho}_i \to \hat{\rho}(x); \quad d \to va^{-1}; \quad \textstyle\sum_i \to \int_0^{\ell=La} \mathrm{d}x a^{-1}; \\ J_i \to J(x); \quad \hat{J}_i \to \hat{J}(x); \quad \nabla_i \to a\nabla + \tfrac{1}{2}a^2\Delta \end{aligned} \tag{A.2}$$

where ∇_i is the discrete gradient, e.g. $\nabla_i \rho_i = \rho_{i+1} - \rho_i$. This overall substitution and the Taylor expansion of the action then gives

$$\begin{aligned} S &= -\int_0^T \mathrm{d}t \int_0^\ell \mathrm{d}x \left[\hat{\rho}\dot{\rho} + v^{-1}\hat{J}\dot{J} - v\rho\nabla\hat{J} - J\nabla\hat{\rho} + \frac{\alpha\rho}{4}\left(e^{2\hat{J}} + e^{-2\hat{J}} - 2\right) \right. \\ &+ \left. \frac{\alpha J}{4v}\left(e^{2\hat{J}} - e^{-2\hat{J}}\right) \right] + aS_1, \end{aligned} \tag{A.3}$$

where the neglected term S_1 is given by

$$\begin{aligned} S_1 &= -\int_0^T \mathrm{d}t \int_0^\ell \mathrm{d}x \left[v\rho\big[-\frac{1}{2}\Delta\hat{J} + (\nabla\hat{\rho})^2/2 + (\nabla\hat{J})^2/2\big] + J\big[-\Delta\hat{\rho}/2 + \nabla\hat{\rho}\nabla\hat{J}\big] \right. \\ &+ \left. v/2\big(\nabla\rho - \nabla J/v\big)\big(\nabla\hat{\rho} - \nabla\hat{J}\big) \right] + \mathcal{O}(a). \end{aligned} \tag{A.4}$$

To calculate the correct manner in which to rescale our fields let us begin by considering a system ℓ times larger and rescaling $t \to t\ell^\alpha$, $x \to x\ell$, $\rho \to \rho/\ell$ so that the action is given by

$$\begin{aligned} S &= -\int_0^{T/\ell^\alpha} \mathrm{d}t \int_0^1 \mathrm{d}x \left[\hat{\rho}\dot{\rho} + \ell\frac{\hat{J}\dot{J}}{v} - \ell^{\alpha-1}v\rho\nabla\hat{J} - \ell^\alpha J\nabla\hat{\rho} - \ell^\alpha\frac{\alpha}{4}\rho\left(e^{2\hat{J}} + e^{-2\hat{J}} - 2\right) \right. \\ &- \left. \ell^{\alpha+1}\frac{\alpha}{4v}J\left(e^{-2\hat{J}} - e^{2\hat{J}}\right) \right] \end{aligned} \tag{A.5}$$

For the $\hat{J}$ terms to not blow up we need to have $\hat{J}$ small. We therefore expand the exponentials to give

$$S = -\int_0^{T/\ell^\alpha} \mathrm{d}t \int_0^1 \mathrm{d}x \left[\hat{\rho}\dot{\rho} + \ell\frac{\hat{J}\dot{J}}{v} - \ell^{\alpha-1}v\rho\nabla\hat{J} - \ell^\alpha J\nabla\hat{\rho} - \ell^\alpha\alpha\rho\hat{J}^2 + \ell^{\alpha+1}\frac{\alpha}{v}J\hat{J} \right]. \tag{A.6}$$

If we explicitly take $\hat{J}$ to scale as $\hat{J} \to \hat{J}\ell^{-\beta}$ and $J \to J\ell^{-\delta}$ we get

$$\begin{aligned} S &= -\int_0^{T/\ell^\alpha} \mathrm{d}t \int_0^1 \mathrm{d}x \left[\hat{\rho}\dot{\rho} + \ell^{1-\beta-\delta}\frac{\hat{J}\dot{J}}{v} - \ell^{\alpha-1-\beta}v\rho\nabla\hat{J} \right. \\ &- \left. \ell^{\alpha-\delta}J\nabla\hat{\rho} - \ell^{\alpha-2\beta}\alpha\rho\hat{J}^2 + \ell^{\alpha-\beta-\delta+1}\frac{\alpha}{v}J\hat{J} \right]. \end{aligned} \tag{A.7}$$

Now, we need the coefficient of each term to be of order 1 or smaller so that no terms blow up so

$$1-\beta-\delta \leq 0; \qquad \alpha-1-\beta \leq 0; \qquad \alpha-\delta \leq 0; \qquad \alpha-2\beta \leq 0; \qquad 1+\alpha-\beta-\delta \leq 0. \tag{A.8}$$

However, as we do not want to simply be left with $\dot{\rho} = 0$ we need $\alpha - \delta = 0$ and as we also want to retain a noise, which corresponds to the $\hat{J}^2$ term, we also require that $\alpha - 2\beta = 0$. That leaves our action

$$S = -\int_0^{T/\ell^\alpha} \mathrm{d}t \int_0^1 \mathrm{d}x \left[\hat{\rho}\dot{\rho} + \ell^{1-3\beta}\frac{\hat{J}\dot{J}}{v} - \ell^{\beta-1}v\rho\nabla\hat{J} - J\nabla\hat{\rho} - \alpha\rho\hat{J}^2 + \ell^{1-\beta}\frac{\alpha}{v}J\hat{J}\right]. \tag{A.9}$$

Which tells us that $\beta \leq 1$, $\beta \geq 1/3$ and $\beta \geq 1$ which imply that $\beta = 1$ and hence $\alpha = 2$ and $\delta = 2$. Injecting these scalings back into the action gives

$$S = -\int_0^{T/\ell^2} \mathrm{d}t \int_0^1 \mathrm{d}x \left[\hat{\rho}\dot{\rho} + \ell^{-2}v^{-1}\hat{J}\dot{J} - v\rho\nabla\hat{J} - J\nabla\hat{\rho} + \alpha\rho\hat{J}^2 + \frac{\alpha J\hat{J}}{v}\right] \tag{A.10}$$

where the macroscopic observation time $\tau = T/\ell^2$ is supposed to be of order 1. The term in $\hat{J}\dot{J}$ is thus irrelevant and we can check that the hydrodynamic action

$$S_0 = -\int_0^{\tau} \mathrm{d}t \int_0^1 \mathrm{d}x \left[\hat{\rho}\dot{\rho} - v\rho\nabla\hat{J} - J\nabla\hat{\rho} + \alpha\rho\hat{J}^2 + \frac{\alpha J\hat{J}}{v}\right] \tag{A.11}$$

is invariant under further diffusive scaling. Note that the scaling of the fields considered here is arbitrary and we could *choose* to look at currents J, $\hat{J}$ larger than $1/\ell^2$, $1/\ell$. This would correspond to trajectories whose probabilities are smaller than $\exp(-\ell)$, which are not correctly described by fluctuating hydrodynamics and large deviations. One can also check that under this rescaling, the action S_1 stays of order 1 and aS_1 is thus, indeed, negligible.

For one isolated bacterium the run-and-tumble dynamics is a variant of a random walk and is known to be diffusive at large scales [2, 4]. It is therefore not surprising that we find $\alpha = 2$. In the presence of interactions (as in section 3.2.3), a uniform density profile of bacteria will continue to exhibit diffusive behaviour; the interactions will simply rescale the diffusivity. If interactions cause the profile to become unstable, however, the model can nevertheless give rise to length scales which grow in a non-diffusive manner, as for example for coarsening (see

section 6.3).

Appendix B

Solution of the first passage time problem

The first passage time from n particles to n_{peak} is denoted $T_{n,n_{\text{peak}}}$ and, in continuous time, is given by the solution to the equation

$$T_{n,n_{\text{peak}}} = \mathrm{d}t + [1 - (u_L + u(n))\ \mathrm{d}t\,]\, T_{n,n_{\text{peak}}} + u(n)\,\mathrm{d}t\, T_{n-1,n_{\text{peak}}} + u_L\,\mathrm{d}t\, T_{n+1,n_{\text{peak}}} \tag{B.1}$$

This equation states that the time to go from n to n_{peak} particles (l.h.s) is dt plus the time to go from the new number of particles, obtained after a time interval dt, to n_{peak}. With probabilities $u(n)\,dt$ and $u_L\,dt$, there are now $n-1$ or $n+1$ particles, while with probability $1-(u_L+u(n))\,dt$ there are still n particles, hence the three terms of the r.h.s. Equation (B.1) then reduces to

$$(u_L + u_n)\, T_{n,n_{\text{peak}}} - u_L\, T_{n+1,n_{\text{peak}}} - u(n)\, T_{n-1,n_{peak}} = 1 \tag{B.2}$$

with boundary condition $T_{n_{\text{peak}},n_{\text{peak}}} = 0$. Now, define the difference $d_n = T_{n,n_{\text{peak}}} - T_{n-1,n_{\text{peak}}}$ so that

$$u(n)\, d_n - u_L\, d_{n+1} = 1. \tag{B.3}$$

Note that the evolution of the probability to find n particles at a site, $p(n|\mu)$, is given by

$$\frac{\mathrm{d}p(n|\mu)}{\mathrm{d}t} = u(n+1)\, p(n+1|\mu) + u_L\, p(n-1|\mu) - (u(n) + u_L)\, p(n|\mu) \tag{B.4}$$

$$\equiv J_{n+1,n} - J_{n,n-1} \tag{B.5}$$

where $J_{n+1,n} = u(n+1)\,p(n+1|\mu) - u_L\,p(n|\mu)$. At steady state the left hand side of this equation must equal zero, so the current, J must be constant. However, as $p(n<0|\mu) = 0$ and $v_0 = 0$, $J_{-1,0} = 0$ and hence this constant must be zero. This implies that $u(n+1)\,p(n+1|\mu) = u_L\,p(n|\mu)$ so the solution to the homogeneous version of equation (B.3) is:

$$d_n = \frac{1}{u(n)\,p(n|\mu)}. \tag{B.6}$$

To solve the inhomogeneous equation, then, we look for solutions of the form

$$d_n = \frac{c_n}{u(n)\,p(n|\mu)}. \tag{B.7}$$

where c_n is to be determined. Substituting this expression back into equation (B.3) gives

$$-u_L\,\frac{c_{n+1}}{u(n+1)\,p(n+1|\mu)} + u(n)\,\frac{c_n}{u(n)\,p(n|\mu)} = 1. \tag{B.8}$$

The detailed balance condition, $u(n+1)\,p(n+1|\mu) = u_L\,p(n|\mu)$, then implies

$$c_n - c_{n+1} = p(n|\mu), \tag{B.9}$$

so that $c_n = \sum_{l=n}^{\infty} p(l|\mu)$ and the first passage time is given by

$$T_{n,n_{\text{peak}}} = \sum_{l=n_{\text{peak}}+1}^{n} \frac{1}{u(l)\,p(l|\mu)} \sum_{m=l}^{\infty} p(m|\mu). \tag{B.10}$$

Appendix C

Stability Analyses

Beginning with the mean field equations for the partial exclusion-like interaction,

$$\dot{n}^+ = d\, n^+_{i-1}\left(1-\frac{n_i}{n_m}\right) - d\, n^+_i\left(1-\frac{n_{i+1}}{n_m}\right) - \frac{\alpha\, n^+_i}{2} + \frac{\alpha\, n^-_i}{2} \tag{C.1}$$

$$\dot{n}^- = d\, n^-_{i+1}\left(1-\frac{n_i}{n_m}\right) - d\, n^-_i\left(1-\frac{n_{i-1}}{n_m}\right) + \frac{\alpha\, n^+_i}{2} - \frac{\alpha\, n^-_i}{2} \tag{C.2}$$

we can expand around a flat profile and take $n^\pm_k = n_0 + \sum_q \delta^\pm_q \exp(i\, q\, k)$ to investigate the linear stability. In matrix form the resulting equations can be written as

$$\dot{\delta_{\mathbf{q}}} = \begin{pmatrix} d\left(1-\frac{n_0}{n_m}\right)(e^{-iq}-1) + \frac{dn_0}{2n_m}(e^{iq}-1) - \frac{\alpha}{2} & \frac{dn_0}{2n_m}(e^{iq}-1) + \frac{\alpha}{2} \\ \frac{dn_0}{2n_m}(e^{-iq}-1) + \frac{\alpha}{2} & d\left(1-\frac{n_0}{n_m}\right)(e^{iq}-1) + \frac{dn_0}{2n_m}(e^{-iq}-1) - \frac{\alpha}{2} \end{pmatrix} \delta_{\mathbf{q}}, \tag{C.3}$$

where $\delta_{\mathbf{q}} = (\delta^+_q, \delta^-_q)$ as before. Defining the run length as the ratio $d/\alpha = r$, we can write the eigenvalues of this matrix as

$$\lambda_\pm(q) = \alpha\Bigg(-\frac{1}{2} + r\left(1-\frac{n_0}{2\, n_m}\right)(\cos(q)-1) \pm \left[-r^2\left(1-\frac{3\, n_0}{2\, n_m}\right)^2 \sin^2(q) + \frac{1}{4} + \left(\frac{r^2\, n_0^2}{2\, n_m^2} - \frac{r\, n_0}{2\, n_m}\right)(1-\cos(q)) \right]^{\frac{1}{2}} \Bigg). \tag{C.4}$$

Again, one eigenvalue is always negative while one can be positive or negative. In this case, however the condition for stability is no longer independent of q and

r. In particular, we find that $\lambda_+ > 0$ when

$$-2\,r^2\,\left(\frac{n_0}{n_m}\right)^2 - 2\,r^2 + 4\,r^2\,\left(\frac{n_0}{n_m}\right) - r + \cos(q)\,(2\,r^2\,\left(\frac{n_0}{n_m}\right) - 2\,r^2\,\left(\frac{n_0}{n_m}\right)^2) > 0. \tag{C.5}$$

Further, if we want to know only under what conditions on r and $\frac{n_0}{n_m}$ there exist any positive eigenvalues, we can consider the simpler condition

$$-2\,r^2\,\left(\frac{n_0}{n_m}\right)^2 - 2\,r^2 + 4\,r^2\,\left(\frac{n_0}{n_m}\right) - r + 2\,r^2\,\left(\frac{n_0}{n_m}\right) - 2\,r^2\,\left(\frac{n_0}{n_m}\right)^2 > 0, \tag{C.6}$$

which implies that

$$r > \frac{1}{2\,\left(1 - \frac{n_0}{n_m}\right)\left(\frac{2\,n_0}{n_m} - 1\right)}. \tag{C.7}$$

For the more general case where the microscopic mean field equations are given by

$$\begin{aligned}
\dot{n}^+ &= d\,n^+_{i-1}\left(1 - \frac{1}{n_m}\sum_j K^+_j\,n_{i+j-1}\right) - d\,n^+_i\left(1 - \frac{1}{n_m}\sum_j K^+_j\,n_{i+j}\right) \\
&- \frac{\alpha\,n^+_i}{2} + \frac{\alpha\,n^-_i}{2} \qquad \text{(C.8)} \\
\dot{n}^- &= d\,n^-_{i+1}\left(1 - \frac{1}{n_m}\sum_j K^-_j\,n_{i+j+1}\right) - d\,n^-_i\left(1 - \frac{1}{n_m}\sum_j K^-_j\,n_{i+j}\right) \\
&+ \frac{\alpha\,n^+_i}{2} - \frac{\alpha\,n^-_i}{2}, \qquad \text{(C.9)}
\end{aligned}$$

we can perform a similar analysis. Once again we expand around a flat profile, this time to obtain

$$\begin{aligned}
\dot{\delta}^+_q &= d\,\delta^+_q\,e^{-i\,q}\left(1 - \frac{1}{n_m}\sum_j K^+_j\,n_0\right) - d\,\delta^+_q\left(1 - \frac{1}{n_m}\sum_j K^+_j\,n_0\right) - \frac{\alpha}{2}\left(\delta^+_q - \delta^-_q\right) \\
&- \frac{d\,n_0}{2\,n_m}\left(\delta^+_q + \delta^-_q\right)\sum_j K^+_j\,e^{i(j-1)q} + \frac{d\,n_0}{2\,n_m}\left(\delta^+_q + \delta^-_q\right)\sum_j K^+_j\,e^{ijq} \qquad \text{(C.10)} \\
\dot{\delta}^-_q &= d\,\delta^-_q\,e^{i\,q}\left(1 - \frac{1}{n_m}\sum_j K^-_j\,n_0\right) - d\,\delta^-_q\left(1 - \frac{1}{n_m}\sum_j K^-_j\,n_0\right) + \frac{\alpha}{2}\left(\delta^+_q - \delta^-_q\right) \\
&- \frac{d\,n_0}{2\,n_m}\left(\delta^+_q + \delta^-_q\right)\sum_j K^-_j\,e^{i(j+1)q} + \frac{d\,n_0}{2\,n_m}\left(\delta^+_q + \delta^-_q\right)\sum_j K^-_j\,e^{ijq}. \qquad \text{(C.11)}
\end{aligned}$$

Now, we can define a new function $\kappa^{\pm}(q) = \sum_j K_j^{\pm} \exp(i\,j\,q)$. With this definition, and the normalisation of $K_j^{\pm}$, we can simplify equations (C.11).

$$\dot{\delta_{\mathbf{q}}} = \begin{pmatrix} d\left(1 - \frac{n_0}{n_m} - \frac{dn_0}{2n_m}\kappa^+(q)\right)(e^{-iq} - 1) - \frac{\alpha}{2} & -\frac{dn_0}{2n_m}(e^{-iq} - 1)\,\kappa^+(q) + \frac{\alpha}{2} \\ -\frac{dn_0}{2n_m}(e^{iq} - 1)\,\kappa^-(q) + \frac{\alpha}{2} & d\left(1 - \frac{n_0}{n_m} - \frac{dn_0}{2n_m}\kappa^-(q)\right)(e^{iq} - 1) - \frac{\alpha}{2} \end{pmatrix} \delta_{\mathbf{q}}, \tag{C.12}$$

For isotropic kernels, where $\kappa^{\pm}(q) = \kappa(q)$, it turns out we can write the eigenvalues in a relatively simple form and, even without knowledge of the specific shape of K_j, we can analyse the conditions under which there will exist positive eigenvalues. We start by writing the eigenvalues of the matrix in equation (C.12) as

$$\begin{aligned} \lambda_{\pm}(q) = \alpha\Bigg(& -\frac{1}{2} + r\left(1 - \frac{n_0\,(1 + 1/2\kappa(q))}{n_m}\right)(\cos(q) - 1) \\ & \pm \Bigg[- r^2 \left(1 - \frac{n_0\,(1 + 1/2\kappa(q))}{n_m}\right)^2 (1 - \cos(q))\,(1 + \cos(q)) \\ & + \frac{1}{4} - \frac{1}{2}\frac{r\,n_0\,\kappa(q)}{n_m}(\cos(q) - 1) + \frac{1}{2}\frac{r^2\,n_0^2\,\kappa^2(q)}{n_m}^2 (1 - \cos(q)) \Bigg]^{1/2} \Bigg). \end{aligned} \tag{C.13}$$

The larger of these two eigenvalues will be positive if

$$-2\,r^2 - r + \frac{r\,n_0}{n_m} - \frac{2\,r^2\,n_0^2}{n_m^2} + \frac{4\,r^2\,n_0}{n_m} + \kappa(q)\left(\frac{2\,r^2\,n_0}{n_m} - \frac{2\,r^2\,n_0^2}{n_m^2} + \frac{r\,n_0}{n_m}\right) > 0. \tag{C.14}$$

Further, as $K(x)$ is always positive, $\kappa(q)$ will have a maximum at $q = 0$, where $\kappa(0) = 1$, and so we can examine the simpler condition

$$-2\,r^2 - r + \frac{2\,r\,n_0}{n_m} - \frac{4\,r^2\,n_0^2}{n_m^2} + \frac{6\,r^2\,n_0}{n_m} > 0. \tag{C.15}$$

When this inequality is fulfilled we will see instability. Given that r must be positive this means any isotropic density kernel will be unstable in the range $n_0 \in [0.5\,n_m, n_m]$.

Bibliography

[1] M. E. Cates, D. Marenduzzo, I. Pagonabarraga, and J. Tailleur. Arrested phase separation in reproducing bacteria creates a generic route to pattern formation. *Proceedings of the National Academy of Sciences*, 107(26):11715–11720, 2010.

[2] M. J. Schnitzer. Theory of continuum random walks and application to chemotaxis. *Physical Review E: Statistical, Nonlinear, and Soft Matter Physics*, 48(4):2553–2568, 1993.

[3] J. Tailleur and M. E. Cates. Sedimentation, trapping, and rectification of dilute bacteria. *Europhysics Letters*, 86:60002, 2009.

[4] J. Tailleur and M. E. Cates. Statistical mechanics of interacting run-and-tumble bacteria. *Physical Review Letters*, 100(21):218103, 2008.

[5] R. A. Blythe and M. R. Evans. Nonequilibrium steady states of matrix-product form: a solver's guide. *Journal of Physics A: Mathematical and Theoretical*, 40(46):R333–R441, 2007.

[6] M. R. Evans and T. Hanney. Nonequilibrium statistical mechanics of the zero-range process and related models. *Journal of Physics A: Mathematical and General*, 38(19):R195–R240, 2005.

[7] Bernard D. Non-equilibrium steady states: fluctuations and large deviations of the density and of the current. *Journal of Statistical Mechanics: Theory and Experiment*, 2007(07):P07023, 2007.

[8] C. W. Gardiner. *Handbook of Stochastic Methods for Physics, Chemistry, and Natural Sciences*. Berlin: Springer, 2004.

[9] V. Westphal, S. O. Rizzoli, M. A. Lauterbach, D. Kamin, R. Jahn, and S. W. Hell. Video-rate far-field optical nanoscopy dissects synaptic vesicle movement. *Science*, 320(5873):246–249, 2008.

[10] J. Toner and Y. Tu. Long-range order in a two-dimensional dynamical xy model: How birds fly together. *Phys. Rev. Lett.*, 75(23):4326–4329, 1995.

[11] N. D. Mermin and H. Wagner. Absence of ferromagnetism or antiferromagnetism in one- or two-dimensional isotropic heisenberg models. *Phys. Rev. Lett.*, 17(22):1133–1136, 1966.

[12] E. M. Purcell. Life at low reynolds number. *American Journal of Physics*, 45:3–11, 1976.

[13] H.C. Berg. *E. coli in Motion*. Springer, New York, 2004.

[14] H. C. Berg and D. A. Brown. Chemotaxis in *Escherichia coli* analysed by three-dimensional tracking. *Nature*, 239(5374):500–504, 1972.

[15] H. C. Berg and R. A. Anderson. Bacteria swim by rotating their flagellar filaments. *Nature*, 245(5425):380–382, 1973.

[16] H. C. Berg. The rotary motor of bacterial flagella. *Annual Review of Biochemistry*, 72(1):19–54, 2003.

[17] H. C. Berg. Motile behavior of bacteria. *Physics Today*, 53(1):24–29, 2000.

[18] S. H. Larsen, R. W. Reader, E. N. Kort, W. Tso, and J. Adler. Change in direction of flagellar rotation is the basis of the chemotactic response in *Escherichia coli*. *Nature*, 249(5452):74–77, 1974.

[19] R. M. Macnab. Bacterial flagella rotating in bundles: a study in helical geometry. *Proceedings of the National Academy of Sciences of the United States of America*, 74(1):221–225, 1977.

[20] L. Turner, W. S. Ryu, and H. C. Berg. Real-time imaging of fluorescent flagellar filaments. *Journal of Bacteriology*, 182(10):2793–2801, 2000.

[21] H. C. Berg. Marvels of bacterial behavior. *Proceedings of the American Philosophical Society*, 150(3):428–442, 2006.

[22] M.J. Schnitzer, S.M. Block, H.C. Berg, and E.M. Purcell. Strategies for chemotaxis. *Symp. Soc. Gen. Microbiol.*, 46:15–34, 1990.

[23] R. Erban and H. G. Othmer. From individual to collective behavior in bacterial chemotaxis. *SIAM Journal on Applied Mathematics*, 65(2):361–391, 2004.

[24] P.-G. de Gennes. Chemotaxis: the role of internal delays. *European Biophysics Journal*, 33:691–693, 2004.

[25] M. A. Rivero, R. T. Tranquillo, H. M. Buettner, and D. A. Lauffenburger. Transport models for chemotactic cell populations based on individual cell behavior. *Chemical Engineering Science*, 44(12):2881 – 2897, 1989.

[26] D. A. Clark and L. C. Grant. The bacterial chemotactic response reflects a compromise between transient and steady-state behavior. *Proceedings of the National Academy of Sciences of the United States of America*, 102(26):9150–9155, 2005.

[27] Y. Kafri and R. A. da Silveira. Steady-state chemotaxis in *Escherichia coli*. *Physical Review Letters*, 100(23):238101, 2008.

[28] J E Segall, S M Block, and H C Berg. Temporal comparisons in bacterial chemotaxis. *Proceedings of the National Academy of Sciences*, 83(23):8987–8991, 1986.

[29] D. S. Dean. Langevin equation for the density of a system of interacting Langevin processes. *Journal of Physics A: Mathematical and General*, 29(24):L613–L617, 1996.

[30] J.K. Parrish and L. Edelstein-Keshet. Complexity, pattern and evolutionary trade-offs in animal aggregation. *Science*, 99:9645–9649, 1999.

[31] G. Theraulaz, E. Bonabeau, S. C. Nicolis, R. V. Sol, V. Fourcassi, S. Blanco, R. Fournier, J.-L. Joly, P. Fernndez, A. Grimal, P. Dalle, and J.-L. Deneubourg. Spatial patterns in ant colonies. *Proceedings of the National Academy of Sciences*, 99(15):9645–9649, 2002.

[32] M. Ballerini, N. Cabibbo, R. Candelier, A. Cavagna, E. Cisbani, I. Giardina, V. Lecomte, A. Orlandi, G. Parisi, A. Procaccini, M. Viale, and V. Zdravkovic. Interaction ruling animal collective behavior depends on topological rather than metric distance: Evidence from a field study. *Proceedings of the National Academy of Sciences*, 105(4):1232–1237, 2008.

[33] J.D. Murray. *Mathematical Biology*, volume 2. Spinger-Verlag, New York, 2003.

[34] E.O. Budrene and H.C. Berg. Complex patterns formed by motile cells of *Escherichia coli*. *Nature*, 349:630–633, 1991.

[35] E.O. Budrene and H.C. Berg. Dynamics of formation of symmetrical patterns by chemotactic bacteria. *Nature*, 376:49–53, 1995.

[36] D E Woodward, R Tyson, M R Myerscough, J D Murray, E O Budrene, and H C Berg. Spatio-temporal patterns generated by *Salmonella typhimurium*. *Biophys. J.*, 68:2181–2189, 1995.

[37] M.P. Brenner, L.S. Levitov, and E.O. Budrene. Physical mechanisms for chemotactic pattern formation by bacteria. *Biophys. J.*, 74:1677–1693, 1998.

[38] R. Tyson, S.R. Lubkin, and J.D. Murray. A minimal mechanism for bacterial pattern formation. *Proc. Roy. Soc. Lon. B*, 266:299–304, 1999.

[39] K. Kawasaki, A. Mochizuki, M. Matsushita, T. Umeda, and N. Shigesada. Modeling spatio-temporal patterns generated by *Bacillus subtilis*. *J. Theor. Biol.*, 188:177–185, 1997.

[40] S. E. Espiov and J. A. Shapiro. Kinetic model of proteus mirabilis swarm colony development. *Journal of Mathematical Biology*, 36:249–268, 1998.

[41] O.A. Igoshin, A. Mogilner, R.D. Welch, D. Kaiser, and G. Oster. Pattern formation and travelling in myxobacteria: Theory and modeling. *Proceedings of the National Academy of Sciences*, 98:14913–14918, 2001.

[42] O. J. O'Loan, M. R. Evans, and M. E. Cates. Jamming transition in a homogeneous one-dimensional system: The bus route model. *Physical Review E: Statistical, Nonlinear, and Soft Matter Physics*, 58(2):1404–1418, 1998.

[43] Z Burda, D Johnston, J Jurkiewicz, M Kamiński, MA Nowak, G Papp, and I Zahed. Wealth condensation in pareto macroeconomies. *Phys. Rev. E*, 65:026102, 2002.

[44] K E P Sugden and M R Evans. A dynamically extending exclusion process. *Journal of Statistical Mechanics: Theory and Experiment*, 2007(11):P11013, 2007.

[45] S. Klumpp and R. Lipowsky. Traffic of molecular motors through tube-like compartments. *Journal of Statistical Physics*, 113:233–268, 2003.

[46] R. Lipowsky, S. Klumpp, and T. M. Nieuwenhuizen. Random walks of cytoskeletal motors in open and closed compartments. *Phys. Rev. Lett.*, 87:108101, 2001.

[47] M. Doi. Second quantization representation for classical many-particle system. *Journal of Physics A: Mathematical and General*, 9(9):1465–1477, 1976.

[48] L. Peliti. Path integral approach to birth-death processes on a lattice. *J. Phys. France*, 46(9):1469–1483, 1985.

[49] F. van Wijland. Field theory for reaction-diffusion processes with hard-core particles. *Physical Review E: Statistical, Nonlinear, and Soft Matter Physics*, 63(2):022101, 2001.

[50] J. Tailleur, J. Kurchan, and V. Lecomte. Mapping out-of-equilibrium into equilibrium in one-dimensional transport models. *Journal of Physics A: Mathematical and Theoretical*, 41(50):505001 (41pp), 2008.

[51] L. Bertini, A. De Sole, D. Gabrielli, G. Jona-Lasinio, and C. Landim. Fluctuations in stationary nonequilibrium states of irreversible processes. *Physical Review Letters*, 87(4):040601, 2001.

[52] S. Pilgram, A. N. Jordan, E. V. Sukhorukov, and M. Büttiker. Stochastic path integral formulation of full counting statistics. *Physical Review Letters*, 90(20):206801, 2003.

[53] A. N. Jordan, E.V. Sukhorukov, and S. Pilgram. Fluctuation statistics in networks: A stochastic path integral approach. *Journal of Mathematical Physics*, 45:4386–4418, 2004.

[54] H. Janssen. On a lagrangean for classical field dynamics and renormalization group calculations of dynamical critical properties. *Zeitschrift für Physik B Condensed Matter*, 23(4):377–380, 1976.

[55] C. De Dominicis. Techniques de renormalisation de la théorie des champs et dynamique des phénomènes critiques. *J. Phys. Colloques*, 37:C1–247–C1–253, 1976.

[56] A. Lefevre and G. Biroli. Dynamics of interacting particle systems: stochastic process and field theory. *Journal of Statistical Mechanics: Theory and Experiment*, 2007(07):P07024, 2007.

[57] L. Bertini, A. De Sole, D. Gabrielli, G. Jona-Lasinio, and C. Landim. Macroscopic fluctuation theory for stationary non-equilibrium states. *Journal of Statistical Physics*, 107(3-4):635–675, 2004.

[58] S. Prolhac and K. Mallick. Cumulants of the current in a weakly asymmetric exclusion process. *Journal of Physics A: Mathematical and Theoretical*, 42(17):175001, 2009.

[59] M. R. Evans. Phase transitions in one-dimensional nonequilibrium systems. *Brazilian Journal of Physics*, 30(1):42–57, 2000.

[60] F. Spitzer. Interacting Markov processes. *Adv. in Math.*, 5:246, 1970.

[61] P. Bialas and Z. Burda. Condensation in the backgammon model. *Nucl. Phys. B*, 493:505, 1997.

[62] J. Eggers. Sand as Maxwell's demon. *Physical Review Letters*, 83(25):5322–5325, 1999.

[63] D. van der Meer, K. van der Weele, and D. Lohse. Coarsening dynamics in a vibrofluidized compartmentalized granular gas. *Journal of Statistical Mechanics: Theory and Experiment*, 2004(04):P04004, 2004.

[64] C. Godréche. Dynamics of condensation in zero-range processes. *Journal of Physics A: Mathematical and General*, 36(23):6313–6328, 2003.

[65] S. Grokinsky, G. M. Schütz, and H. Spohn. Condensation in the zero range process: Stationary and dynamical properties. *Journal of Statistical Physics*, 113(3-4):389–410, 2004.

[66] S.N. Majumdar, M.R. Evans, and R.K.P. Zia. Nature of the condensate in mass transport models. *Physical Review Letters*, 94:180601, 2005.

[67] C. Godréche and J. M. Luck. Dynamics of the condensate in zero-range processes. *Journal of Physics A: Mathematical and General*, 38(33):7215–7237, 2005.

[68] Y. Schwarzkopf, M. R. Evans, and D. Mukamel. Zero-range processes with multiple condensates: statics and dynamics. *Journal of Physics A: Mathematical and Theoretical*, 41(20):205001 (21pp), 2008.

[69] S.A. Safran. *Statistical Thermodynamics of Surfaces, Interfaces and Membranes*. Addison Wesley, New York, 1994.

[70] R.E. Goldstein. Model for the phase equilibrium of micellar solutions of nonionic surfactants. *J. Chem. Phys.*, 84:3367, 1986.

[71] M.R. Evans, S.N. Majumdar, and R.K.P. Zia. Canonical analysis of condensation in factorised steady states. *Journal of Statistical Physics*, 123:357, 2006.

[72] R. T. Rockafellar. *Convex Analysis*. Princeton University Press, 1970.

[73] P.M. Chaikin and T.C. Lubensky. *Principles of Condensed Matter Physics*. Cambridge University Press, 1995.

[74] P. Hänggi, P. Talkner, and M. Borkovec. Reaction-rate theory: fifty years after Kramers. *Rev. Mod. Phys.*, 62(2):251–341, 1990.

[75] C. Godréche. From urn models to zero-range processes: Statics and dynamics. In M. Henkel and R. Sanctuary, editors, *Ageing and the Glass Transition*, volume 716/2007 of *Lecture Notes in Physics*, chapter 6. Springer Berlin / Heidelberg, 2007.

[76] S.J. Cornell, K. Kaski, and R.B. Stinchcombe. Domain scaling and glassy dynamics in a one-dimensional Kawasaki Ising model. *Physical Review B*, 44:12263, 1991.

[77] M. R. Evans and T. Hanney. Phase transition in two species zero-range process. *Journal of Physics A: Mathematical and General*, 36(28):L441–L447, 2003.

[78] J. Garca-Ojalo and J.M. Sancho. *Noise in Spatially Extended Systems*. Springer, 1999.

[79] P. Sollich. Predicting phase equilibria in polydisperse systems. *Journal of Physics: Condensed Matter*, 14(3):R79, 2002.

[80] G. Schütz and S. Sandow. Non-abelian symmetries of stochastic processes: Derivation of correlation functions for random-vertex models and disordered-interacting-particle systems. *Phys. Rev. E*, 49(4):2726–2741, 1994.

[81] P. L. Krapivsky, S. Redner, and J. Tailleur. Dynamics of an unbounded interface between ordered phases. *Phys. Rev. E*, 69(2):026125, 2004.

[82] T. Funaki and H. Spohn. Motion by mean curvature from the Ginzburg-Landau interface model. *Communications in Mathematical Physics*, 185:1–36, 1997.

[83] P. C. Hohenberg and B. I. Halperin. Theory of dynamic critical phenomena. *Rev. Mod. Phys.*, 49:435–479, Jul 1977.

[84] A. J. Bray. Theory of phase-ordering kinetics. *Advances in Physics*, 43:357–459, 1994.

[85] J. A. Shapiro. The significances of bacterial colony patterns. *BioEssays*, 17(7):597–607, 1995.

[86] E. Ben-Jacob, I. Cohen, and H. Levine. Cooperative self-organization of microorganisms. *Advances in Physics*, 49(4):395–554, 2000.

[87] R. M. Harshey. Bacterial motility on a surface: Many ways to a common goal. *Annual Review of Microbiology*, 57(1):249–273, 2003.

[88] J.P. Hansen and I.R. McDonald. *Theory of Simple Liquids*. Academic Press, 2006.

[89] L.G. Wilson, V.A. Martinez, J. Schwarz-Linek, J. Tailleur, P.N. Pusey, G. Bryant, and W.C.K. Poon. Differential dynamic microscopy of bacterial motility. *Phys. Rev. Lett.*, 106:018101, 2011.

[90] O.A. Croze, G.P. Ferguson, M.E. Cates, and W.C.K. Poon. Migration of chemotactic bacteria in soft agar: Role of gel concentration. *Biophysical Journal*, 101(3):525 – 534, 2011.

[91] M. Ericsson, D. Hanstorp, P. Hagberg, J. Enger, and T. Nystrm. Sorting out bacterial viability with optical tweezers. *Journal of Bacteriology*, 182(19):5551–5555, 2000.

[92] T. Nyström. Not quite dead enough: on bacterial life, culturability, senescence, and death. *Archives of Microbiology*, 176(3):159–164, 2001.

[93] C Liu, X. Fu, L. Liu, X. Ren, C. K.L. Chau, S. Li, L. Xiang, H. Zeng, G. Chen, L.-H. Tang, P. Lenz, X. Cui, W. Huang, T. Hwa, and J.-D. Huang. Sequential establishment of stripe patterns in an expanding cell population. *Science*, 334(6053):238–241, 2011.

[94] R. Erban and H. G. Othmer. From signal transduction to spatial pattern formation in *E. coli*: A paradigm for multiscale modeling in biology. *Multiscale Modeling & Simulation*, 3(2):362–394, 2005.

[95] P. Chavanis and C. Sire. Kinetic and hydrodynamic models of chemotactic aggregation. *Physica A: Statistical Mechanics and its Applications*, 384(2):199 – 222, 2007.

[96] E. Frey. Evolutionary game theory: Theoretical concepts and applications to microbial communities. *Physica A: Statistical Mechanics and its Applications*, 389(20):4265 – 4298, 2010.

[97] W. R. Young, A. J. Roberts, and G. Stuhne. Reproductive pair correlations and the clustering of organisms. *Nature*, 412:328–331, 2001.

[98] G. Hauser. *Über Fäulnissbacterien und deren Beziehungen zur Septicämie*. Vogel, Leipzig, 1885.

[99] O Rauprich, M Matsushita, CJ Weijer, F Siegert, SE Esipov, and JA Shapiro. Periodic phenomena in *Proteus mirabilis* swarm colony development. *J. Bacteriol.*, 178(22):6525–6538, 1996.

[100] C. Allison and C. Hughes. Bacterial swarming: an example of prokaryotic differentiation and multicellular behaviour. *Sci. Prog.*, 75(298):403–422, 1991.

[101] A. Czirók, M. Matsushita, and T. Vicsek. Theory of periodic swarming of bacteria: Application to *Proteus mirabilis*. *Phys. Rev. E*, 63(3):031915, 2001.

[102] O. Hallatschek and K. S. Korolev. Fisher waves in the strong noise limit. *Phys. Rev. Lett.*, 103:108103, 2009.

[103] M. Assaf, A. Kamenev, and B. Meerson. Population extinction risk in the aftermath of a catastrophic event. *Physical Review E: Statistical, Nonlinear, and Soft Matter Physics*, 79(1):011127, 2009.

Publications

A.G. Thompson, J. Tailleur, M.E. Cates and R.A. Blythe. Lattice Models of Nonequilibrium Bacterial Dynamics In *J. Stat. Mech.*, P02029, 2011.

A.G. Thompson, J. Tailleur, M.E. Cates and R.A. Blythe. Zero-range processes with saturated condensation:the steady state and dynamics. In *J. Stat. Mech.*, P02013, 2010.